



**UNIVERSIDAD NACIONAL AUTÓNOMA DE MÉXICO**  
**PROGRAMA DE POSGRADO EN CIENCIAS FÍSICAS**  
**INSTITUTO DE FÍSICA**  
**FÍSICA DE ALTAS ENERGÍAS, FÍSICA NUCLEAR, GRAVITACIÓN Y**  
**FÍSICA MATEMÁTICA**

# **Searching for dark matter interactions in the PICO-60 bubble chamber and background simulations for the PICO500 detector**

**TESIS**  
**QUE PARA OPTAR POR EL GRADO DE:**  
**DOCTOR EN CIENCIAS (FÍSICA)**

**PRESENTA:**  
**ALEJANDRO SANTIAGO GARCÍA VILTRES**

**TUTOR:** Dr. Eric VÁZQUEZ JÁUREGUI  
Instituto de Física - UNAM

Ciudad Universitaria, CD. MX, Noviembre 2023

©Alejandro Santiago García Viltres 2023



Universidad Nacional  
Autónoma de México



**UNAM – Dirección General de Bibliotecas**  
**Tesis Digitales**  
**Restricciones de uso**

**DERECHOS RESERVADOS ©**  
**PROHIBIDA SU REPRODUCCIÓN TOTAL O PARCIAL**

Todo el material contenido en esta tesis esta protegido por la Ley Federal del Derecho de Autor (LFDA) de los Estados Unidos Mexicanos (México).

El uso de imágenes, fragmentos de videos, y demás material que sea objeto de protección de los derechos de autor, será exclusivamente para fines educativos e informativos y deberá citar la fuente donde la obtuvo mencionando el autor o autores. Cualquier uso distinto como el lucro, reproducción, edición o modificación, será perseguido y sancionado por el respectivo titular de los Derechos de Autor.



# Searching for dark matter interactions in the PICO-60 bubble chamber and background simulations for the PICO500 detector

by

Alejandro Santiago García Viltres

a dissertation submitted in partial fulfillment  
of the requirements for the degree of

DOCTOR OF PHILOSOPHY (PH.D.)

at

NATIONAL AUTONOMOUS UNIVERSITY OF MEXICO (UNAM)

Graduate Program  
PHYSICAL SCIENCES

Supervisor: Prof. Dr. Eric VÁZQUEZ JÁUREGUI  
Institute of Physics - UNAM

CDMX, Mexico  
November 2023

©Alejandro Santiago García Viltres 2023



**PROTESTA UNIVERSITARIA DE INTEGRIDAD Y  
HONESTIDAD ACADÉMICA Y PROFESIONAL  
(Graduación con trabajo escrito)**

De conformidad con lo dispuesto en los artículos 87, fracción V, del Estatuto General, 68, primer párrafo, del Reglamento General de Estudios Universitarios y 26, fracción I, y 35 del Reglamento General de Exámenes, me comprometo en todo tiempo a honrar a la Institución y a cumplir con los principios establecidos en el Código de Ética de la Universidad Nacional Autónoma de México, especialmente con los de integridad y honestidad académica.

De acuerdo con lo anterior, manifiesto que el trabajo escrito titulado:

Searching for dark matter interactions in the PICO-60 bubble chamber and background  
simulations for the PICO500 detector

que presenté para obtener el grado de ----Doctorado---- es original, de mi autoría y lo realicé con el rigor metodológico exigido por mi programa de posgrado, citando las fuentes de ideas, textos, imágenes, gráficos u otro tipo de obras empleadas para su desarrollo.

En consecuencia, acepto que la falta de cumplimiento de las disposiciones reglamentarias y normativas de la Universidad, en particular las ya referidas en el Código de Ética, llevará a la nulidad de los actos de carácter académico administrativo del proceso de graduación.

Una firma manuscrita en tinta azul que parece decir "Alejandro".

**Atentamente**

Alejandro Santiago García Viltres, 518493181

**(Nombre, firma y Número de cuenta de la persona alumna)**

**Contact details:** Alejandro Santiago GARCÍA VILTRES  
Instituto de Física (IFUNAM)  
Universidad Nacional Autónoma de México  
Circuito de la Investigación Científica, Ciudad Universitaria  
CDMX, México CP 04510  
agarciaviltres@gmail.com

Prof. Dr. Eric VÁZQUEZ JÁUREGUI  
Instituto de Física (IFUNAM)  
Universidad Nacional Autónoma de México  
Circuito de la Investigación Científica, Ciudad Universitaria  
CDMX, México CP 04510  
ericvj@fisica.unam.mx

## Declaration of Authorship

I hereby declare that this doctoral thesis was independently composed and authored by myself.

All content and ideas drawn directly or indirectly from external sources are indicated as such. All sources and materials that have been used are referred to in this thesis.

The thesis has not been submitted to any other examining body and has not been published.

---

Place, date

---

Signed: Alejandro Santiago GARCÍA VILTRES

# Abstract

The PICO collaboration since 2015 uses bubble chamber detectors for direct dark matter searches. Due to the elusiveness of dark matter, ever larger detectors are being built. The collaboration is currently working on the design and assembly of the PICO500 detector, the next generation of the PICO-40L detector currently collecting data. This detector will have a volume of 260 liters and a height of almost 4 meters and will be located like its predecessor models at SNOLAB to guarantee a shielding of 2 km of rock. The PICO-60 bubble chamber was the last experiment of the collaboration that collected data between 2013 and 2017 in its two stages to search for dark matter in the form of Weakly Interacting Massive Particle (WIMP). This detector was initially filled with  $\text{CF}_3\text{I}$  in 2013 claiming competitive spin-dependent and spin-independent limits in low-mass parameter space for dark matter reaching an exposure of 3415 kg-day and operating at thermodynamic thresholds between 7 and 20 keV. In 2016 it resumed taking data that had been interrupted in 2014, and was filled with 52 kg of  $\text{C}_3\text{F}_8$  to improve the sensitivity to spin-dependent dark matter interaction operating at thermodynamic thresholds of 2.45 and 3.29 keV and reaching exposures of 1404 kg-day and 1167 kg-day respectively. Many models predict that the dark matter can be coupled to the electromagnetic current through superior multipolar interactions. Using the PICO-60 data we have analyzed and imposed limits for the coupling of photon-mediated interactions using non-relativistic contact operators in an effective field theory framework. On the other hand, PICO bubble chambers have excellent sensitivity to inelastic dark matter-nucleus interactions due to the use of heavy targets such as iodine and the wide range of recoil energies they can record. The study of the inelastic dispersion of the dark matter nucleus is a very interesting way to elucidate the properties of such matter within the wide spectrum of existing theoretical scenarios. In this thesis we report the results obtained for this type of dispersion using the PICO-60 bubble chambers. Our analysis was done in a wide region of the parameter space, allowing us to disprove the assertions of various scenarios that provide a feasible explanation of the signal observed by DAMA assuming an inelastic interaction.

# Resumen

La colaboración PICO desde el 2015 utiliza detectores de cámara de burbujas para búsquedas directas de materia oscura. Debido al carácter elusivo de la materia oscura, se están construyendo detectores cada vez más grandes. La colaboración está trabajando actualmente en el diseño y montaje del detector PICO500, la próxima generación del detector PICO-40L que actualmente recopila datos. Este detector tendrá un volumen de 260 litros y una altura de casi 4 metros y se ubicará como sus modelos predecesores en SNOLAB para garantizar un blindaje de 2 km de roca. La cámara de burbujas PICO-60 fue el último experimento de la colaboración que recopiló datos entre 2013 y 2017 en sus dos etapas para buscar materia oscura en forma de Partículas Masivas de Interacción Débil (WIMP de sus siglas en inglés). Este detector se llenó inicialmente con CF3I en 2013, afirmando límites competitivos dependientes e independientes del espín en el espacio de parámetros de baja masa para la materia oscura, alcanzando una exposición de 3415 kg-día y operando en umbrales termodinámicos entre 7 y 20 keV. En 2016 reanudó la toma de datos que se había interrumpido en 2014 y se llenó con 52 kg de C3F8 para mejorar la sensibilidad a la interacción de la materia oscura dependiente del espín operando con umbrales termodinámicos de 2,45 y 3,29 keV y alcanzando exposiciones de 1404 kg-día y 1167 kg-día respectivamente. Muchos modelos predicen que la materia oscura puede acoplarse a la corriente electromagnética mediante interacciones multipolares superiores. Utilizando los datos de PICO-60, hemos analizado e impuesto límites para el acoplamiento de interacciones mediadas por fotones utilizando operadores de contacto no relativistas en un marco de teoría de campo efectiva. Por otro lado, las cámaras de burbujas PICO tienen una excelente sensibilidad a las interacciones inelásticas entre la materia oscura y el núcleo debido al uso de objetivos pesados como el yodo y la amplia gama de energías de retroceso que pueden registrar. El estudio de la dispersión inelástica del núcleo de materia oscura es una forma muy interesante de dilucidar las propiedades de dicha materia dentro del amplio espectro de escenarios teóricos existentes. En esta tesis reportamos los resultados obtenidos para este tipo de dispersión utilizando las cámaras de burbujas PICO-60. Nuestro análisis se realizó en una amplia región del espacio de parámetros, lo que nos permitió refutar las afirmaciones de varios escenarios que brindan una explicación factible de la señal observada por DAMA asumiendo una interacción inelástica.



# Acknowledgements

Este trabajo fue realizado gracias al apoyo del Consejo Nacional de Ciencia y Tecnología (CONACyT) proyecto CONACyT CB-2017-2018/A1-S-8960 y al Programa UNAM-PAPIIT IN108020 y IN105923

# Contents

<b>Declaration of Authorship</b>	<b>i</b>
<b>Abstract</b>	<b>ii</b>
<b>Acknowledgements</b>	<b>iv</b>
<b>List of Figures</b>	<b>ix</b>
<b>List of Tables</b>	<b>xi</b>
<b>1 Introduction</b>	<b>1</b>
<b>2 Background simulations for the PICO500 detector</b>	<b>3</b>
2.1 Introduction . . . . .	3
2.2 Sources of neutrons . . . . .	3
2.2.1 SOURCES4C code . . . . .	3
2.2.2 GEANT4 code . . . . .	4
2.2.3 Component material neutron yields . . . . .	4
2.2.4 Other neutron sources . . . . .	5
$(\gamma, n)$ neutrons . . . . .	5
$\mu$ -induced neutrons . . . . .	5
2.3 Monte-Carlo (MC) Simulations . . . . .	6
2.3.1 New Design for PICO-500 . . . . .	7
Updated top and bottom flanges . . . . .	8
2.3.2 Neutron Propagation in PICO-500 . . . . .	9
2.3.3 Inner assembly . . . . .	10
PV Neutron Simulations . . . . .	10
Top and Bottom Flanges . . . . .	12
Retroreflector Neutron Simulations . . . . .	12
Outer and Inner Copper Plates . . . . .	12
OV and IV neutron simulations . . . . .	13
C <sub>3</sub> F <sub>8</sub> neutrons . . . . .	13
Mineral Oil . . . . .	14
2.3.4 Optical system . . . . .	14
2.3.5 Acoustic system . . . . .	14
Updating of piezos . . . . .	15
2.4 PICO500 neutron budget and detector material radio purity requirements . . . . .	17
2.5 Radon exposure . . . . .	17
2.5.1 Radon Diffusion . . . . .	18
2.5.2 Radon daughter deposition . . . . .	19
2.6 Radon Emanation . . . . .	19
2.6.1 Cooling System . . . . .	20

2.7	Other miscellaneous neutron backgrounds	20
2.7.1	Dust deposition	20
2.7.2	$(\gamma, n)$ neutrons	21
2.8	Total Results	22
<b>3</b>	<b>Searching for dark matter interactions in the PICO-60 bubble chamber</b>	<b>23</b>
3.1	Results on photon-mediated dark matter-nucleus interactions from the PICO-60 $C_3F_8$ bubble chamber	23
3.1.1	NREFT	23
3.1.2	From Matlab to Python	24
3.1.3	MCMC routine	26
3.1.4	Comparing previous results for SD and SI couplings	27
	Ultra violet (UV) and NREFT for SD interaction	29
3.1.5	WIMpy_NREFT code to study specific couplings and NREFT operators	30
	NREFT-derived specific interactions	30
3.1.6	DM with an anapole moment	31
	DM with a magnetic dipole moment	32
	DM with millicharge	32
	DM with electric dipole moment	33
	Results for specific interactions	33
3.2	Results on Inelastic dark matter-nucleus interactions from the PICO-60 $C_3F_8$ and $CF_3I$ bubble chambers	36
3.2.1	Introduction	36
	Non-relativistic effective field theory	38
	Kinematics of inelastic dark matter scattering	39
	Detector efficiencies	41
3.2.2	Results for SI and SD couplings	41
3.2.3	Excitation limits on large target mass	46
3.2.4	Results for NREFT operators	48
<b>4</b>	<b>Conclusion</b>	<b>50</b>
<b>A</b>	<b>Codes used in the thesis</b>	<b>51</b>
A.1	Rate calculators	51
A.2	Other relevant codes	54
	<b>Bibliography</b>	<b>59</b>

# List of Figures

2.1	Conceptual design for the PICO-500 detector, showing the pressure vessel, camera windows, top/bottom flanges, and the quartz jar configuration. . . . .	7
2.2	Behavior of the background rates from decreasing the radius of the pressure vessel. The PV rate is shown in red, the retro-reflector rate (thin layer mounted to inside of PV) is shown in blue, and the rate from the cameras is shown in black. . . . .	10
2.3	New model of the PICO-500 pressure vessel. . . . .	11
2.4	Current PICO-500 detector model implemented in Geant4 code. Added volume changes: Two retro-reflector cones inside PV, vacuum region outside lower PV, three stainless steel source tubes filled with air, and four high pressure accumulators filled with mineral oil. . . . .	11
2.5	Retro-reflector cone assembly included in the Geant4 model of PICO-500. . . . .	12
2.6	Configuration of one of the cameras where you can see first the steel enclosure of the camera, the lens, the Printed Circuit Board (PCB) and the LED lights. . . . .	15
2.7	Piezo model in GEANT4, the Piezo Housing, the Printed Circuit Board (PCB) and the piezoelectric material (PbZr) were considered. . . . .	16
2.8	Left: Piezo model showing the piezo housing, PCB, and piezoelectric material. Center: Front view of the two layers of piezos distributed around the IV. Right: Top view of the array of 24 piezos distributed in two layers at different heights measured from the top of the IV. . . . .	16
2.9	Upper left: Surfaces used to emit gamma particles. Upper right: Gamma flux of 3 to 100 MeV from the cavern. Bottom left: Kinetic energy spectrum of gamma particles registered in the volume of water shielding. Bottom right: Cross sections for the formation of neutrons in the isotopes present in water. . . . .	22
3.1	Exclusion limits for SD coupling using PICO-60 data (left). Statistical test for 90% upper limit (center). WIMP sensitivities (right). . . . .	25
3.2	Parameter 3; Fluorine setpoint at 20% efficiency . . . . .	27
3.3	Probability distribution obtained for WIMP efficiency at 2.4 keV threshold, 19 GeV mass and SD coupling. . . . .	28
3.4	Likelihood surfaces obtained for SD coupling and a mass of 19 GeV. . . . .	28
3.5	Exclusion limits of both energy thresholds for SD coupling of Jin's and our results(upper left). SI coupling results for both thresholds of Jin's and our results(upper right). SD coupling exclusion limits for the simple merge of best fits of both results(lower left). SI coupling limits for the simple merge of best fits of both results(lower right). . . . .	29
3.6	Expected event rate for SD coupling considering dmdd and WIMpy codes for UV and NREFT theories (left). . . . .	30

3.7	Comparison for different operators using the NREFT in WIMpy (blue) and dmdd (red) for a WIMP mass of 10 GeV. . . . .	31
3.8	Contour plot of integrated efficiency $\phi$ at 2.45 and 3.29 keV. Contour layers have been color coded to represent the difference in $\chi^2$ with respect to the minimum. Details in the outer boundary of the plot are subject to statistical fluctuations. . . . .	34
3.9	Limits on the coupling strength for specific interactions using the SHM. . . . .	35
3.10	Scattering rates in $C_3F_8$ (red), xenon (dashed blue), and argon (dotted green) for a DM particle with mass of 5 GeV/ $c^2$ with coupling through the anapole moment (upper left, for a coupling of $3.6 \times 10^{-8}$ GeV $^{-2}$ ), millicharge (upper right, for a coupling of $2.2 \times 10^{-8} e$ ), magnetic dipole moment (lower left, for a coupling of $2.8 \times 10^{-8}$ GeV $^{-1}$ ), and electric dipole moment (lower right, for a coupling of $2.8 \times 10^{-8}$ GeV $^{-1}$ ). The rates were obtained with the WIMpy_NREFT package [46]. . . . .	36
3.11	Exclusion limits at 90% C.L. for the anapole moment (upper left), millicharge (upper right), magnetic dipole moment (lower left), and electric dipole moment (lower right) couplings. The limits are derived from the profile likelihood analysis of the PICO-60 $C_3F_8$ (red) combined blind exposure. Limits from XENON-1T (dashed blue) [21] and DEAP-3600 (dotted green) [2] using xenon and argon, respectively, are also shown. . . . .	37
3.12	Nucleation efficiency curves for the detectors considered in this work. Efficiency curves for detectors with Xenon targets XENON-1T (upper left) [15] and PANDAX-4T (upper right) [52]. On the bottom we have the efficiency curves for the PICO-60 detector with $CF_3I$ (left) and $C_3F_8$ (right) targets. . . . .	42
3.13	Exclusion limits as a function of the delta parameter for a WIMP mass of 1TeV on the PICO-60 bubble chamber and the XENON-1T and PANDAX-4T TPCs. Left: 90% limits for SI coupling ( $\mathcal{O}_1$ ), in the case of PICO-60 we show the results for both targets ( $C_3F_8$ and $CF_3I$ ) separately and combined. Right: Limits at 90% confidence level for SD interaction ( $\mathcal{O}_4$ ), in the case of PICO-60 we only consider coupling with protons and for the Xenon detectors we explore both possibilities. . . . .	43
3.14	Upper limits (90% C. L.) on inelastic DM-nucleon scattering cross sections assuming isospin conservation as a function of the mass splitting for the effective operator $\mathcal{O}_1$ and DM masses of 10 GeV/ $c^2$ , 100 GeV/ $c^2$ , 1 TeV/ $c^2$ , and 10 TeV/ $c^2$ , from the analysis of the PICO-60 $CF_3I$ and $C_3F_8$ experiments. Limits from XENON- 1T [15], PANDAX-4T [53], and CRESST II [47] are also shown. The limits from XENON-1T and PANDAX-4T were derived using the same methodology, utilizing the available information and data published by the respective collaborations. . . . .	44
3.15	DAMA allowed regions obtained from [57, 61] and upper bounds of PICO-60 $CF_3I$ and $C_3F_8$ in DM-nucleon scattering cross sections as a function of mass splitting for the effective operator $\mathcal{O}_1$ and DM masses of 5.5 GeV/ $c^2$ , 11 GeV/ $c^2$ , 100 GeV/ $c^2$ and 300 GeV/ $c^2$ at 99% C. L. . . . .	45

3.16	Upper limits (90% C. L.) on inelastic DM-nucleon scattering cross sections assuming isospin conservation as a function of the mass splitting for the effective operator $\mathcal{O}_4$ and DM masses of $10 \text{ GeV}/c^2$ , $100 \text{ GeV}/c^2$ , $1 \text{ TeV}/c^2$ and $10 \text{ TeV}/c^2$ , from the analysis of the PICO-60 $\text{CF}_3\text{I}$ and $\text{C}_3\text{F}_8$ experiments. Limits from XENON-1T and PANDAX-4T are also shown. The limits from XENON-1T and PANDAX-4T were derived using the same methodology, utilizing the available information and data published by the respective collaborations. . . . .	46
3.17	Upper limits at 90% C.L. obtained from the PICO-60 $\text{C}_3\text{F}_8$ and $\text{CF}_3\text{I}$ experiments on inelastic scattering cross sections of DM-protons and DM-nucleons assuming isospin conservation. The limits are presented as a color scale for the effective operators $\mathcal{O}_1$ (top) and $\mathcal{O}_4$ (bottom) as a function of mass division and mass DM. . . . .	47
3.18	Exclusion limits with a 90% confidence level considering excitations in the isotopes of $^{127}\text{I}$ , $^{129}\text{Xe}$ and $^{131}\text{Xe}$ present in the PICO-60, XENON-1T and PANDAX-4T detectors for specific mass splittings of 57.6, 39.6 and 80.2 keV. On the left side we consider couplings with protons and on the right side with neutrons. . . . .	47
3.19	Exclusion curves behavior at 90% confidence level as a function of the delta parameter for SI operators. . . . .	48
3.20	Exclusion curves at 90% confidence level as a function of the delta parameter for the group of operators behaving as spin-dependent. . .	49

# List of Tables

2.1	Neutron Yield determined from the SOURCES4c code for the different detector components (taking into account $(\alpha, n)$ reactions, spontaneous fission, and delayed neutron emission). The units for the neutron yield are neutrons per gram per parts per billion (ppb) per seconds.	5
2.2	Gamma flux measured in SNOLAB. Alan work: region from 2 to 8 MeV. Our study: region from 8 to 100 MeV.	6
2.3	The $\mu$ -induced neutron flux from the rock into SNOLAB cavity.	6
2.4	Properties of the PICO-500 detector components	8
2.5	Activity values with their respective errors for different detector materials in ppb units taken from SNOLAB page [33].	8
2.6	Neutron fluence in each PICO-500 detector component in 1 year, including neutrons from $(\alpha, n)$ reactions as well as fission and direct neutron decay.	9
2.7	Probability that neutrons produce a WIMP-like event at $C_3F_8$ .	13
2.8	Results for the number of events of a single bubble in the different components of the PICO500 detector.	15
2.9	Results for the number of single bubble events per year assuming 12 piezos and connectors in each layer.	16
2.10	Probability of a neutron interacting with the fiducial volume of $C_3F_8$ , for different detector components.	17
2.11	Maximum alpha rates from $^{210}Po$ for different components of the detector in column four, in column two we can see the values of the neutron yield and the probability of producing a background event by neutrons generated in each of the components is shown in column three.	18
2.12	Limits on radon emanation for main detector components.	19
2.13	Maximum $^{222}Rn$ concentration allowed for the refrigerant liquid in the Copper Tubing Inner and the Cooling Coil.	20
2.14	Number of background events due to contamination by dust present in the components exposed to the cave.	21
2.15	Total contribution to the number of single events like WIMP per year for the simulated principal components of the PICO500 detector.	22
3.1	The best-fit parameters explored by our algorithm. The first row lists the starting nucleation threshold while the next 4 rows are increments from the previous step.	26
3.2	NREFT operators, with $\vec{v}^\perp$ the component of the velocity perpendicular to the momentum transfer, $i\frac{\vec{q}}{m_N}$ the momentum transfer, $\vec{S}_\chi$ -DM spin and $\vec{S}_N$ -nucleon spin.	31
3.3	NREFT operators, with $\vec{v}^\perp$ the component of the velocity perpendicular to the momentum transfer, $i\frac{\vec{q}}{m_N}$ the momentum transfer, $\vec{S}_\chi$ -DM spin and $\vec{S}_N$ -nucleon spin.	41

3.4	Number of observed events and background level reported by both experiments in the results for SI coupling [15, 52]. . . . .	43
-----	--	----



## Chapter 1

# Introduction

There is overwhelming evidence that most of the matter in the Universe is not baryonic. There are various astrophysical observations that demonstrate the presence of a certain component of dark matter (DM), among the main ones we can find the high speed of rotation of gas and stars on the outside of spiral galaxies, high-speed dispersion, and the extended halo X-ray imaging of hot gas in elliptical galaxies, and high-speed, high-temperature scattering of gas in galaxy clusters. The search for Weakly Interacting Massive Particles (WIMPs) is a challenge due to the predicted small WIMP-nucleon scattering cross sections, which require nuclear recoil energies on the order of 1-100 keV. To reach sufficient sensitivity at this low threshold, experiments require a large detector volume located in a background-suppressed environment, like SNOLAB. Since the nature of the WIMP-nucleon interaction is unknown, explorations into both spin-dependent (SD) and spin-independent (SI) couplings are necessary. Furthermore, in this sense, the inelastic dark matter-nucleus dispersion and the coupling of the DM with the electromagnetic current through higher multipole interactions are also studied.

The PICO collaboration has operated several bubble chambers using fluorocarbon fluids as the target material and taking advantage of the natural shielding of the underground facilities at SNOLAB [62]. These detectors are made with a stainless steel (SS) pressure vessel filled with hydraulic fluid, inside which it has an inner system composed of a high-purity synthetic fused silica jar and stainless steel bellows. Inside it is filled with a fluorocarbon material (CF<sub>3</sub>I or C<sub>3</sub>F<sub>8</sub>). The pressure vessel is located inside a tank with water that provides protection against external background radiation and controls the temperature. Camera arrays are used to photograph the chambers to identify the bubbles, and also for position reconstruction and as a trigger. As an additional mechanism to record information about the bubble formation process, low-radioactivity piezoelectric transducers are placed in the silica container to record the acoustic signal of the process. This acoustic signal after processing is used to reject alpha decay backgrounds. Nuclear and electronic recoils are calibrated using neutron (AmBe and Cf-252) and gamma (Co-60 and Ba-133) sources [12]. The bubble chambers developed by the PICO collaboration have excellent sensitivity to nuclear recoil and are overall almost insensitive to electron recoil backgrounds. The PICO-60 CF<sub>3</sub>I bubble chamber had 36.8 kg of CF<sub>3</sub>I and was operated between June 2013 and May 2014 [11], reaching an exposure of 3415 kg-day at different thermodynamic or "Seitz" thresholds [59] between 7 and 20 keV. The main objective of this detector was to search for spin-independent couplings between the nucleon and WIMPs by using iodine as a target and to explore the spin-dependent coupling of the proton with WIMPs through fluorine. In order to explore the spin-dependent sector in more detail, the PICO-60 C<sub>3</sub>F<sub>8</sub> bubble chamber was built, which was filled with 52.2 kg of C<sub>3</sub>F<sub>8</sub> and operated in two stages between November 2016

and June 2017 [10, 8] at Seitz thresholds of 3.29 keV with an exposure of 1167 kg-day in the first stage and at a Seitz threshold of 2.45 keV with an exposure of 1404 kg-day in the second stage. The results from this camera established the most stringent direct detection constraints to date on the spin-dependent WIMP-proton cross section with a value of  $2.5 \times 10^{-41} \text{ cm}^2$  for a WIMP of 25 GeV/c<sup>2</sup> [8].

Using the data reported by both PICO-60 bubble chambers we set ourselves the task of exploring various theoretical models that address the study of interactions between dark matter and the nucleus. Specifically in our work we present the exclusion limits imposed by PICO-60 for inelastic and photon-mediated interactions between dark matter and the nucleus. It is important to point out that the method of calculating the limits and exclusion curves of both detectors differs since the calibration programs were different for both cameras. That is, to extract the sensitivity of the CF<sub>3</sub>I run, a global fit to the YBe and AmBe neutron data [56] and the pion beam data [18] was used. Efficiency curves were obtained by fitting monotonically increasing piecewise linear functions [11]. In the case of the C<sub>3</sub>F<sub>8</sub> runs, different neutron sources were used, specifically monoenergetic neutrons with energies of 24 keV produced by SbBe sources, energies of 50, 61 and 97 keV produced in  $^{51}\text{V}(p,n)^{51}\text{Cr}$  reactions and data of AmBe neutrons [8]. For each calibration experiment the carbon and fluorine efficiency curves were obtained similarly to that described for the CF<sub>3</sub>I run and for both thresholds with C<sub>3</sub>F<sub>8</sub> the efficiencies were extracted with a fit using the python emcee [37] Markov Chain Monte Carlo (MCMC) code [26, 7]. For the calculation of the PICO-60 CF<sub>3</sub>I and C<sub>3</sub>F<sub>8</sub> limits we follow the standard halo parametrization [49] assuming the same astrophysical parameters for both detectors and a local dark matter density  $\rho_D = 0.3 \text{ GeV}/c^2/\text{cm}^3$ . The exclusion limits noted are obtained for each of the target fluids employed, both results consistent with the absence of any dark matter signal. The range of nuclear recoil energies extends from the thermodynamic threshold to 100 keV. This high energy limit was chosen conservatively due to the lack of acoustic calibration for recoils above  $\sim 100$  keV.

## Chapter 2

# Background simulations for the PICO500 detector

## 2.1 Introduction

The PICO-500 experiment will search for dark matter by first operating a 260 L bubble chamber filled with  $C_3F_8$ , a target sensitive to the SI and SD WIMP-nucleon cross-sections around  $10^{-44} \text{ cm}^2$  and  $10^{-42} \text{ cm}^2$ , respectively. There are three main classes of backgrounds that can be confused with an interaction of dark matter particles: neutrons,  $\beta/\gamma$ , and alpha decays. In the case of PICO-500, the primary focus are  $(\alpha, n)$  reactions produced in the internal components of the detector.  $\beta/\gamma$  interactions are suppressed thanks to thermodynamic conditions of the moderately super-heated bubble chamber. Alpha particles don't travel far in the materials, therefore producing backgrounds near the surfaces that can be removed by fiducial cuts, along with acoustic cuts as alpha energy depositions are distinguishable from nuclear recoils.

Alpha particles with MeV scale energies are produced from the decay of radioactive impurities:  $^{238}\text{U}$ ,  $^{235}\text{U}$ ,  $^{232}\text{Th}$ ,  $^{210}\text{Pb}$ , and/or radon emanation into the detector materials. Although Alpha particles themselves can be identified in the detector, they are concerning because they can interact with the detector components to release neutrons. The secondary neutrons will travel farther into the target volume, potentially appearing indistinguishable from a dark matter candidate.

This document lists all potential sources of neutrons in PICO-500, with an emphasis on  $(\alpha, n)$  reactions. Also provided are calculations that approximate the limits of radio-active impurities allowed, in order to achieve scientific goals.

## 2.2 Sources of neutrons

For PICO, it is imperative to have accurate knowledge of all significant sources of backgrounds. Neutron sources found in PICO-500 will include the  $(\alpha, n)$  reactions, fission neutrons, direct neutron decays of the  $^{238}\text{U}$  chain,  $(\gamma, n)$  neutrons, and muon-induced neutrons.

### 2.2.1 SOURCES4C code

SOURCES4C is a library that determines neutron production rates and energy spectra for  $(\alpha, n)$  reactions, spontaneous fission, and delayed neutron emission ( $\beta^-, n$ ) due to radionuclide decay [63]. The code is able to simulate  $(\alpha, n)$  reactions in four types of problems: homogeneous media (i.e., a mixture of  $\alpha$ -emitting source material

and low- $Z$  target material), two-region interface problems (i.e., a slab of  $\alpha$ -emitting source material in contact with a slab of low  $Z$  target material), three-region interface problems (i.e., a thin slab of low- $Z$  target material sandwiched between  $\alpha$ -emitting source material and low- $Z$  target material), and  $(\alpha, n)$  reactions induced by a monoenergetic beam of  $\alpha$ -particles incident on a slab of target material.

The  $(\alpha, n)$  spectra are calculated using an assumed isotropic angular distribution in the center-of-mass system with a library of 107 nuclide decay  $\alpha$ -particles, 24 sets of measured and/or evaluated  $(\alpha, n)$  cross sections, product nuclide level branching fractions, and functional  $\alpha$ -particle stopping cross sections for  $Z < 106$ . Spontaneous fission energy spectra are calculated with evaluated half-life, spontaneous fission branching, and Watt spectrum parameters for 44 actinides. The delayed neutron spectra are taken from an evaluated library of 105 precursors.

### 2.2.2 GEANT4 code

Geant4 is a free software package composed of tools that can be used to accurately simulate the passage of particles through matter [3]. All the aspects involved with the simulation process have been included in the toolkit:

- the geometry of the system,
- the materials involved,
- the fundamental particles of interest,
- the generation of primary events,
- the tracking of particles through materials and electromagnetic fields,
- the physics processes governing particle interactions,
- the response of sensitive detector components,
- the generation of event data,
- the storage of events and tracks,
- the visualization of the detector and particle trajectories, and
- the capture and analysis of simulation data at different levels of detail and refinement.

At the heart of Geant4 is a large set of physical models to handle the interactions of particles with matter over a very wide energy range. Geant4 is written in C++ and exploits advanced software engineering techniques and object-oriented technology to achieve transparency. This tool offers the user the ability to create a geometric model with a large number of components of different shapes and materials, as well as to define which ones will be sensitive to recording the information (hits) necessary to simulate the responses of the detector (digitization).

Geant4 provides a complete set of physical processes to model the behavior of particles. The user can choose between different approaches and implementations, and modify or add the provided set.

### 2.2.3 Component material neutron yields

The sources4c code is used to determine the neutron yield from  $(\alpha, n)$  reactions based on the geometry of components present in the current PICO-500 design, see Table 2.1. From PICO experience, the materials in these components (and their relative

abundance) makes them primary sources of  $\alpha$  backgrounds.

TABLE 2.1: Neutron Yield determined from the SOURCES4c code for the different detector components (taking into account  $(\alpha, n)$  reactions, spontaneous fission, and delayed neutron emission). The units for the neutron yield are neutrons per gram per parts per billion (ppb) per seconds.

Component	Material	Yield factor [n/g/ppb/s]			
		$^{238}\text{U}$ from $^{234}\text{Th}$	$^{238}\text{U}$ from $^{226}\text{Ra}$	$^{232}\text{Th}$	$^{210}\text{Pb}$
PV	Stainless steel	$1.364 \times 10^{-11}$	$5.242 \times 10^{-12}$	$6.147 \times 10^{-12}$	
Retroreflector	Aluminum	$1.798 \times 10^{-11}$	$1.468 \times 10^{-10}$	$6.147 \times 10^{-12}$	
Mineral Oil	CH <sub>4</sub>	$1.544 \times 10^{-11}$	$1.194 \times 10^{-11}$	$5.710 \times 10^{-12}$	
OV	Quartz	$1.473 \times 10^{-11}$	$1.245 \times 10^{-11}$	$6.312 \times 10^{-12}$	
IV	Quartz	$1.473 \times 10^{-11}$	$1.245 \times 10^{-11}$	$6.312 \times 10^{-12}$	
Active volume	C <sub>3</sub> F <sub>8</sub>	$1.392 \times 10^{-11}$	$2.063 \times 10^{-12}$	$9.152 \times 10^{-13}$	
Piezo Housing	Copper	$1.362 \times 10^{-11}$	$5.219 \times 10^{-13}$	$7.335 \times 10^{-13}$	
PCB Piezo	pcb	$1.503 \times 10^{-11}$	$9.314 \times 10^{-12}$	$4.419 \times 10^{-12}$	
Piezo	PbZr	$1.468 \times 10^{-11}$	$5.785 \times 10^{-12}$	$1.414 \times 10^{-12}$	$5.175 \times 10^{-8}$
Camera	Aluminum	$1.798 \times 10^{-11}$	$1.468 \times 10^{-10}$	$6.147 \times 10^{-12}$	
Lens	Aluminum	$1.798 \times 10^{-11}$	$1.468 \times 10^{-10}$	$6.147 \times 10^{-12}$	
Norite	mixture	$1.601 \times 10^{-11}$	$3.948 \times 10^{-11}$	$2.096 \times 10^{-11}$	

## 2.2.4 Other neutron sources

### $(\gamma, n)$ neutrons

Neutron or alpha particle capture reactions in rocks at SNOLAB produce high-energy photons, which can produce photonuclear reactions within dark matter detectors or produce neutrons near the detector's active volume. The flux of high-energy photons has been measured in the SNO cavern using NaI detectors [38]. In parallel to this work we have determined the flux of gamma particles above 8 MeV with a NaI crystal of 15.6 kg, which we will use as input in our simulations for photonuclear reactions. From this study we have a gamma flux for our simulation with energies from 2 to 100 MeV. Table 2.2 shows the gamma flux used as input for the simulations  $(\gamma, n)$ , whose objective is to determine the production of neutrons in different components of the detector.

### $\mu$ -induced neutrons

The  $\mu$ -rate at SNOLAB is greatly reduced thanks to the 2 km of rock overburden. The  $\mu$  rate was measured in SNO as  $N_\mu = (3.31 \pm 0.01(\text{stat}) \pm 0.09(\text{sys})) \times 10^{-10} \mu/\text{s}/\text{cm}^2$  [4]. The rate of  $\mu$ -induced neutron production depends on the chemical composition and density of the medium through which a  $\mu$  travels. Dependence can be described using a power law [51]:

$$\langle n \rangle = 1.27 \times 10^{-4} \left( \frac{Z^2}{A} \right)^{0.92} n / (\mu \text{ g cm}^{-2}). \quad (2.1)$$

With  $Z = 10$  and  $A = 18$ , the  $\mu$ -induced neutron flux in water at SNOLAB is

$$\langle n \rangle_{\text{H}_2\text{O}} = 20.4 \times 10^{-14} \text{ n/s/g}. \quad (2.2)$$

TABLE 2.2: Gamma flux measured in SNOLAB. Alan work: region from 2 to 8 MeV. Our study: region from 8 to 100 MeV.

Energy interval (MeV)	Gamma Flux ( $y^{-1}cm^{-2}$ )
2-3	$7.96 \times 10^5$
3-4	$2.4 \times 10^4$
4-5	240
5-6	70
6-7	74
7-8	52
8-9	31.66
9-10	1.50
10-11	0.166
11-13	0.0403
13-15	$1.98 \times 10^{-3}$
15-20	$1.14 \times 10^{-3}$
20-30	$1.65 \times 10^{-3}$
30-60	$1.69 \times 10^{-3}$
60-100	$1.08 \times 10^{-3}$

Reference [51] also estimated the  $\mu$ -induced neutron flux from the rock into the SNOLAB underground cavity and is listed in Table 2.3.

TABLE 2.3: The  $\mu$ -induced neutron flux from the rock into SNOLAB cavity.

Energy	> 1.0MeV	> 10MeV	> 100MeV	Total
Neutron flux ( $\times 10^{-9} n/s/cm^2$ )	0.020	0.018	0.005	0.054

## 2.3 Monte-Carlo (MC) Simulations

To model the neutron background for the PICO-500 detector, Monte-Carlo simulations are used to propagate neutrons through components (scaled to match geometry and composition) to determine the background rate from the detector itself. The model of the detector was performed with GEANT4 version 10.03 patch-03 and the compilation was done with gcc 9.3.0 and GNU Make 4.2.1, including the physics lists provided by the advanced\_underground\_physics and neutron\_hp example libraries. The covered physics are suitable for a low-background experiment.

Figure 2.1 shows the original conceptual design of the PICO-500 detector. The inner jar assembly (lower left schematic) will be mounted inside a stainless steel pressure vessel (upper left schematic), which is suspended inside a water tank. The pressure vessel (PV) has a maximum radius of 121.92 cm, a height of 426.72 cm, and a wall thickness of 1.905 cm. The  $C_3F_8$  target is held within the two concentric quartz vessels. The outer vessel has a maximum radius of 23 cm and a height of 200 cm, while the inner vessel has a radius of 21.4 cm and a height of 76 cm. The two jars are coupled together by a stainless steel bellows and flange system. Filling the

space inside the PV, and outside the jars, is around 8 tons of mineral oil.

The right image in Figure 2.1 shows a 3D rendering of the original PICO-500 design, which includes four pressure rated glass windows. Mounted outside the glass will be the camera, the LED ring, and the camera lenses. This interface is important, because the electronics housed in the camera enclosures are known to be hot sources. The view ports have a diameter of 16.51 cm, and will have a stainless steel enclosure mounted to them for all the electronics. In Table 2.4 we list the main properties of the detector components used in our calculations.

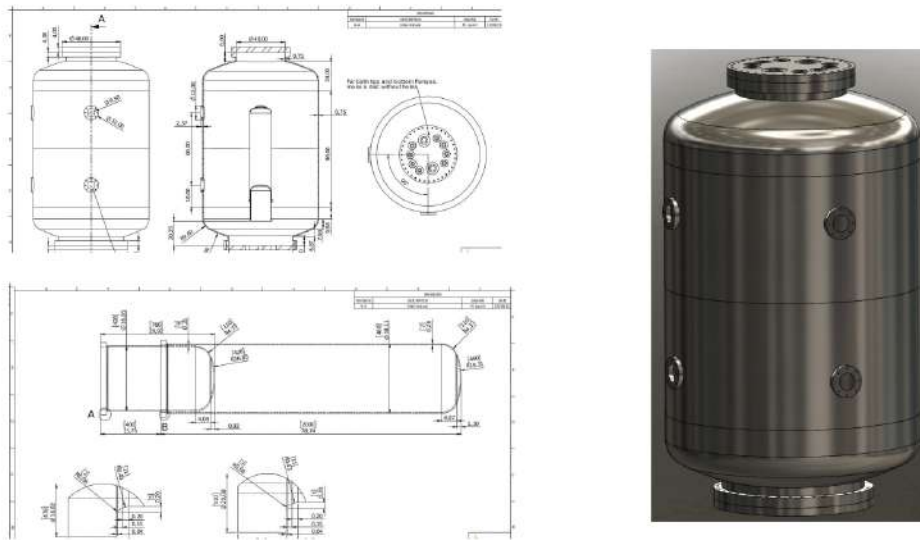


FIGURE 2.1: Conceptual design for the PICO-500 detector, showing the pressure vessel, camera windows, top/bottom flanges, and the quartz jar configuration.

Searching the gamma assay literature from the SNOLAB gamma assay facility [33] we have summarized the impurities of some of the PICO-500 detector materials in Table 2.5. We can calculate the neutron fluence in 1 year for each component of the detector from multiplying the mass, the activity and the neutron yield, in table 2.6 we present the results.

### 2.3.1 New Design for PICO-500

The geometry shown in Figure 2.1 was modified after analyzing the expected background rate from the PV. From simulation, it was observed that the PV size could be mod without a significant increase in background events. The motivation was to reduce the overall cost of the vessel. The new size was determined by simulating a range of PV dimensions, to study the effect on background rates. Figure 2.2 shows the outcome, demonstrating how the background rate is effected by reducing the PV radius.

This study motivated a new design for the detector, see Figure 2.3 for the conceptual design. Along with the reduced radius around the target volume (now around 84 cm), the diameter of the lower region was reduced to 48.75 cm.

TABLE 2.4: Properties of the PICO-500 detector components

Component	Material (g/cm <sup>3</sup> )	Density (m <sup>2</sup> )	Volume (m <sup>3</sup> )	Mass (kg)
Pressure Vessel	Stainless Steel 316L	7.7	0.65	5883
Top Flange	Stainless Steel			225
Bottom Flange	Stainless Steel			1031
Mineral Oil	Mineral Oil	0.77	8.83	6800
Retroreflector	Stainless Steel 316L/retro film			65
Outer Vessel	HSQ 900	2.203	3.37	56.2
Inner Vessel	HSQ 900	2.203	0.94	23.1
Active volume	C <sub>3</sub> F <sub>8</sub>	1.3768	0.26	358
Outer Copper Plate	Cu 101	8.960		274
Inner Copper Plate	Cu 101	8.960		53
Piezo housing	Cu 101/SS	8.960		0.046
PCB Piezo	Kapton	1.755659		0.0013
Piezo	PbZr	7.5		0.0013
Camera	Aluminum	2.700		0.1
Lens	Aluminum	2.700		0.06

TABLE 2.5: Activity values with their respective errors for different detector materials in ppb units taken from SNOLAB page [33].

Component	Concentration [ppb]				Sample Description
	<sup>238</sup> U from <sup>234</sup> Th	<sup>238</sup> U from <sup>226</sup> Ra	<sup>232</sup> Th	<sup>210</sup> Pb	
PV	5.81	0.28	0.77		PICO 56-61 mean
Top Flange	$< 9.86 \times 10^4$	$< 5.84 \times 10^5$	$< 3 \times 10^6$		Simulation
Bottom Flange	$< 3.78 \times 10^4$	$< 3.2 \times 10^5$	$< 3.62 \times 10^5$		Simulation
Camera	$< 61.13$	151.46	371.3		PICO 63
Lens	1003.59	201.04	331.12		PICO 90
Retroreflector	5.61	66.06	73.99	26.5	PICO CW29
Mineral oil	$< 0.0063$	$< 0.007$	$< 0.015$		Simulation
OV	$< 6.89 \times 10^{-4}$	$< 6.89 \times 10^{-4}$	$< 6.28 \times 10^{-4}$		LA-ICP-MS
IV	$< 6.89 \times 10^{-4}$	$< 6.89 \times 10^{-4}$	$< 6.28 \times 10^{-4}$		LA-ICP-MS
C <sub>3</sub> F <sub>8</sub>	$< 0.002$	$< 0.0102$	$< 0.0251$		Simulation
Piezo Housing	18.92	0.35	0.03		PICO 77
PCB Piezo	2.25	17.48	4.94		PICO 35
PbZr	0.34	0.68	$< 1.74$	25.87	PICO CW35
Mine Dust	1230	1380	6450		SNOLAB 59

### Updated top and bottom flanges

Due to significant savings compared to the original price, it was decided to build the top and bottom flanges with another supplier. Due to this, it is important to estimate the minimum purity limit necessary in the stainless steel that will be used for the construction of both flanges. In section 2.3.3 the results for this calculation of purity in the stainless steel of the flanges are presented.



TABLE 2.6: Neutron fluence in each PICO-500 detector component in 1 year, including neutrons from  $(\alpha, n)$  reactions as well as fission and direct neutron decay.

Component	$^{238}\text{U}$ from $^{234}\text{Th}$	$^{238}\text{U}$ from $^{226}\text{Ra}$	$^{232}\text{Th}$	$^{210}\text{Pb}$	Total
PV	13400	294	803		14497
Top Flange	340.3	6.3	20.3		367
Bottom Flange	624	11.6	37.3		673
Retroreflector	206	$1.98 \times 10^4$	$1.24 \times 10^4$		32406
Hydraulic liquid	2390	83.5	257		2730.5
OV	0.0183	0.0155	$6.72 \times 10^{-3}$		0.04052
IV	$7.53 \times 10^{-3}$	$6.36 \times 10^{-3}$	$2.76 \times 10^{-3}$		0.01665
Active volume	252	37.3	16.5		305.8
Copper Plates	144.77	3.93	0.681		149.4
Piezo housing	0.376	$2.67 \times 10^{-4}$	$3.21 \times 10^{-5}$		0.38
PCB	$1.39 \times 10^{-3}$	$6.68 \times 10^{-3}$	$8.96 \times 10^{-4}$		$8.97 \times 10^{-3}$
Piezo	$9.71 \times 10^{-4}$	$1.63 \times 10^{-4}$	$1.02 \times 10^{-4}$	55.35	$1.24 \times 10^{-3}$
Camera	6.84	138	189		333.84
Lens	62.6	102	94.2		258.8

### 2.3.2 Neutron Propagation in PICO-500

For each component in PICO-500, the contribution from  $(\alpha, n)$  reactions are simulated with the neutron yield and energy spectrum's obtained from the SOURCES4C code described in section (2.2.1). These neutrons are generated on the surfaces or in the volume of the detector component and emitted in isotropic directions.

From the physics lists mentioned in section (2.2.2), these neutrons are propagated through the different detector materials before reaching the target volume. The energy deposited into the  $\text{C}_3\text{F}_8$  from nuclear and electron recoils is stored in an output file ("pico.root") for further processing. The output file stores: the energy deposited to each interaction in the  $\text{C}_3\text{F}_8$ , the position of the event relative to the jars, the initial conditions of the primary neutron, and the recoiling element from the event (Carbon or Fluorine).

Using this stored information, the neutron events can be counted and characterized based on the number of recoils that would result in bubble formation (neutron deposits enough energy above the Seitz threshold to a localized region.) Each event counted above threshold is corrected to account for the nucleation efficiency of carbon and fluorine recoils near threshold.

The probability that a neutron generates a background event,  $P_{leak}$ , is defined as the number of events counted above threshold in the  $\text{C}_3\text{F}_8$  fiducial volume (corrected by nucleation efficiency),  $N_{leak}$ , divided by the total number of simulated primary neutrons,  $N_{total}$ :

$$P_{leak} = \frac{N_{leak}}{N_{total}}. \quad (2.3)$$

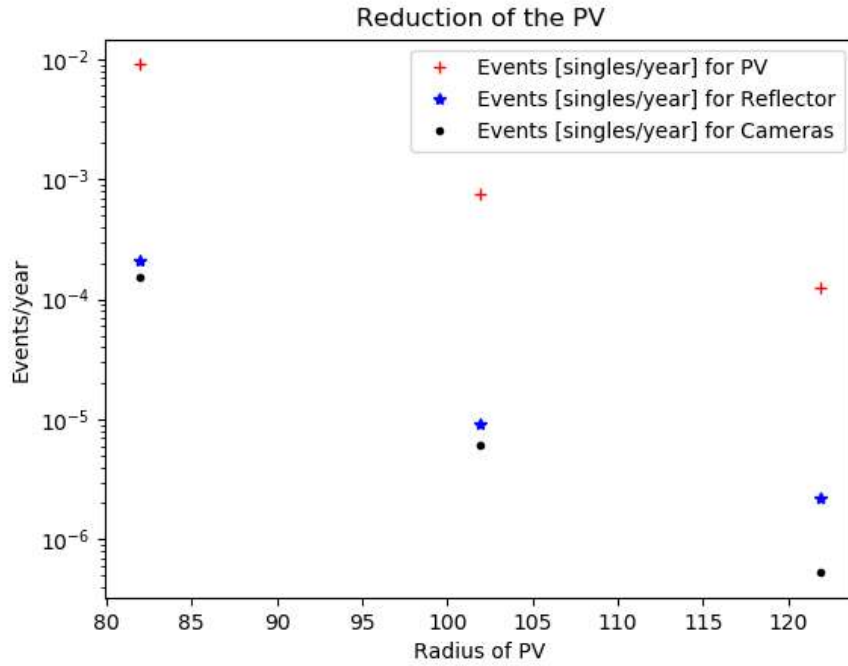


FIGURE 2.2: Behavior of the background rates from decreasing the radius of the pressure vessel. The PV rate is shown in red, the retro-reflector rate (thin layer mounted to inside of PV) is shown in blue, and the rate from the cameras is shown in black.

### 2.3.3 Inner assembly

The results presented in this section show the background rates expected from internal components of the PICO500 detector. The simulated and analyzed components in this section are: PV, Top and Bottom Flanges, Retro-Reflector, Outer and Inner Copper Plates, Outer Vessel (OV), and Inner Vessel (IV), C<sub>3</sub>F<sub>8</sub> and Mineral Oil volumes. In figure 2.4 we show the final model in GEANT4 of our detector on which all the simulations are carried out.

#### PV Neutron Simulations

From section (2.3.1), the simulations of  $(\alpha, n)$  backgrounds from the PV motivated the decision to reduce its dimensions. At the PV,  $2.4 \times 10^8$  neutron events were generated uniformly in the stainless steel volume following the energy distributions of the <sup>232</sup>Th, <sup>238</sup>U from <sup>234</sup>Th and <sup>238</sup>U from <sup>226</sup>Ra chains.

Table (2.10) shows the probability that a neutron background is detected. Thanks to the scale of the pressure vessel, the probability of neutron interactions are very low. Equation 3.4 is used to calculate the number of single bubble events detected in a year of operation from background sources:  $(\alpha, n)$  reactions, spontaneous fission, and delayed neutron emission:

$$Rate = m \cdot Y \cdot A \cdot factor \cdot P_{leak}. \quad (2.4)$$

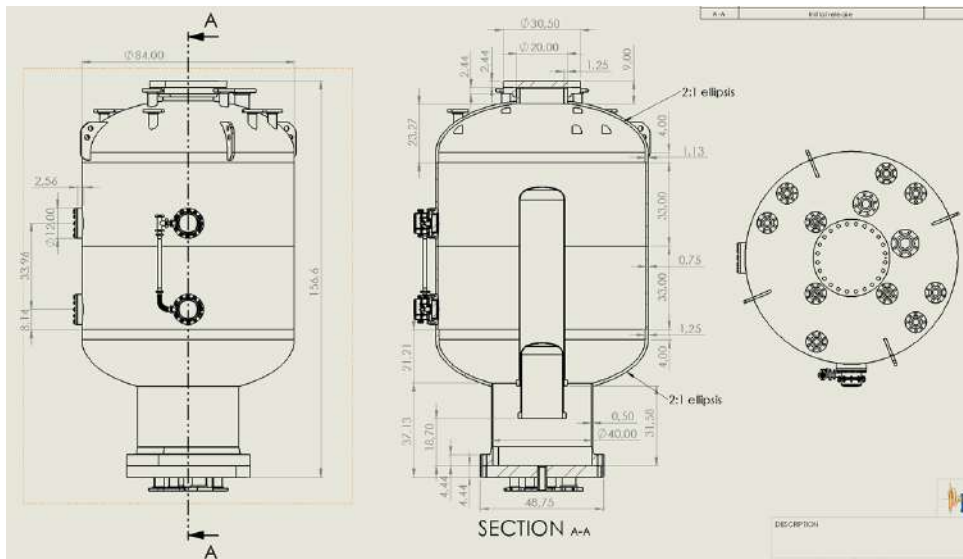


FIGURE 2.3: New model of the PICO-500 pressure vessel.

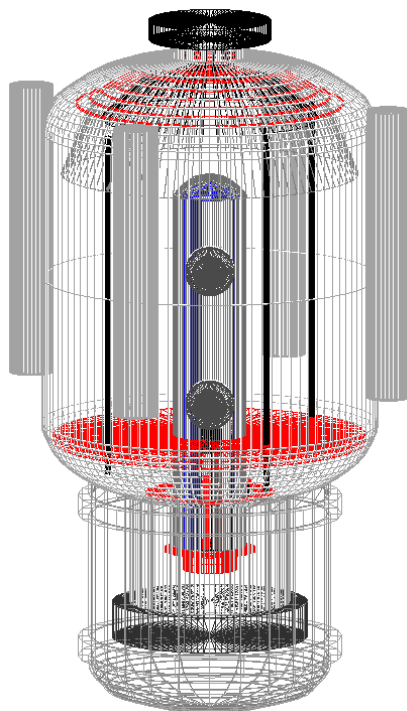


FIGURE 2.4: Current PICO-500 detector model implemented in Geant4 code. Added volume changes: Two retro-reflector cones inside PV, vacuum region outside lower PV, three stainless steel source tubes filled with air, and four high pressure accumulators filled with mineral oil.

Where  $m$  is the mass of the simulated volume in units of grams,  $P_{leak}$  is the Monte Carlo interaction probability (Equation 2.3), and  $factor$  ( $\approx \pi \cdot 10^7$ ) is the live time of the detector in seconds. The yield factor,  $Y$ , is in units of neutrons per second per gram per parts per billion (ppb) [n/s/g/ppb]; Table 2.1 shows the neutron yields

values for each component from each decay chain.  $A$  is the activity of each component for the different decay chains, in units of ppb. The values of the activities for the different components are shown in Table 2.5.

### Top and Bottom Flanges

In order to calculate the purity levels of the stainless steel that will be used for both flanges we simulate from both pieces a significant number of neutrons with energy spectrum obtained from the SOURCES4C code described in section 2.2.1, and thus calculate a maximum quota for the activity of the radioactive chains  $^{232}\text{Th}$  and  $^{238}\text{U}$  once a rate of 0.1 singles events per year has been set.

### Retroreflector Neutron Simulations

In PICO-500, an array of retro-reflectors are used to maximize the light reflecting back to the cameras (illuminating the detector). The retro-reflector includes two concentric conical surfaces and are located in the upper region of the PV, (see Figure 2.5). The retro-reflector is made of three layers: aluminium, polypropylene, and copper.

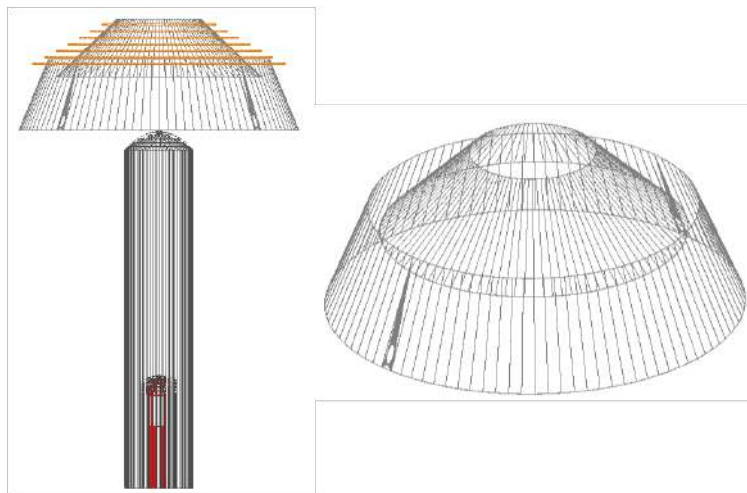


FIGURE 2.5: Retro-reflector cone assembly included in the Geant4 model of PICO-500.

Neutrons are generated in the aluminum layer of the retro-reflectors and scaled to reflect radioactive impurities of the material. The number of single bubble events expected per year of running is calculated using Equation 3.4. Thanks to the large volume of mineral oil and the size of the pressure vessel, the rate of neutrons reaching the  $\text{C}_3\text{F}_8$  from the retro-reflectors and depositing sufficient energy is  $4.06 \times 10^{-4}$  single bubble events per year. Table 2.8 shows the rates of neutrons expected by the different radioactive chains.

### Outer and Inner Copper Plates

Copper plates help distribute heat and keeps the surrounding pipes in the thermal systems at a consistent temperature to minimize thermal lose. The hot region ( $\approx 15\text{ }^\circ\text{C}$ ) is controlled by heating the copper plates using heater wire, which is fed into the top layer of HDPE (high-density polyethylene). The outer copper plate passes heat into the mineral oil volume surrounding the jars, while the inner copper

plate keeps the mineral oil inside the jars warm.

Due to their proximity to the active detection volume and the high mass of copper they have, it is necessary to carry out the pertinent simulations and analyze their contribution to the total background of the detector. For the purpose of the simulations, we consider both pieces as one with an effective mass of copper of 327 kg and  $5 \times 10^4$  neutrons were emitted for each radioactive chain considered with the energy spectrum obtained from the SOURCES4C code described in section 2.2.1. In table 2.8 we show the results of the number of background events per year for the radioactive chains considered in the copper plates.

### OV and IV neutron simulations

As mentioned in Section (2.3), the target volume of  $C_3F_8$  is confined by two concentric quartz jars. Unlike the retro-reflectors, the jar surfaces are in direct contact with the  $C_3F_8$ , and therefore require care to minimize their background contribution, which goes beyond the scope of this review.

Using SOURCES4c, the neutron yield from the upper chain of  $^{238}U$  in quartz is  $1.473 \times 10^{-11}$  n/s/g/ppb (see Table 2.1), at a concentration of  $7 \times 10^{-4}$ ppb, see Table (2.5). The neutron interaction probability from Monte-Carlo is 0.085, obtained by simulating neutrons in the jars. Using Equation (3.4), the rate of background neutrons from the jars is  $1.57 \times 10^{-3}$  single bubble event per year. Table (2.8) shows the results for all decay chains expected from the jars.

### $C_3F_8$ neutrons

During operation, the  $C_3F_8$  volume is held at thermodynamic conditions that maintain a meta-stable state. Passing neutrons can undergo nuclear recoils, which initiate bubble nucleation if the energy deposited is above the threshold. This signal is otherwise indistinguishable from a dark matter candidate, so PICO sets a limit of radioactive contamination allowed before the dark matter signal becomes masked by neutrons ( $\approx 0.1$  single bubble events per year).

To set this limit  $2 \times 10^4$  neutrons are generated in the  $C_3F_8$  volume, emitted isotropically with an energy distribution scaled to match the radioactive chains considered. Table 2.7 shows the probability of leakage of the neutrons produced in the reactions ( $\alpha, n$ ) of the different decay chains considered. Using Equation 3.4, with a yield factor of  $9.152 \times 10^{-13}$  n/s/g/ppb taken from table 2.1 for the radioactive chain of  $^{232}Th$ , a target mass of  $\approx 270$  kg and a  $P_{leak}$  of 0.127, we get a quota for the activity of 0.097 ppb. In Table 2.5 we list the results for the required purity levels in  $C_3F_8$ .

TABLE 2.7: Probability that neutrons produce a WIMP-like event at  $C_3F_8$ .

$P_{leak}$	$^{238}U$ from $^{234}Th$	$^{238}U$ from $^{226}Ra$	$^{232}Th$
$C_3F_8$ in OV	0.108	0.138	0.127

## Mineral Oil

The active region of the PICO500 detector is covered by a mineral oil mass of 6776 kg (Petrochem white oil FG-10), which is connected to a hydraulic manifold to allow periodic pressurization of the detector and to convert bubbles back into droplets. In addition, the active region is kept warm with a mineral oil convection temperature control bath. The oil is heated by a resistive heating element on a copper plate located at the bottom of the PV.

For mineral oil it is necessary to estimate the radio-purity limits since there are no precise measurements of them yet. To do this, we set a value of 0.033 singles events per year for each radioactive chain and we calculated the radio-purity limit. For  $^{232}\text{Th}$  we have generated  $4 \times 10^4$  neutrons isotropically in mineral oil with energy spectrum obtained from the SOURCES4C code (2.2.1), of which 72 reach  $\text{C}_3\text{F}_8$  and produce single bubble events. From equation 2.5, with a Yield factor value of  $5.71 \times 10^{-12}$  obtained from Table 2.1 and a mass value of  $6.8 \times 10^6$  g obtained from Table 2.4, we obtain a radio-purity limit of 0.015 *ppb*. The results for the radio-purity limits in the other radioactive chains are shown in Table 2.5.

### 2.3.4 Optical system

In bubble chambers, when a particle collides with the superheated target liquid, some bubbles can form. These bubbles will be captured with the cameras of the optical system with a high frame rate per seconds. The images obtained by the cameras are used to reconstruct the spatial coordinates of each bubble within the active region.

In our GEANT4 model of the detector we have included four cameras located in steel enclosures to protect them from the water that surrounds our detector and is used to reduce the neutron background. With this distribution of cameras shown in figure 2.3 it is possible to collect information from the entire active volume. In figure 2.6 we can see the model of one of the four cameras in our detector. To carry out the simulations of the components of the cameras we had to emit many neutrons from them since the distances between them and the  $\text{C}_3\text{F}_8$  are large and therefore little statistics are available. For the four lenses,  $11 \times 10^8$  neutrons were emitted with an energy spectrum obtained from the SOURCES4C code in aluminum. From the  $P_{leak}$  obtained from the simulation for the  $^{238}\text{U}$  from  $^{234}\text{Th}$ , a mass value of 55 grams per lens, the activity of this chain in this component obtained from Table 2.5 and using expression (3.4) we obtained a contribution to the background of  $5.69 \times 10^{-8}$  single events per year. As expected, we obtained a small contribution from the camera components to the total background as these are quite far from the active volume. In Table 2.8 we summarize the contribution of each radioactive chain present in each component of the detector.

### 2.3.5 Acoustic system

Due to the need to install piezoelectric acoustic sensors on the walls of the quartz vessel containing the active volume of  $\text{C}_3\text{F}_8$ , it is necessary to analyze its contribution to the total background due to its proximity. In figure 2.7 we show the model built in GEANT for the piezo, where the piezo housing was made of copper, and the piezoelectric material is made of lead zirconate. For this we analyze the contribution of radioactive chains of  $^{238}\text{U}$ ,  $^{232}\text{Th}$  and  $^{210}\text{Pb}$  present in the piezoelectric material.

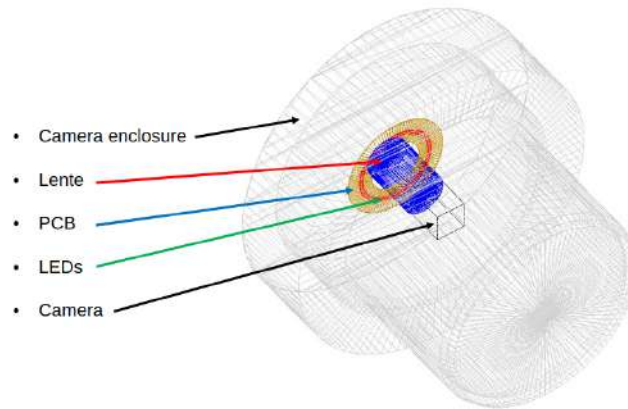


FIGURE 2.6: Configuration of one of the cameras where you can see first the steel enclosure of the camera, the lens, the Printed Circuit Board (PCB) and the LED lights.

Due to the high value of the Yield factor for the neutrons produced by the  $^{210}\text{Pb}$  chain in the piezoelectric, as shown in Table 2.1, these will present the greatest contribution to the total background events. For the PbZr we simulate  $4 \times 10^4$  neutrons from the  $^{210}\text{Pb}$  chain, of which have an interaction probability in the  $\text{C}_3\text{F}_8$  of  $3.23 \times 10^{-3}$ , using the expression 3.4 we obtain 0.178 single events per year. For the other radioactive chains, calculations were made and the results are shown in Table 2.8.

TABLE 2.8: Results for the number of events of a single bubble in the different components of the PICO500 detector.

Component	Number of singles events per year			
	$^{238}\text{U}$ from $^{234}\text{Th}$	$^{238}\text{U}$ from $^{226}\text{Ra}$	$^{232}\text{Th}$	$^{210}\text{Pb}$
PV	$1.0 \times 10^{-07}$	$5.83 \times 10^{-08}$	$2.92 \times 10^{-08}$	
Top Flange	0.033	0.033	0.033	
Bottom Flange	0.033	0.033	0.033	
Cameras	$8.54 \times 10^{-9}$	$5.76 \times 10^{-8}$	$1.48 \times 10^{-7}$	
Lens	$1.14 \times 10^{-7}$	$4.9 \times 10^{-8}$	$4.2 \times 10^{-8}$	
Retroreflector	$1.29 \times 10^{-5}$	$8.26 \times 10^{-05}$	$3.1 \times 10^{-04}$	
Mineral oil	0.033	0.033	0.033	
OV	$1.79 \times 10^{-3}$	$1.48 \times 10^{-03}$	$6.98 \times 10^{-4}$	
IV	$1.03 \times 10^{-4}$	$8.87 \times 10^{-05}$	$4.04 \times 10^{-5}$	
$\text{C}_3\text{F}_8$	0.033	0.033	0.033	
Copper Plates	0.188	$5.19 \times 10^{-3}$	$6.4 \times 10^{-4}$	
Piezo Housing	$1.81 \times 10^{-3}$	$1.37 \times 10^{-6}$	$1.77 \times 10^{-7}$	
PCB piezo	$7.21 \times 10^{-6}$	$5.3 \times 10^{-5}$	$6.12 \times 10^{-6}$	
PbZr	$4.56 \times 10^{-6}$	$8.08 \times 10^{-07}$	$6.56 \times 10^{-7}$	0.181

### Updating of piezos

In this section we show the new distribution of the piezos in two layers at different heights from the top of the IV. The first layer is at a height of 8.6 inches measured from the top of the IV and the second layer is lower at a height of 12 inches. The

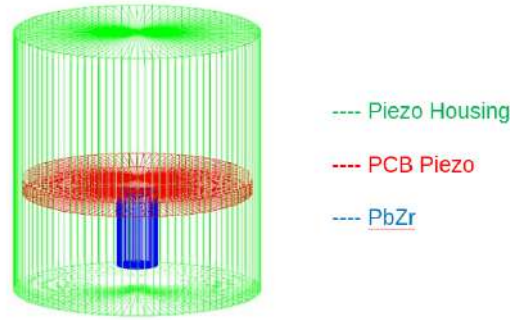


FIGURE 2.7: Piezo model in GEANT4, the Piezo Housing, the Printed Circuit Board (PCB) and the piezoelectric material (PbZr) were considered.

piezos connectors have also been added to the model since we have an activity measurement for the different radioactive chains present in them and we can analyze their contribution to the total background event rate. The piezo connectors were made of stainless steel (304 STN STL) and have a mass of 14 grams. Adding other BPS glass material components to the connector was analyzed, but due to their low mass (0.2 grams), we decided not to consider them. In Table 2.9 we present the results obtained for the number of single bubble events per year in the new configuration proposed for the acoustic system.

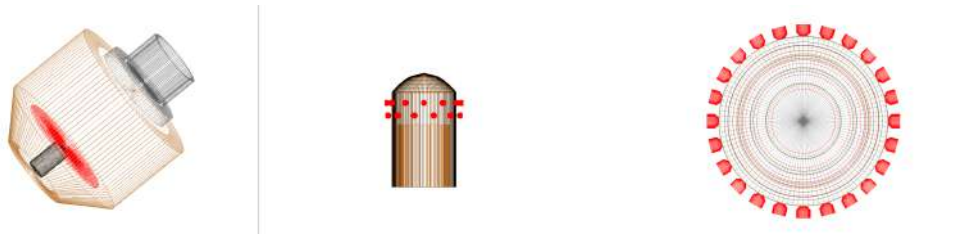


FIGURE 2.8: Left: Piezo model showing the piezo housing, PCB, and piezoelectric material. Center: Front view of the two layers of piezos distributed around the IV. Right: Top view of the array of 24 piezos distributed in two layers at different heights measured from the top of the IV.

TABLE 2.9: Results for the number of single bubble events per year assuming 12 piezos and connectors in each layer.

Position	Number of singles events per year				
	Piezo connector	Piezo housing	PCB	PbZr	Total
1 <sup>st</sup> layer	$3.75 \times 10^{-03}$	$1.94 \times 10^{-02}$	$4.61 \times 10^{-04}$	0.316	0.34
2 <sup>nd</sup> layer	$3.91 \times 10^{-04}$	$1.91 \times 10^{-02}$	$4.59 \times 10^{-04}$	0.321	0.34

We can appreciate that from both layers of piezos similar results are obtained. The difference in heights of 3.4 inches does not become significant in the expected rate of background events.



## 2.4 PICO500 neutron budget and detector material radio purity requirements

For some of the materials in the PICO-500 detector, there is no precise measurement of radio-purity levels. For the purpose of calculation, for each of these components that represent a potential neutron source we are going to allow 0.1 neutron background events in the fiducial volume in 1 year. For each neutron source, the neutron leakage probability,  $P_{\text{leak}}$ , is obtained from Monte-Carlo simulations and summarized in Table 2.10.

The number of background events expected in 1 year for each relevant decay chain is the product of neutron fluence (Table 2.6) and  $P_{\text{leak}}$ . For each component of the detector, the sum of the contribution to the number of events for each chain is calculated and is listed in Table 2.8. The assay results from the current SNOLAB Ge detector provide us with only upper limits for some components, others still need to be determined with greater accuracy.

From equation 2.5 we can establish upper limits of radio-purity within several components of the detector:

$$R = \frac{N}{t \cdot Y_{ppb} \cdot m \cdot P_{\text{leak}}}, \quad (2.5)$$

where  $N \leq 0.1$  is the number of singles events like WIMP expected at  $t = 1$  year of data taking.  $Y_{ppb}$  is the neutron yield from Table 2.1 and  $m$  is the mass taken from Table 2.4. The results are shown in Table 2.5.

TABLE 2.10: Probability of a neutron interacting with the fiducial volume of  $\text{C}_3\text{F}_8$ , for different detector components.

Component	Probability of leakage		
	$^{238}\text{U}$ from $^{234}\text{Th}$	$^{238}\text{U}$ from $^{226}\text{Ra}$	$^{232}\text{Th}$
PV	$1.0 \times 10^{-07}$	$6.67 \times 10^{-08}$	$2.92 \times 10^{-08}$
Retro-Reflector	$5.42 \times 10^{-08}$	$4.17 \times 10^{-09}$	$2.08 \times 10^{-08}$
Mineral oil	0.0016	0.00185	0.00178
Outer Jar	0.0854	0.0122	0.0117
Inner Jar	0.0122	0.0121	0.0118
$\text{C}_3\text{F}_8$	0.11	0.14	0.13
Piezo housing	0.005512	0.00167	0.00408
PCB	0.00493	0.00593	0.0072
PbZr	0.00015	0.0002	0.000275
Camera	$9.37 \times 10^{-10}$	$2.08 \times 10^{-10}$	$3.91 \times 10^{-10}$
Lens	$9.09 \times 10^{-10}$	$2.38 \times 10^{-10}$	$2.21 \times 10^{-10}$

## 2.5 Radon exposure

Radon exposure can lead to surface contamination in PICO-500 from radon diffusion and daughter energy deposition, both leading to  $\alpha$ -decays from  $^{210}\text{Po}$ . These alphas interact with the detector materials and generate  $(\alpha, n)$  neutrons. From Equation

(2.6) the maximum alpha rate from  $^{210}\text{Po}$ ,  $R_{Po}$ , is calculated for each component of the detector to maintain a limit of  $N \leq 0.1$  neutron events observed in  $t = 1$  years of data collection.

$$R_{Po} = \frac{N}{t \cdot Y_{\alpha} \cdot P_{leak}}. \quad (2.6)$$

Where  $Y_{\alpha}$  is the neutron yield, which gives the number of neutrons observed per decay of  $^{210}\text{Po}$  and its units are  $[(\text{Bq} \cdot \text{s})^{-1}]$ .  $P_{leak}$  is the probability that some neutron generated in some component of the detector by the  $(\alpha, n)$  reactions of the  $^{210}\text{Po}$  decays will produce a single bubble event in  $\text{C}_3\text{F}_8$ . Table 2.11 summarizes the maximum alpha rates for the pressure vessel and jars.

TABLE 2.11: Maximum alpha rates from  $^{210}\text{Po}$  for different components of the detector in column four, in column two we can see the values of the neutron yield and the probability of producing a background event by neutrons generated in each of the components is shown in column three.

Component	$Y_{\alpha} [n/\text{Bq} \cdot \text{s}]$	$P_{leak}$	$R_{Po} [\text{Bq}]$
Pressure vessel	$1.53 \times 10^{-8}$	$4 \times 10^{-9}$	$1.63 \times 10^{15}$
Outer jar	$8.95 \times 10^{-8}$	0.077	0.46
Inner jar	$8.95 \times 10^{-8}$	0.011	3.37

### 2.5.1 Radon Diffusion

Over time radon can diffuse into materials. The isotopes in the radon decay chain are short-lived, which means only  $^{210}\text{Pb}$  will build up on a surface layer before beta-decaying to  $^{210}\text{Po}$  and undergoing alpha decay. Therefore, it's assumed that each decay of  $^{222}\text{Rn}$  occupies the same region of the surface layer with one  $^{210}\text{Pb}$  atom. There will be a lag between the  $^{210}\text{Pb}$  decay rate and the alpha-decay of  $^{210}\text{Po}$ , where the latter catches up over time and eventually equilibrium is reached. In this study we assume equilibrium, as this leads to more conservative estimates of tolerance to radon exposure.

Radon diffusion into quartz has been evaluated in Reference [50]. The parameters of interest are the diffusion length  $d_e = 1$  millimeter and the solubility  $S = 10$ . In this case the rate of  $^{210}\text{Po}$  decay,  $R_{Po}$ , is:

$$R_{Po} = d_e \cdot S \cdot R_n \cdot T \cdot A \cdot \frac{1}{\tau}, \quad (2.7)$$

where  $R_n$  is radon concentration,  $T$  is the maximum exposure time in years,  $A$  is the surface area in square meters, and  $\tau = 32.2$  years is the life time of  $^{210}\text{Po}$ . The radon concentration underground at SNOLAB is  $R_n \approx 100 \text{ Bq}/\text{m}^3$  [25]. For the outer and inner jars the outer surface area is  $A = 3.37 \text{ m}^2$  and  $A = 0.94 \text{ m}^2$  respectively. Therefore, the exposure times should be less than 4.4 and 115 years for both jar respectively.

## 2.5.2 Radon daughter deposition

The rate of deposition of  $^{210}\text{Po}$  on surfaces due to exposure to radon in the air depends on many factors, including aerosol concentration in the environment, relative humidity and air velocity. In this note we use an average deposition rate given by  $D = 0.001 \text{ Bq/m}^2$  of  $^{210}\text{Po}$  per  $\text{Bq/m}^3$  of  $^{222}\text{Rn}$  per year of exposure [32].

To limit the amount of  $^{210}\text{Po}$  introduced from  $^{222}\text{Rn}$  daughter diffusion the maximum exposure time in air is:

$$T \leq \frac{R_{Po}}{D \cdot R_n \cdot A}. \quad (2.8)$$

For the outer and inner jar the maximum exposure time in air is  $T = 1.36$  and  $T = 35.85$  years respectively. In the case of the pressure container with an outer surface of  $A = 21\text{m}^2$ , a maximum exposure time in air of  $T = 7.78 \times 10^{14}$  years is obtained.

## 2.6 Radon Emanation

The radon emanation limit for detector materials is constrained by the alpha backgrounds we can tolerate in the outer jar. Radon atoms emanated from the detector materials outside of the OV and inside of the PV interact with quartz and produce  $(\alpha, n)$  neutrons. The maximum radon emanation rate from any source outside of the outer jar is  $R_{Rn} = 0.46 \text{ Bq}$ , as shown in section 2.5 Table 2.11, and is calculated from Equation (2.6) with a neutron yield on quartz  $Y_\alpha = 9.68 \times 10^{-7}$  including the four alphas in the decay chain of  $^{222}\text{Rn}$ . The probability that a simulated neutron on the outer surface of the OV will produce a background event is  $P_{leak} = 7.83 \times 10^{-2}$ .

The radon emanation limit,  $R$ , that can be tolerate is calculated by:

$$R = \frac{R_{Rn}}{A}, \quad (2.9)$$

where  $A$  is the outer surface area for different detector components in units of square meter. For piezo cables, it is assumed that approximately 1  $m$  of cable is needed for each of the piezos. So the radon emanation limit for piezo cables is then:

$$R_{piezo} = 420(\text{mBq})/\text{meter}. \quad (2.10)$$

In table (2.12) we show the results of radon emanation limits for some components of the detector.

TABLE 2.12: Limits on radon emanation for main detector components.

Component	Outer Surface [ $\text{m}^2$ ]	$R$ [ $\text{mBq}/\text{m}^2$ ]
IV	0.94	450
PV	21	20
Retro-Reflector	1.73	240
Retro-Reflector Bottom	2.74	150

## 2.6.1 Cooling System

In this bubble chamber a cooling system is necessary to keep the working temperature at 20° C. This cooling system is made up of two main components, the cooling coil in the upper part together with the Retro-Reflector and a lower pipe wound inside the Copper Tubing Inner. Both cooling pipes contain inside the liquid (+)– Limonene with chemical formula  $C_{10}H_{16}$ , which is cooled by a system external to the detector. Since this liquid is constantly brought into contact with the surrounding air in the SNOLAB cavern as it circulates through the cooling system, the maximum allowed  $^{222}Rn$  concentration must be calculated to guarantee few background events. We did the calculation with expression (2.6) using a Yield factor of  $Y_{alpha} = 9.21 \times 10^{-7}$  (n/decay), a value of  $N = 0.1$  (singles events per year) and the  $P_{leak}$  values shown in table 2.13.

TABLE 2.13: Maximum  $^{222}Rn$  concentration allowed for the refrigerant liquid in the Copper Tubing Inner and the Cooling Coil.

Component	$P_{leak}$	mass [kg]	Radon concentration
Copper Tubing Inner	$6.83 \times 10^{-5}$	1.18	42.72 Bq/kg
Cooling Coil Assembly	$4.75 \times 10^{-7}$	1.45	5000 Bq/kg

It is important to note that in the position of the copper tubing inner, being closer to  $C_3F_8$ , the  $^{222}Rn$  concentration limit allowed for the refrigerant liquid to circulate through it is around 56 Bq and taking into account that the  $^{222}Rn$  concentration in the cavern is  $\approx 100 \text{ Bq/m}^3$ , it is necessary to take actions to minimize contamination.

## 2.7 Other miscellaneous neutron backgrounds

### 2.7.1 Dust deposition

The dust level of the SNO experiment on the inner surface of the AV was  $< 0.001 \text{ g/m}^2$  after cleaning withalconox/water using sponges. Therefore, in our case, we can safely assume a dust deposition rate of  $< 0.01 \text{ g/m}^2/\text{year}$  in SNOLAB (after cleaning). With an exposure time of 4 months, the amount of dust is 0.011 g on the OV outer surface, 0.003 g on the IV, and 0.07 g on the PV. Because the dust comes from the mine, the concentration of uranium and thorium is expected to be the same as that of norite rock, i.e.,  $A = 6.45 \text{ ppm}$  for the  $^{232}Th$ , 1.23 ppm for  $^{238}U$  from  $^{234}Th$  y 1.38 ppm for  $^{238}U$  from  $^{226}Ra$ , taken from table (2.5). The number of background events can be calculated from:

$$N = A \cdot Y_{ppb} \cdot t \cdot m \cdot P_{leak} \quad (2.11)$$

Where  $m$  is the mass of dust that is deposited on the outer surface of the component that is exposed in the cavern and  $t$  is the detector operating time in seconds.  $Y_{ppb}$  is the yield factor for the neutrons generated by the decays of the radioactive chains present in the mass of dust deposited on each component and their units are  $n/g/s/ppb$ . Using the values for  $Y_{ppb}$  in table (2.1) and  $P_{leak}$  values from table (2.10) we calculate the number of background events in 1 year.

TABLE 2.14: Number of background events due to contamination by dust present in the components exposed to the cave.

Component	$^{238}\text{U}$ from $^{234}\text{Th}$	$^{238}\text{U}$ from $^{226}\text{Ra}$	$^{232}\text{Th}$
OV	$5.0 \times 10^{-4}$	$8 \times 10^{-4}$	$2.4 \times 10^{-3}$
IV	$2.4 \times 10^{-5}$	$3.9 \times 10^{-5}$	$9.2 \times 10^{-5}$
PV	$2 \times 10^{-9}$	$4 \times 10^{-9}$	$5 \times 10^{-9}$

### 2.7.2 $(\gamma, n)$ neutrons

In section 2.2.4 we show the gamma flux measured in SNOLAB that we will use in our simulations, which covers the range from 3 to 100 MeV, Figure 2.9 upper right. This gamma flux from the cavern at the PICO detector placement site is emitted from two different configurations depending on the gamma particle formation process, see Figure 2.9 upper left. The less energetic ones, from 3 to 10 MeV were emitted from a cylindrical source around the water shielding and the more energetic ones were emitted from a circular plane source on top of the detector assembly with surface areas of  $1.87 \times 10^6 \text{ cm}^2$  and  $7.23 \times 10^5 \text{ cm}^2$  respectively. The volumes that we are going to consider for the production of neutrons from the incidence of the gamma flux will be the water shield, the pressure container, the mineral oil and the active volume ( $\text{C}_3\text{F}_8$ ).

We first calculate the rate by multiplying the initial flux by the emission surface in each of the two configurations considered. Then with the division between the number of simulated gamma particles and the rate we obtain the time to which the number of simulated particles is equivalent. We then calculated the effective area in each of the volumes considered for neutron formation by photonuclear reactions using expression 2.12 for the normal incidence case, and for the case of the cylindrical source we use as effective area the outer surface of the analyzed volume. Using the lifetime and effective area of each simulation, the kinetic energy spectrum (Figure 2.9 bottom left) of the gammas recorded in each of the four detector components analyzed was normalized. Finally, this normalized kinetic energy spectrum registered in each volume was integrated by the effective cross-section curves for neutron formation in each of the isotopes present in the analyzed component (Figure 2.9 bottom right), multiplied by the number of atoms of each isotope, the isotopic abundance of each isotope and by the probability that a neutron that forms in the component escapes from it and upon reaching the  $\text{C}_3\text{F}_8$  target produces a single event like WIMP per year. To calculate this probability we simulate neutrons isotropically in each component of the considered detector with a uniform energy spectrum of 0.1 to 1 MeV and we define it as the fraction between the number of them that form single bubble events in  $\text{C}_3\text{F}_8$  and the number of neutrons simulated. In the cases of water and PV where no event was recorded in  $\text{C}_3\text{F}_8$ , we assumed 2.3 events to guarantee a confidence level of 90%. This calculation gives us the expected result, the number of events like wimp per year due to neutrons formed in photonuclear reactions.

$$A_{eff} = \pi r [r \cos 25.7^\circ + 2h \sin 25.7^\circ] \quad (2.12)$$

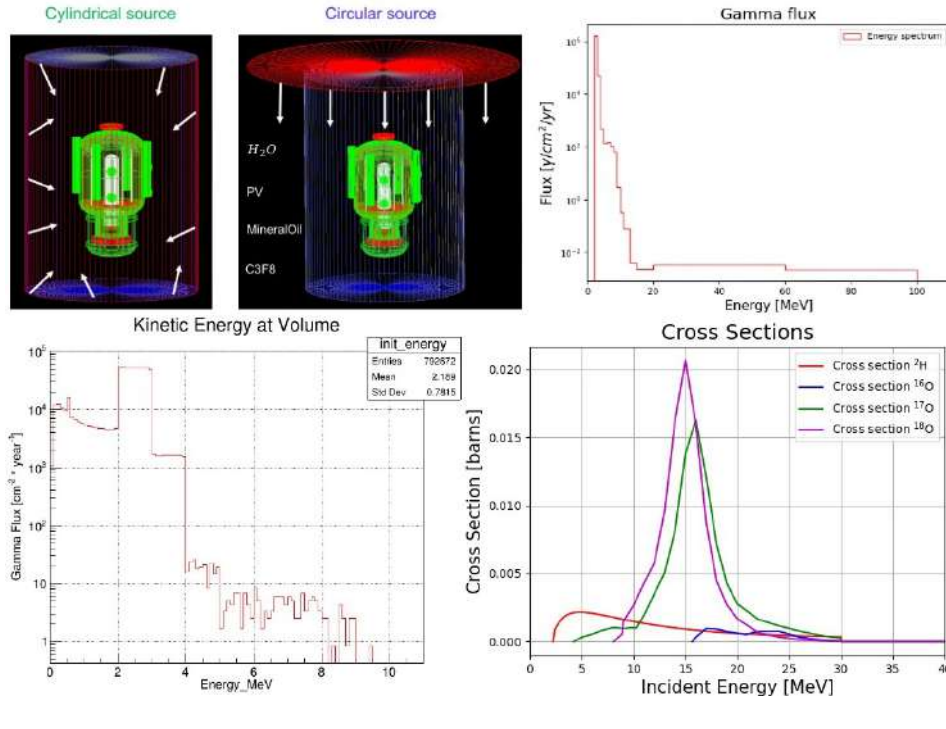


FIGURE 2.9: Upper left: Surfaces used to emit gamma particles. Upper right: Gamma flux of 3 to 100 MeV from the cavern. Bottom left: Kinetic energy spectrum of gamma particles registered in the volume of water shielding. Bottom right: Cross sections for the formation of neutrons in the isotopes present in water.

## 2.8 Total Results

In Table 2.15 we have summarized the information concerning each simulated component, its mass value in kilograms and the total number of events singles like WIMP per year assuming all contributions for each radioactive chain present in the component.

TABLE 2.15: Total contribution to the number of single events like WIMP per year for the simulated principal components of the PICO500 detector.

Component	Mass[kg]	Events singles like WIMP per year
Piezo(24 of them)	0.05 (per piezo)	0.68
Inner and Outer Copper Plates	327	0.197
Piezo connectors (24 of them)	0.014 (per connector)	$2.47 \times 10^{-3}$
OV	56	$2.4 \times 10^{-3}$
PV	5880	$1.63 \times 10^{-3}$
IV	23	$8.81 \times 10^{-5}$
Top and Bottom flanges	1256	$6.18 \times 10^{-6}$
RetroReflector	65	$1.42 \times 10^{-6}$
Lenses	0.22	$4.52 \times 10^{-7}$
Cameras	0.4	$3.62 \times 10^{-7}$
Photo-nuclear reactions		0.038
<b>TOTAL</b>		<b>0.922</b>

## Chapter 3

# Searching for dark matter interactions in the PICO-60 bubble chamber

This section analyzes the results obtained with the PICO-60 bubble chamber in both data runs using CF<sub>3</sub>I and C<sub>3</sub>F<sub>8</sub> targets.

### 3.1 Results on photon-mediated dark matter-nucleus interactions from the PICO-60 C<sub>3</sub>F<sub>8</sub> bubble chamber

PICO-60 has already produce world-leading limits on spin dependent (SD) WIMP-proton interactions with different target fluids, in this section we described the methodology to study photon-mediated dark matter-nucleus interactions. Limits were set using a non-relativistic effective field theory (NREFT).

#### 3.1.1 NREFT

Using the NREFT it is possible to identify all possible elastic DM-nucleus response functions that can be determined in direct search experiments to characterize the DM and thus establish a direct relationship between said responses and the effective theoretical operators that mediate the interaction. The effective field theory in this direct detection case involves a set of four-fermion operators for dark matter interactions with a nucleon in the nucleus in the non-relativistic limit. These operators are higher order in momentum and some of them lead to novel nuclear responses that require new form factors to describe DM interactions with the nucleus. Therefore, within the NREFT now, in addition to the spin-independent and spin-dependent interactions, the angular momentum dependent (LD) and the spin and angular momentum dependent (LSD) interactions must also be included.

We will now give a brief introduction to the non-relativistic effective theory of nucleon-DM interactions. Because we are interested in direct detection by elastic scattering, all effective operators will be four-field operators, of the form

$$\mathcal{L}_{int} = \chi \mathcal{O}_\chi \chi N \mathcal{O}_N N \quad (3.1)$$

The properties of the WIMP and nucleon operators,  $\mathcal{O}_\chi$  and  $\mathcal{O}_N$ , are limited by imposing relevant symmetries. In the moment space, we will take the incoming (outgoing) momentum of  $\chi$  to be  $p$  ( $p'$ ) and of  $N$  to be  $k$  ( $k'$ ). The form of possible interactions is constrained by several symmetries. In particular Galilean invariance imposes that the only combinations of momentum that may appear are those made

from the two invariants momentum transfer  $\vec{q} = p' - p$  and relative incoming velocity  $\vec{v} = \vec{v}_{\chi,in} - \vec{v}_{N,in}$ . Interactions can include the nucleon's spin  $\vec{S}_N$  and, if the dark matter carries intrinsic spin (for instance, if it is a fermion), then  $\vec{S}_\chi$  as well. According to the above, the most general Hamiltonian density for the process can be expressed in terms of a combination of the following five Hermitian operators, which act on the two-particle Hilbert space spanned by tensor products of WIMP and nucleon states:

$$1_{\chi N} \quad i\vec{q} \quad \vec{v}^\perp \quad \vec{S}_\chi \quad \vec{S}_N, \quad (3.2)$$

where  $1_{\chi N}$  is the SI operator,  $\vec{q}$  is the transferred momentum,  $\vec{S}_\chi$  and  $\vec{S}_N$  are the WIMP and nucleon spins, respectively, while  $\vec{v}^\perp = \vec{v} + \frac{\vec{q}}{2\mu_{\chi N}}$  (with  $\mu_{\chi N}$  the WIMP-nucleon reduced mass) is the relative transverse velocity operator satisfying  $\vec{v}^\perp \cdot \vec{q} = 0$ . By including terms that are at most linear in  $\vec{S}_N$ ,  $\vec{S}_\chi$  and  $\vec{v}^\perp$ , we can construct 15 non-relativistic quantum mechanical operators from 3.2.

The most general Hamiltonian density describing the WIMP-nucleus interaction can be written as follows:

$$\mathcal{H}(\mathbf{r}) = \sum_{\tau=0,1} \sum_{k=1}^{11} c_k^\tau \mathcal{O}_k(\mathbf{r}) t^\tau \quad (3.3)$$

where  $t^0 = 1$ ,  $t^1 = \tau_3$  denote the  $2 \times 2$  identity and third Pauli matrix in isospin space, respectively, and the isoscalar and isovector (dimension-2) coupling constants  $c_k^0$  and  $c_k^1$ , are related to those to protons and neutrons,  $c_k^p$  and,  $c_k^n$  by  $c_k^p = (c_k^0 + c_k^1)/2$  and  $c_k^n = (c_k^0 - c_k^1)/2$ . Note that  $c_k^i$  have dimension of mass<sup>-2</sup> due to the normalization convention chosen in [14]. Consequently, we are implicitly encoding in the  $c_k^{p,n}$  coefficients a New Physics scale  $\Lambda$  such that  $c_k^i = \frac{1}{\Lambda^2}$ .

### 3.1.2 From Matlab to Python

The PICO collaboration uses a code written in matlab language to obtain exclusion limits in the WIMP search region. The code uses the python package dark matter direct detection (dmdd) [39] to calculate the differential rate according to the type of coupling, as we can see in equation 3.4:

$$\frac{dR}{dE_R}(E_R) = \frac{\rho_\chi}{m_T m_\chi} \int_{v_{min}}^{v_{esc,lab}} v f_\oplus(\mathbf{v}) \frac{d\sigma_T}{dE_R}(E_R, v) d^3v, \quad (3.4)$$

the units of the differential rate are [counts/kg/sec/keV]. We assume that the terrestrial dark matter velocity distribution  $f_\oplus(\mathbf{v})$  is related to a Galactic velocity distribution  $f(\mathbf{v})$  that is described as a Maxwell-Boltzmann distribution with a smooth velocity cut-off as we can see in equation 3.5. **Scattering cross sections** are treated within the framework of two theories, the ultraviolet theory and the non-relativistic effective field theory (NREFT). In the PICO code, ultraviolet theory is used to draw exclusion limits for the classical SI and SD couplings. It is important to emphasize that for the SI coupling the differential rate must be calculated in the carbon material, target that is not included in the dmdd package libraries and therefore in this case this function was manually introduced in the code.



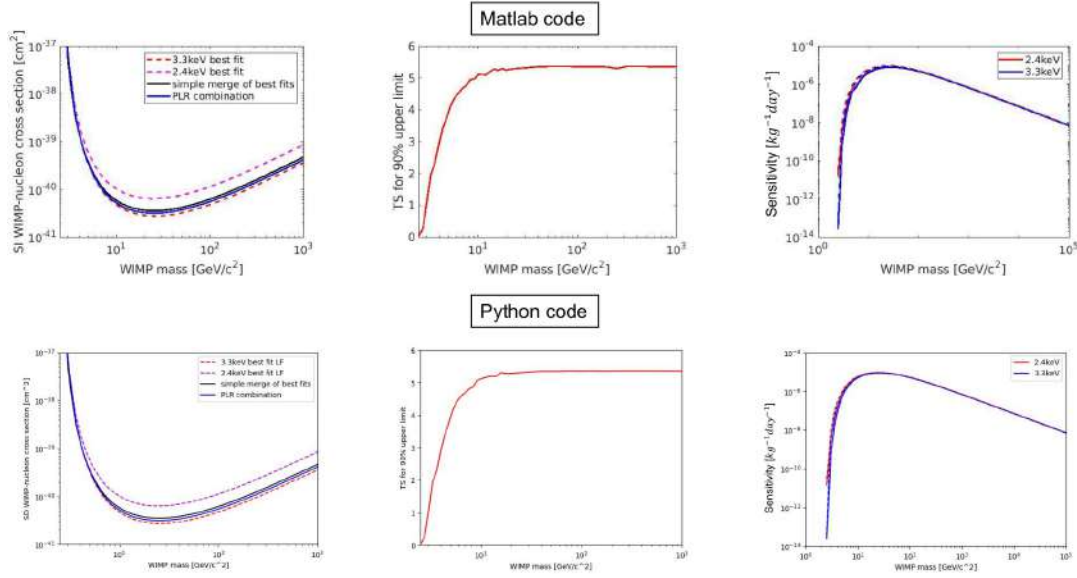


FIGURE 3.1: Exclusion limits for SD coupling using PICO-60 data (left). Statistical test for 90% upper limit (center). WIMP sensitivities (right).

$$f(\mathbf{v}) \propto \left[ \exp\left(-\frac{\mathbf{v}^2 - v_0^2}{v_{rms}^2}\right) - \exp\left(-\frac{v_{esc}^2 - v_0^2}{v_{rms}^2}\right) \right] \quad (3.5)$$

The code uses as input a 5-dimensional tensor (LF) obtained by members of the collaboration with the help of the python package emcee Markov Chain Monte Carlo (MCMC) [37, 43]. The MCMC code is used to fit the calibration data from the last PICO detectors. The output of the fitting is a distribution of sets of four efficiency curves (fluorine and carbon curves at each of the 2.45 and 3.29 keV thresholds) with associated likelihoods. The results of integrating differential rates by efficiency curves (wimp efficiencies) for a range of WIMP masses, both energy thresholds and coupling types (SD/SI) were stored in the LF tensor. In the first dimension of this tensor we have the whole WIMP mass array considered, exactly 42 values. In the second and third dimensions we have for each mass and coupling a matrix of 40x40 values where the WIMP efficiencies obtained with the MCMC are stored. In the fourth dimension, the type of coupling to be considered for the limit calculation is chosen (SI, SD, Anapole, Magnetic, Electric, Millicharge). And finally in the last dimension the energy threshold (2.45 or 3.29 keV) or the log-likelihood of the WIMP integrated efficiencies is chosen.

Due to the fact that the code works with the python packages dmdd and MCMC and due to the inherent advantages of the language itself, we took the task of rewriting all the code in Python, in appendix A, A.5 we show a part of the code.

Once the code was rewritten in Python, we set ourselves the task of reproducing the same limits using the original MATLAB version and the new Python version. As a comparison, we show in Fig 3.1 the results for both codes. Since the compared results are identical and the fact that to obtain them the entire code must be run modularly, we can ensure that our Python code is usable to analyze the data from the PICO detectors.

### 3.1.3 MCMC routine

To calculate the WIMP efficiency, equation 3.6, we use the Monte Carlo code developed by members of the collaboration. This code needs as input a file called "WIMP-spectra\_production" in which the differential rates of the desired coupling for each WIMP mass value considered are stored. For our study, a file was created for each of the specific couplings studied. To obtain the WIMP efficiencies as mentioned above, it is necessary to run the MCMC package. This code uses 34 parameters, 20 fit parameters (nucleation efficiency nodes) and 14 nuisance parameters, see Table 3.1. The nucleation efficiency nodes and nuisance parameters are estimators in a maximum likelihood fit. For more details on the nucleation efficiency model parameters, nuisance parameters and the use of the MCMC it is pertinent to review the thesis of Jin Miaotianzi [43] and the conference proceedings [26].

TABLE 3.1: The best-fit parameters explored by our algorithm. The first row lists the starting nucleation threshold while the next 4 rows are increments from the previous step.

Parameter	Carbon <sub>2,45</sub>	Fluorine <sub>2,45</sub>	Carbon <sub>3,29</sub>	Fluorine <sub>3,29</sub>
0% threshold (keV)	6.92	3.52	7.14	3.64
20% increment (keV)	.06	.12	.03	1.19
50% increment (keV)	3.49	.00	3.82	2.54
80% increment (keV)	1.95	.40	2.22	4.22
100% increment (keV)	.98	2.10	.78	2.16
Nuisance Parameters				
Tolman	PT <sub>2013</sub>	PT <sub>SbBe</sub>	PT <sub>2014</sub>	PT <sub>AmBe</sub>
.25	-.16	.32	1.61	-.43
30ml <sub>2013</sub> <sup>Geo</sup>	30ml <sub>2014</sub> <sup>Geo</sup>	flux <sub>2013</sub> <sup>97keV</sup>	flux <sub>2013</sub> <sup>61keV</sup>	flux <sub>2014</sub> <sup>97keV</sup>
-1.70	.49	.38	-.76	1.00
flux <sub>2014</sub> <sup>61keV</sup>	flux <sub>2014</sub> <sup>50keV</sup>	flux <sub>SbBe</sub>	flux <sub>AmBe</sub>	
.48	-.28	-1.23	-.50	

$$\phi_{SI/SD}(M_\chi, E_T) = \int \frac{dR_{SI/SD}}{dE_r}(E_r, M_\chi) \times \varepsilon(E_r, E_T) dE_r \quad (3.6)$$

The log-likelihood ( $\log \mathcal{L}$ ) can be constructed as the Poisson log-likelihood for observed event counts plus a Gaussian penalty for nuisance parameters.

$$\log \mathcal{L} = \sum_i \sum_j \left[ -v_{i,j}(\{x_{n,p}\}, \{s_k\}) + k_{i,j} + k_{i,j} \log \left( \frac{v_{i,j}(\{x_{n,p}\}, \{s_k\})}{k_{i,j}} \right) \right] - \sum_k \frac{s_k^2}{2} \quad (3.7)$$

where  $k_{i,j}$  is the number of bubbles observed with multiplicity  $j$  observed in experiment  $i$ ,  $v_{i,j}$  are the expected number of events in experiment  $i$  of multiplicity  $j$  given a set of efficiency curves parameterized by the knot positions  $\{x_{n,p}\}$  where  $n$  represents recoiling nuclei species and  $p$  represents percentile, nuisance parameters  $s_k$ , which represent the fraction of assumed systematic error and its standard  $1\sigma$  value. We can define a corresponding goodness of fit  $\chi^2$  in the usual manner as

$$\chi^2 = -2 \cdot LL, \quad (3.8)$$

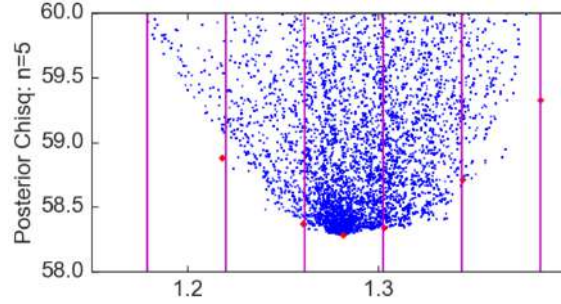


FIGURE 3.2: Parameter 3; Fluorine setpoint at 20% efficiency

Given equation 3.7 and 3.8, we can treat  $\chi^2$  as a cost function based on  $\{x_{n,p}\}$  and nuisance parameters  $s_k$ . Our goal is to minimize cost function with floating efficiency nodes as well as nuisance parameters and then probe probability distribution around optimum in order to find the WIMP sensitivity. The "fast burn-in" technique was used to explore the probability distribution around the optimum in the high-dimensional space, see Jin's thesis [43]. In Fig 3.2 we show the modified MCMC method used in this analysis, in which we take advantage of MCMC code to transverse high-dimensional spaces efficiently and then we apply a routine to sample the points on the log-likelihood boundaries for each. parameter then feedback into the first process

### 3.1.4 Comparing previous results for SD and SI couplings

Once we understood the MCMC code developed by Daniel Durnford our first task was to run it for classical SI/SD couplings to obtain our own LF matrix for these couplings, similar to what Jin Miaotianzi did [43]. WIMP efficiencies were obtained for each mass, threshold and coupling type with our own MCMC code routine. The following parameters were used for Stage 1, 100 for the number of bins, 2 for the proposal scale factor and 5 for the number of steps, for more details about this see see Jin's thesis [43]. In Figure 3.3, we show the probability distribution obtained for the WIMP efficiencies at the 2.4 keV threshold for a mass of 19 GeV and SD coupling. As we saw before, for each value of mass, coupling and energy threshold we will have a probability distribution like the one shown in Fig 3.3. In order to store each of these distributions in a single file (LF tensor) and subsequently draw the exclusion limits for the entire mass spectrum, it was necessary to take a representative sample. To do this we used the probability distribution in the combination of both thresholds, Fig 3.4, and then the entire space was divided into a matrix of 40x40 bins, in each of which we took the point of highest probability. In Figure ??, we show the result after binning (red) and compare with the distribution obtained by Jin (blue) for the same mass, threshold and coupling.

Using these distributions we can construct the likelihood surfaces as a function of WIMP detection efficiency at 2.45 and 3.29 keV. WIMP detection efficiencies,  $\phi$ , in units of detected WIMPs per kg-day of exposure per picobarn of WIMP-nucleon scattering cross section, are derived from the calibration MCMC output by integrating the efficiency curves over the nuclear recoil spectrum from an astrophysical WIMP flux for an array of potential WIMP masses. The two-dimensional WIMP detection efficiency space is divided into bins and within each bin the maximum likelihood set of efficiency curves that fall within that bin is found. The likelihood

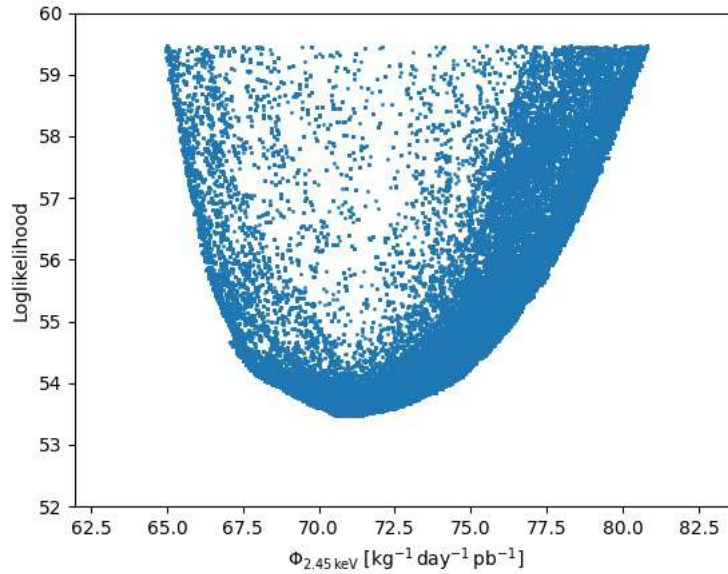


FIGURE 3.3: Probability distribution obtained for WIMP efficiency at 2.4 keV threshold, 19 GeV mass and SD coupling.

surface thus created retains any covariance between the efficiency at the two thresholds from the neutron calibration. In Figure 3.4, we show the likelihood surfaces obtained for SD coupling and a mass of 19 GeV. As a comparison, we show the same surfaces obtained with the original code. It is important to emphasize that in this analysis of the parameter space, its exploration is not done the same, since the code we use developed by Daniel Durnford does not behave exactly the same as the one used by Jin. But the important thing here is that we focus on regions of maximum probability, and if we look closely we have practically the same results.

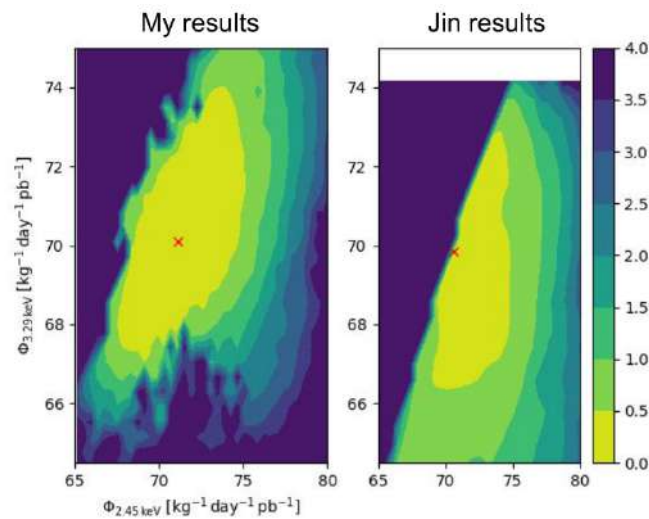


FIGURE 3.4: Likelihood surfaces obtained for SD coupling and a mass of 19 GeV.

The standard halo parametrization is used, with the following parameters: local dark matter density  $\rho_D = 0.3 \text{ GeV}c^{-2}\text{cm}^{-3}$ , galactic escape velocity  $v_{esc} = 544 \text{ km/s}$ , velocity of the earth with respect to the halo  $v_{Earth} = 232 \text{ km/s}$ , and characteristic WIMP velocity with respect the halo  $v_0 = 220 \text{ km/s}$ .

Once the WIMP efficiencies were obtained for each mass, threshold and coupling, we set the task of filling in our own 5-dimensional LF tensor. Using this tensor and the original one obtained by Jin, we were able to compare the exclusion limits obtained by us with those obtained by Jin and published in the last PICO-60 paper [8]. Figure 3.5 shows the results of this comparison for classical SI/SD couplings. As we can see we have obtained excellent agreement using our own MCMC code routine.

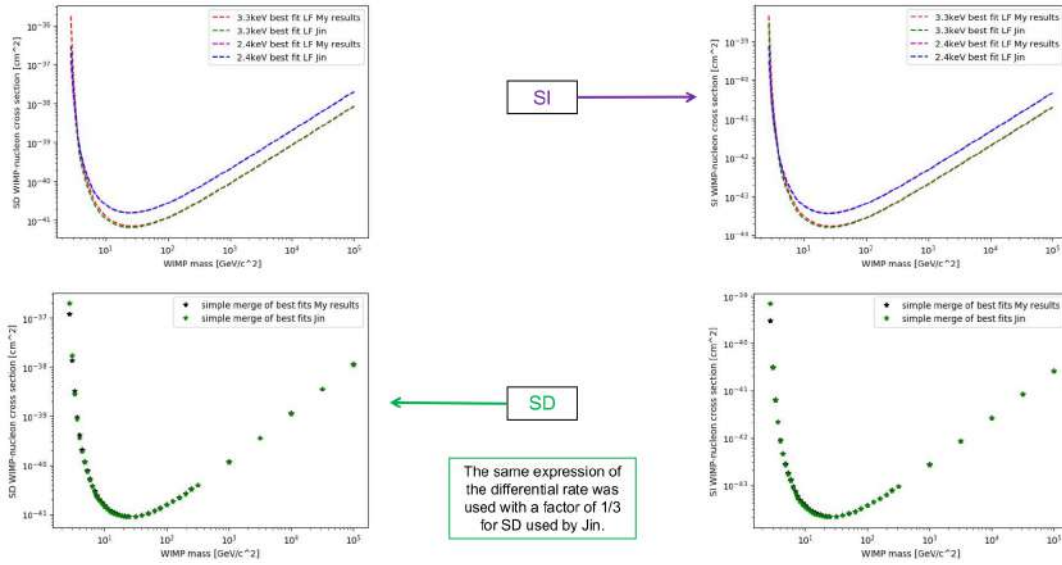


FIGURE 3.5: Exclusion limits of both energy thresholds for SD coupling of Jin's and our results(upper left). SI coupling results for both thresholds of Jin's and our results(upper right). SD coupling exclusion limits for the simple merge of best fits of both results(lower left). SI coupling limits for the simple merge of best fits of both results(lower right).

### Ultra violet (UV) and NREFT for SD interaction

As we saw before, to compare our results with those obtained by Jin for the SD interaction we used the same factor of 1/3 in the expected rate of events. The UV theory of the python package dmdd was used to obtain the expected event rate for the published SD and SI couplings. Due to this and the fact that we will be using NREFT and the python package WIMpy we decided to compare the results obtained with both theories and python codes for these couplings. Figure 3.6 shows the results of these comparisons for the expected rate of events and the corresponding exclusion limits.

As we can see, there is a complete agreement between the results for both codes using the NREFT. However, the UV theory disagrees with the results obtained with or without factor. It is worth noting that the results for the expected rate of events for the UV theory are higher, which implies a stronger limit. As part of our comparisons,

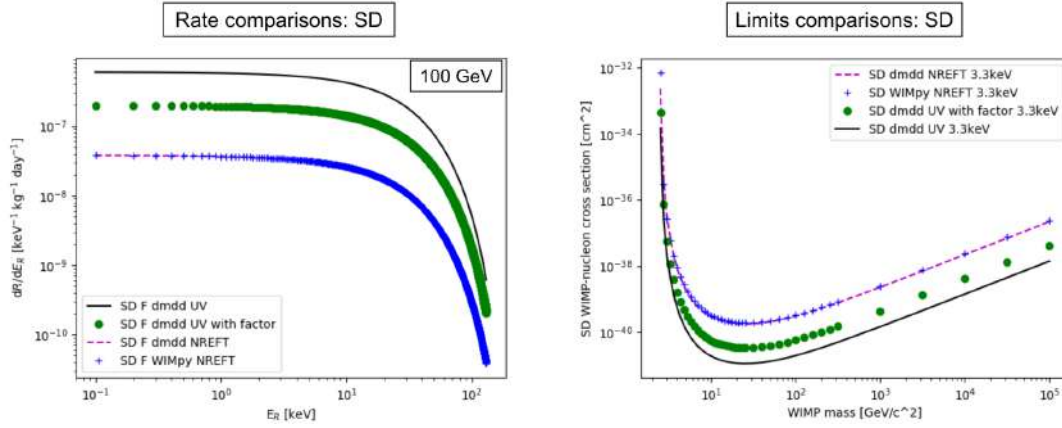


FIGURE 3.6: Expected event rate for SD coupling considering dmdd and WIMpy codes for UV and NREFT theories (left).

the same analysis was done for the SI coupling and instead we obtained a complete correspondence between both packages, the UV theory and the NREFT. It would be recommendable to review the results published by PICO for the SD coupling and compare them when using a NREFT.

### 3.1.5 WIMpy\_NREFT code to study specific couplings and NREFT operators

In addition to the dmdd code, we have included the WIMpy\_NREFT [46] python code. This allows us to calculate Dark Matter-Nucleus scattering rates in the framework of NREFT [36, 34, 14] including operators from  $\mathcal{O}_1$  to  $\mathcal{O}_{11}$ , as well as millicharged, electric/magnetic dipole, and anapole interactions. Considering a NREFT, direct detection experiments have a more general way to characterize their results. NREFT provides a detailed formulation to describe all possible dark matter-nucleus couplings and a better description of the nuclear response. Instead of the classical two couplings SI and SD, six nuclear response functions arise from different effective operators. In this framework, the nucleus is not treated as a point-like particle but its composite nature is reflected. Table 3.2 shows the main non-relativistic effective operators up to the twelfth operator, where  $\mathcal{O}_1$  represents the standard SI interaction and  $\mathcal{O}_4$  the standard SD. It is important to note that in the WIMpy\_NREFT code we have a greater availability of target materials, including carbon. This gives us the possibility to study other types of specific couplings in  $C_3F_8$  using the PICO-60 data. WIMpy and dmdd have been tested using the NREFT in both and they give the same results. The results for the differential rates of different operators ( $\mathcal{O}_1$ ,  $\mathcal{O}_4$ ,  $\mathcal{O}_9$ ,  $\mathcal{O}_{11}$ ) in the framework of an NREFT using both codes are shown in Fig 3.7.

#### NREFT-derived specific interactions

The NREFT formalism incorporates more complex interactions. If the Standard Model (SM) photon is responsible for the DM-nucleon interaction, relevant cases arise from using a certain effective operator or combining some of them, e.g. anapole, electric or magnetic dipole, and millicharged DM.

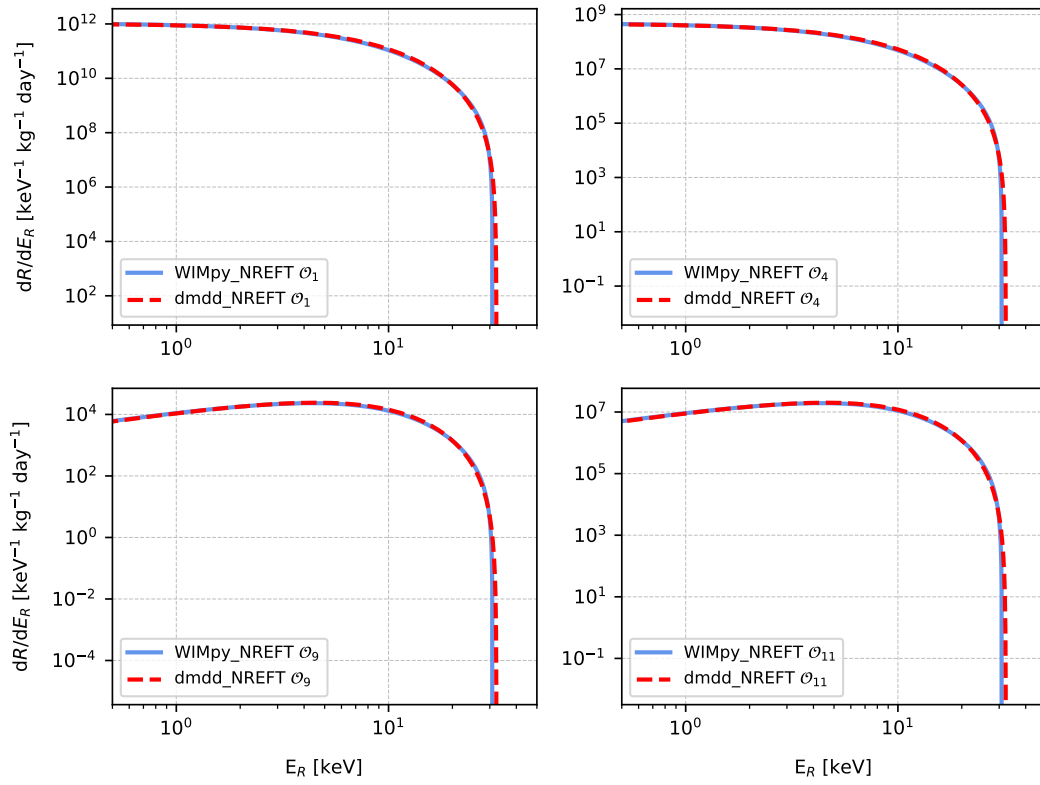


FIGURE 3.7: Comparison for different operators using the NREFT in WIMpy (blue) and dmdd (red) for a WIMP mass of 10 GeV.

### 3.1.6 DM with an anapole moment

The anapole moment is the lowest electromagnetic moment allowed for a Majorana particle. It is generated by a toroidal electric current which confines the magnetic field within a torus; basically, it is equivalent to having a particle with a toroidal dipole moment. If the DM particle is assumed to be a Majorana fermion scattering off a nucleus via a spin-1 mediator that kinetically mixes with the photon, then the effective interaction is written as:

TABLE 3.2: NREFT operators, with  $\vec{v}^\perp$  the component of the velocity perpendicular to the momentum transfer,  $i\frac{\vec{q}}{m_N}$  the momentum transfer,  $\vec{S}_\chi$ -DM spin and  $\vec{S}_N$ -nucleon spin.

Operators	Operators
$\mathcal{O}_1 = 1_\chi 1_N$	$\mathcal{O}_7 = \vec{S}_N \cdot \vec{v}^\perp$
$\mathcal{O}_2 = (\vec{v}^\perp)^2$	$\mathcal{O}_8 = \vec{S}_\chi \cdot \vec{v}^\perp$
$\mathcal{O}_3 = i\vec{S}_N \cdot \left(\frac{\vec{q}}{m_N} \times \vec{v}^\perp\right)$	$\mathcal{O}_9 = i\vec{S}_\chi \cdot \left(\vec{S}_N \cdot \frac{\vec{q}}{m_N}\right)$
$\mathcal{O}_4 = \vec{S}_\chi \cdot \vec{S}_N$	$\mathcal{O}_{10} = i\vec{S}_N \cdot \frac{\vec{q}}{m_N}$
$\mathcal{O}_5 = i\vec{S}_\chi \cdot \left(\frac{\vec{q}}{m_N} \times \vec{v}^\perp\right)$	$\mathcal{O}_{11} = i\vec{S}_\chi \cdot \frac{\vec{q}}{m_N}$
$\mathcal{O}_6 = \left(\vec{S}_\chi \cdot \frac{\vec{q}}{m_N}\right) \left(\vec{S}_N \cdot \frac{\vec{q}}{m_N}\right)$	$\mathcal{O}_{12} = \vec{v}^\perp \cdot \left(\vec{S}_\chi \times \vec{S}_N\right)$

$$\mathcal{L}_A = c_A \bar{\chi} \gamma^\mu \gamma^5 \chi \partial^\nu F_{\mu\nu}, \quad (3.9)$$

where the  $\chi$  spinor represents the Majorana DM particle,  $c_A$  the anapole moment coupling strength and  $F_{\mu\nu}$  the electromagnetic field tensor. The anapole moment has a unique feature, it interacts only with external electromagnetic currents  $\mathcal{J}_\mu = \partial^\nu F_{\mu\nu}$  [42]. In the non-relativistic limit, the effective operator for anapole interactions,  $\mathcal{O}_A$ , is a linear combination of the momentum-independent operator  $\mathcal{O}_8$  and the momentum-dependent  $\mathcal{O}_9$ :

$$\mathcal{O}_A = c_A \sum_{N=n,p} (\mathcal{Q}_N \mathcal{O}_8 + g_N \mathcal{O}_9), \quad (3.10)$$

where  $\mathcal{Q}_N$  is the nucleon charge ( $\mathcal{Q}_p = e$ ,  $\mathcal{Q}_n = 0$ ) while  $g_N$  is the nucleon  $g$ -factor ( $g_p = 5.59$  and  $g_n = -3.83$ ). This interaction is expressed as  $\mathcal{O}_A = c_A [e \mathcal{O}_8 + (g_p + g_n) \mathcal{O}_9]$  for  $\text{C}_3\text{F}_8$ . It is possible to parametrize the coupling strength in terms of an anapolar effective cross-section as:

$$\sigma_A = \frac{c_A^2 \mu_N^2}{\pi} \quad (3.11)$$

### DM with a magnetic dipole moment

Contact interactions ( $|\vec{q}| \ll m_\phi$ ), where  $m_\phi$  is the mass of the mediator, are independent on the exchanged momentum, however long-range interactions ( $|\vec{q}| \gg m_\phi$ ) are enhanced at small momentum transfer. Examples of long-range interactions are DM with electric or magnetic dipole moments and millicharged DM. These arise from the exchange of a massless mediator, where the propagator term enhances the interaction. Considering the DM particle as a Dirac fermion acquiring a magnetic dipole moment, the effective interaction is given by:

$$\mathcal{L}_{MD} = \frac{\mu_\chi}{2} \bar{\chi} \sigma^{\mu\nu} \chi F_{\mu\nu}, \quad (3.12)$$

where the spinor  $\chi$  represents the Dirac DM particle,  $\mu_\chi$  is the magnetic moment coupling, and  $\sigma^{\mu\nu} = \frac{i}{2} [\gamma^\mu, \gamma^\nu]$ . Similar to the anapole moment scenario, the non-relativistic shape of the effective operator for magnetic dipole interactions,  $\mathcal{O}_{MD}$ , can be expressed in terms of contact operators in the NREFT.  $\mathcal{O}_{MD}$  depends on the operators  $\mathcal{O}_1$ ,  $\mathcal{O}_4$ ,  $\mathcal{O}_5$ , and  $\mathcal{O}_6$  and is expressed as follows:

$$\mathcal{O}_{MD} = 2e\mu_\chi \sum_{N=n,p} \left[ \mathcal{Q}_N m_N \mathcal{O}_1 + 4\mathcal{Q}_N \frac{m_\chi m_N}{q^2} \mathcal{O}_5 + 2g_N m_\chi \left( \mathcal{O}_4 - \frac{1}{q^2} \mathcal{O}_6 \right) \right] \quad (3.13)$$

Likewise, the magnetic moment coupling can be used to obtain an effective cross-section:

$$\sigma_{MD} = \frac{\mu_\chi^2}{\pi} \quad (3.14)$$

### DM with millicharge

Millicharged particles have attracted interest since they represent elegant extensions to the Standard Model (SM). A millicharged DM particle would carry a fraction of



the electron charge and many searches have been performed [55, 20, 48, 23]. Considering a Dirac fermion, the interaction Lagrangian of the millicharged DM is given by:

$$\mathcal{L}_{\mathcal{M}} = e\epsilon_{\chi}A_{\mu}\bar{\chi}\gamma^{\mu}\chi \quad (3.15)$$

where  $A_{\mu}$  is the SM photon and  $\epsilon_{\chi}$  is the millicharge (a fraction of the electron charge  $e$ ). The non-relativistic millicharge operator,  $\mathcal{O}_{\mathcal{M}}$ , is only a function of the  $\mathcal{O}_1$  operator but with a  $q^2$  dependence:

$$\mathcal{O}_{\mathcal{M}} = e^2\epsilon_{\chi}\frac{1}{q^2}\mathcal{O}_1 \quad (3.16)$$

In the same way, dark matter millicharge coupling can be used to obtain an effective cross section:

$$\sigma_{\mathcal{M}} = \frac{\epsilon_{\chi}^2}{\mu_N^2 \cdot \pi} \quad (3.17)$$

### DM with electric dipole moment

Likewise, assuming a Dirac fermion as the DM particle acquiring an electric dipole moment, the effective Lagrangian for the coupling can be written as:

$$\mathcal{L}_{\mathcal{ED}} = \frac{d_{\chi}}{2}i\bar{\chi}\sigma^{\mu\nu}\gamma^5\chi F_{\mu\nu}, \quad (3.18)$$

where  $d_{\chi}$  is the electric dipole moment coupling. A DM particle with a permanent electric dipole moment must have a non-zero spin, and  $d_{\chi}$  satisfies time-reversal and parity violation [60]. The non-relativistic operator participating in this interaction,  $\mathcal{O}_{\mathcal{ED}}$ , is a function of the  $\mathcal{O}_{11}$  operator. It is expressed as:

$$\mathcal{O}_{\mathcal{ED}} = 2ed_{\chi}\frac{1}{q^2}\mathcal{O}_{11} \quad (3.19)$$

Similarly, electric moment coupling can be used to obtain an effective cross section:

$$\sigma_{\mathcal{ED}} = \frac{d_{\chi}^2}{\pi} \quad (3.20)$$

### Results for specific interactions

The first step to obtain the exclusion limits for these specific couplings was to run the MCMC routine for the entire mass spectrum and both energy thresholds. To run the MCMC for each coupling we use the expressions in Appendix A, section A.1 to calculate the expected event rates for each mass. As seeds for each coupling we used the expressions in the Appendix A, section A.6, where  $c_A$  is the Anapolar coupling constant,  $\epsilon_{\chi}$  the millicharge coupling constant,  $\mu_x$  the magnetic dipole constant, and  $d_x$  the electric dipole constant. Following the original PICO code, we defined each coupling constant from the same cross section seed used for the SI/SD couplings with a value of  $1 \times 10^{-43} \text{ cm}^2$ . As a result, we obtained the WIMP efficiencies at the combination of both thresholds in the form of the likelihood surfaces. Figure 3.8 shows the likelihood surfaces obtained for the four specific couplings under study for a 10 GeV mass. Each point of these surfaces represents the integral of the

differential rate for each coupling by a specific efficiency curve with its respective likelihood on the color scale. The likelihood surfaces are marginalized over as nuisance parameters within the PLR, after being convolved with a two-dimensional Gaussian function reflecting experimental uncertainty in the PICO-60 thermodynamic threshold. The code A.7 shows the section of the python code where this calculation is performed. Using the WIMP efficiencies obtained from the MCMC and stored in the LF tensors, exclusion limits in units of couplings can be obtained at a 90% confidence level using the expressions in the code A.8, for both thresholds.

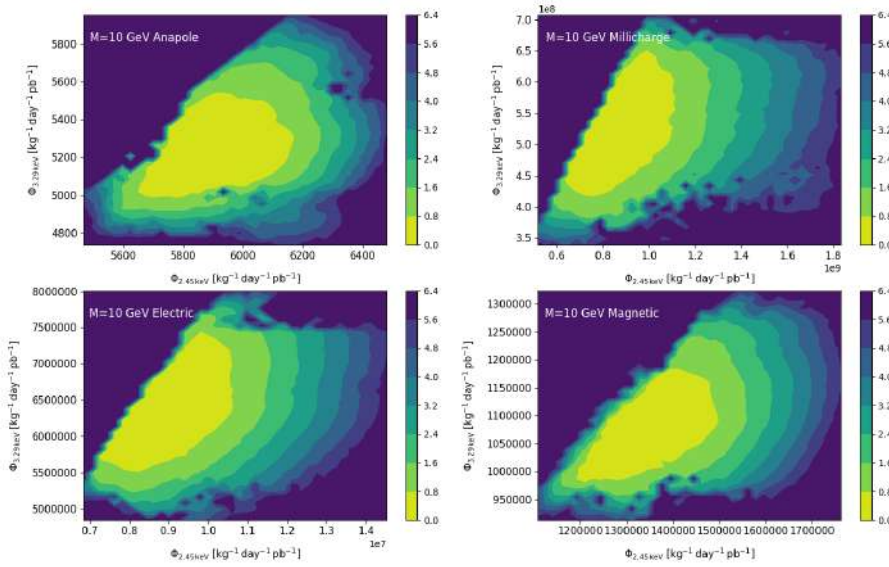


FIGURE 3.8: Contour plot of integrated efficiency  $\phi$  at 2.45 and 3.29 keV. Contour layers have been color coded to represent the difference in  $\chi^2$  with respect to the minimum. Details in the outer boundary of the plot are subject to statistical fluctuations.

It is important to emphasize that the code and limits obtained for each coupling are independent of the cross section seed used ( $1 \times 10^{-43} \text{ cm}^2$ ). The pertinent tests were made running the MCMC with different coupling constant values and the result was always the same. In this way, we demonstrated what was expected, that the exclusion limits obtained depend only on the target, the operators involved and the kinematics for each type of coupling.

The code we have developed, for practicality, accepts as input the name of the desired coupling and, at the end of its execution, it returns the graphs corresponding to the exclusion limits and parameters used in the PLR. Fig 3.9 includes upper bounds on photon-mediated interactions derived by using the NREFT with the SHM, which shows that anapolar coupling would impose the strongest limits. As introduced in section 3.1.5 we will use the WIMpy\_NREFT code to study photon-mediated interactions. Figure 3.10 shows the rates of photon-mediated interactions, obtained with WIMpy\_NREFT for a 5 GeV/ $c^2$  DM particle. To compare our results we use the data reported by the XENON-1T [21] and DEAP-3600 [2] experiments. XENON-1T and DEAP-3600 are leading experiments in the field of SI interactions with noble liquids, using xenon and argon, respectively. Results for the specific couplings studied at

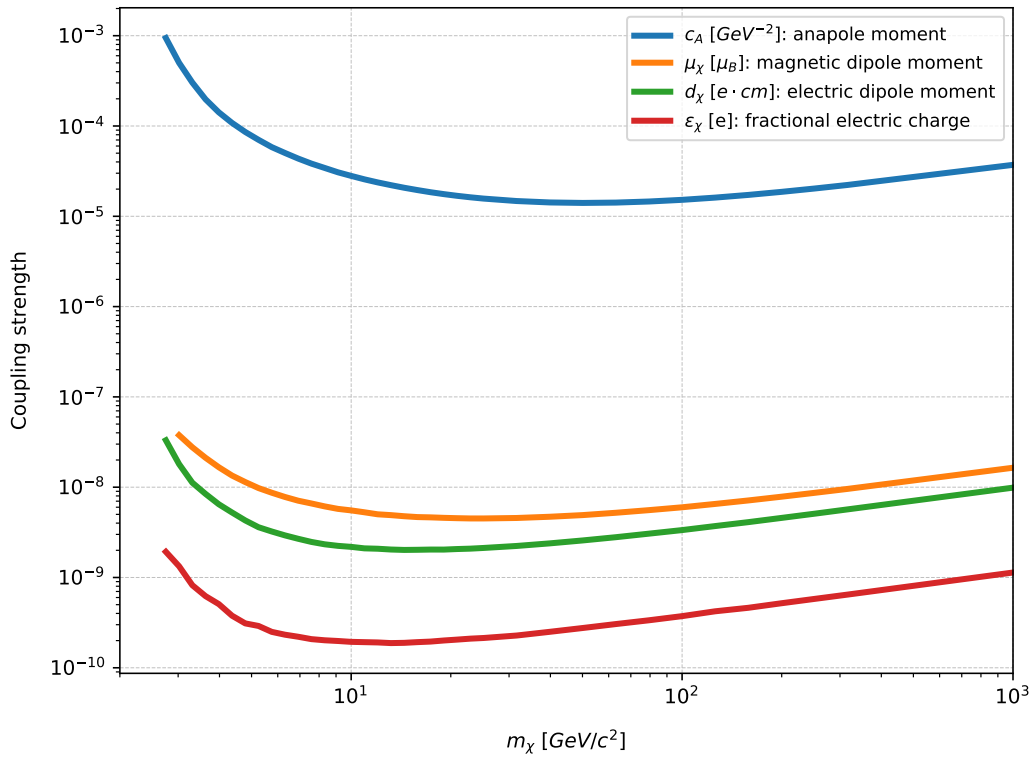


FIGURE 3.9: Limits on the coupling strength for specific interactions using the SHM.

a 90% confidence level using the profile likelihood analysis for PICO-60 C3F8 data are shown in Figure 3.11. The results obtained show the excellent physical reach of bubble chamber technology using fluorine targets. Assuming that the DM is a fermion with electromagnetic moments, the lowest order electromagnetic interaction is through the magnetic or electric dipole moments. This analysis of the PICO-60 bubble chamber establishes primary limits for these couplings, as low as  $2.1 \times 10^{-9} \text{ GeV}^{-1}$  for masses between  $2.7 \text{ GeV}/c^2$  and  $11.7 \text{ GeV}/c^2$  (electrical) and  $5.8 \times 10^{-9} \text{ GeV}^{-1}$  between  $3 \text{ GeV}/c^2$  and  $9.5 \text{ GeV}/c^2$  (magnetic). On the other hand, for a Majorana fermion the only possible electromagnetic moment is the anapolar moment, since the magnetic and electric dipole moments disappear. The PICO-60 experiment imposes leading limits for masses between  $2.7 \text{ GeV}/c^2$  and  $24 \text{ GeV}/c^2$  and greater than  $265 \text{ GeV}/c^2$  with couplings as low as  $1.4 \times 10^{-5} \text{ GeV}^{-2}$ . As the last specific coupling we have the one that can occur with a millicharged particle, these are theoretically well motivated to represent a fraction of the DM. In this case we have obtained leading couplings as low as  $2.1 \times 10^{-10} e$  for masses between  $2.7 \text{ GeV}/c^2$  and  $12 \text{ GeV}/c^2$  using data from the PICO-60 detector. It is important to mention that these results have already been published in the journal "Physical Review D" since August 10, 2022 and represent the strongest limits established for photon-mediated DM interactions in the low-mass WIMP range ( $2.7\text{-}24 \text{ GeV}/c^2$ ) [6].

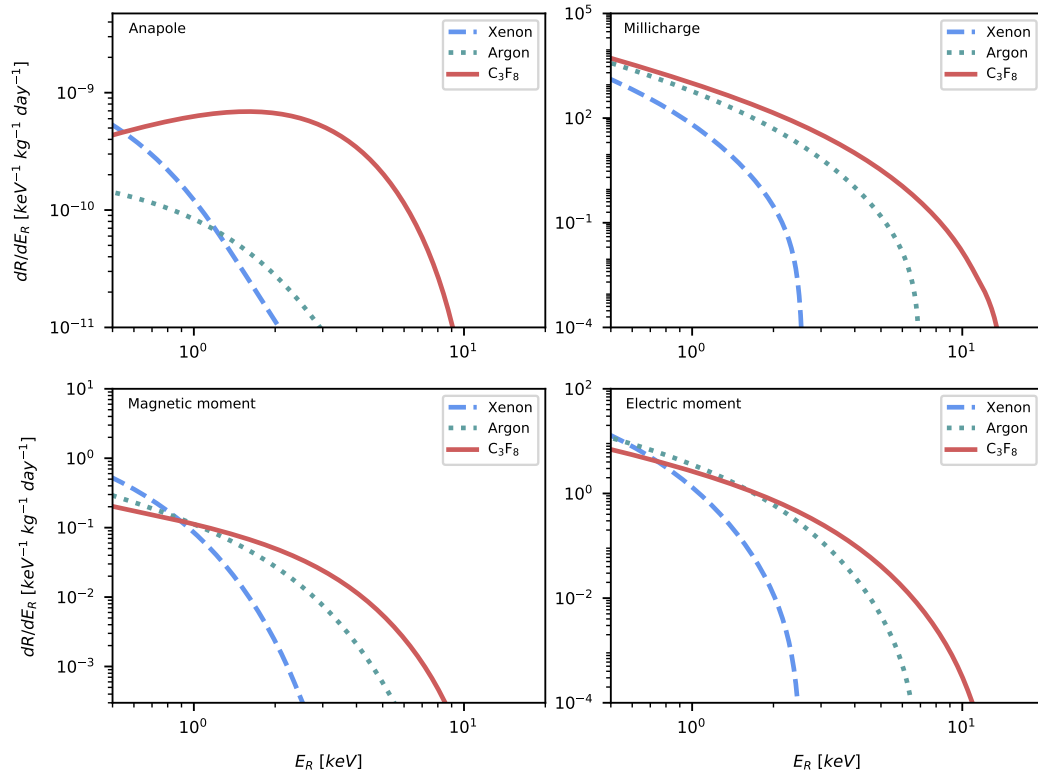


FIGURE 3.10: Scattering rates in  $\text{C}_3\text{F}_8$  (red), xenon (dashed blue), and argon (dotted green) for a DM particle with mass of  $5 \text{ GeV}/c^2$  with coupling through the anapole moment (upper left, for a coupling of  $3.6 \times 10^{-8} \text{ GeV}^{-2}$ ), millicharge (upper right, for a coupling of  $2.2 \times 10^{-8} e$ ), magnetic dipole moment (lower left, for a coupling of  $2.8 \times 10^{-8} \text{ GeV}^{-1}$ ), and electric dipole moment (lower right, for a coupling of  $2.8 \times 10^{-8} \text{ GeV}^{-1}$ ). The rates were obtained with the `WIMpy_NREFT` package [46].

## 3.2 Results on Inelastic dark matter-nucleus interactions from the PICO-60 $\text{C}_3\text{F}_8$ and $\text{CF}_3\text{I}$ bubble chambers

### 3.2.1 Introduction

The search for dark matter (DM) as weakly interacting massive particles (WIMPs) in direct detection experiments has made great progress [5, 24]. It is important to ask what characteristics to expect about the properties of WIMPs once a signal has been established. We do not know the mass of the dark matter particle or other properties such as spin. On the other hand, the possible interactions between WIMPs and Standard Model (SM) particles are also unknown. More light can be shed on these parameters once detection is established.

In direct detection, the aim is to directly observe the recoil induced by DM scattering in the nuclei. The typical Milky Way bound DM velocity is limited by the galactic escape velocity  $v_{esc} \approx 550 \text{ km/s}$  and, consequently, the highest nuclear recoil energy for a terrestrial target assuming WIMPs with a mass of  $100 \text{ GeV}$  is  $\approx 300 \text{ keV}$ . Therefore, direct detection experiments are probing the non-relativistic limit of

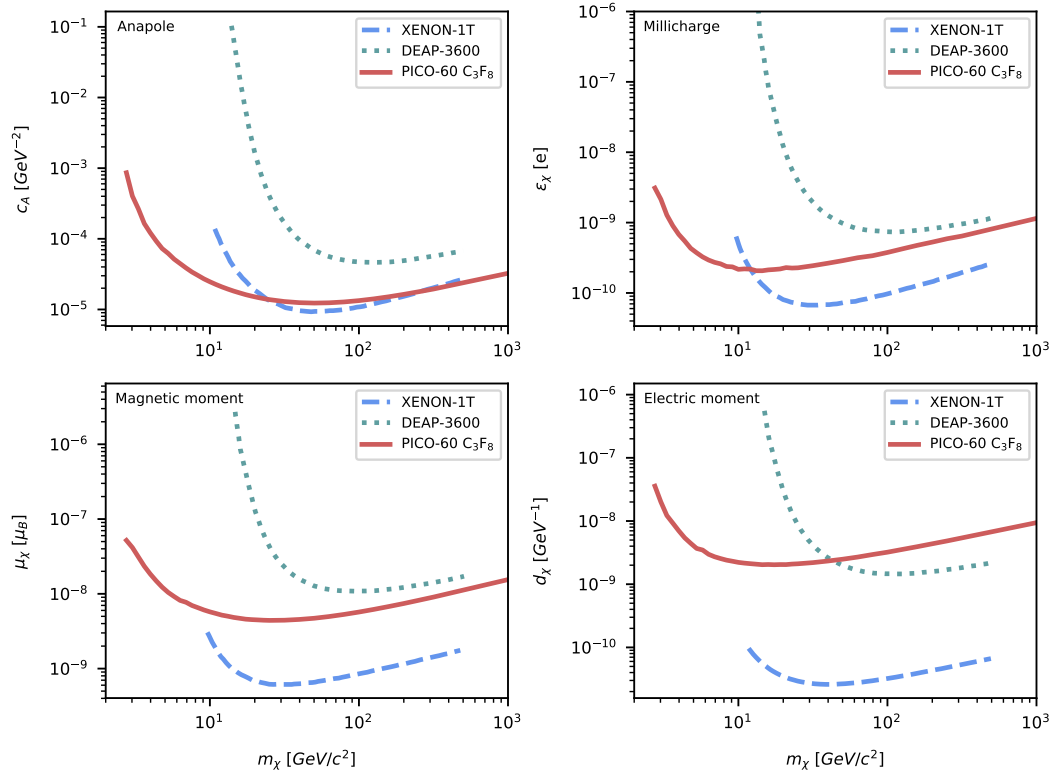


FIGURE 3.11: Exclusion limits at 90% C.L. for the anapole moment (upper left), millicharge (upper right), magnetic dipole moment (lower left), and electric dipole moment (lower right) couplings. The limits are derived from the profile likelihood analysis of the PICO-60  $C_3F_8$  (red) combined blind exposure. Limits from XENON-1T (dashed blue) [21] and DEAP-3600 (dotted green) [2] using xenon and argon, respectively, are also shown.

the interaction between dark matter nuclei and it is possible to describe the scattering process in terms of a non-relativistic effective theory of DM and nucleons. In Section 3.2.1 we present the general operator basis for non-relativistic interactions between DM and nuclei and the formalism for the description of DM scattering in nuclei. Non-relativistic effective field theory can be used for a variety of applications [45, 19].

Different combinations of WIMP mass and WIMP-nucleus interactions can give rise to very similar signals in direct detection experiments. Therefore, large exposures or additional signals are needed to obtain information about the properties of dark matter. Normally, a large exposure is achieved with larger and more sensitive detectors than those available so far, which is very expensive. However, direct detection experiments are sensitive to inelastic WIMP-nucleus scattering in addition to the standard signature of elastic WIMP nucleus scattering [40, 31]. In this process, the nucleus is excited and, due to the different nuclear structure of the ground and the excited state, the response depends crucially on the DM-nucleon interaction. Exploiting the inelastic signal increases the experimental sensitivity to DM properties without the need to modify the detector configuration. This possibility is particularly attractive in the context of direct detection experiments using bubble chambers with superheated targets [9]. The PICO detectors are well suited to the search for

inelastic interactions since using targets with the isotope  $^{127}\text{I}$  they have unusually low output states, with an excitation energy of 57.6 keV. It is well known that inelastic scattering can help distinguish spin-dependent (SD) and spin-independent (SI) interactions traditionally considered in direct detection [27]. In particular, Inelastic (I)DM particles, with O(keV) or larger mass splittings are expected in a variety of dark matter models [41, 16, 13, 17].

A simple inelastic dark matter model consists of a lighter state  $\chi_1$  and a heavier state  $\chi_2$  with a mass splitting  $\delta \equiv M_{\chi_2} - M_{\chi_1}$ . Generally, the lighter state will dominate the relic abundance, and two-by-two scattering processes with baryons should lead to an excitation or de-excitation of the DM state. First, the kinetic energy of dark matter must be large enough to overcome the mass splitting, imposing a lower limit on the relative velocity necessary for an interaction to take place. Second, the minimum momentum exchange required for a collision to occur increases with mass splitting, which means that IDMs with typical halo velocities can only scatter with heavier nuclei and deposit a sufficiently large recoil energy. In other words, even with sufficient kinetic energy, there is a momentum transfer threshold  $\sim \mu_{\chi N} v$  below which no interactions can occur. Consequently, inelastic dark matter can elude searches in most direct detection experiments, either because the analysis region is limited to low recoil energies ( $\lesssim 10 - 50$  keV), or because of the limited mass of the target nucleus. Experiments with bubble-counting heat measurements provide a powerful tool to distinguish DM-induced nuclear recoil (NR) events due to coherent interactions of DM nuclei with high momentum transfer from background events. In addition to nuclear recoil signals from coherent scattering, heavier elements can contribute a second type of signal, thanks to their comparatively less tightly bound outer nucleon shells: gamma photons from induced nuclear excitation and subsequent decay, or the de-excitation of a long-lived excited nuclear state.

The aim of this section is to study the complete set of non-relativistic effective operators instead of only the conventional SD and SI interactions for the case of IDM. We present results for exclusion limits as a function of the delta parameter (mass splitting) at a 90% confidence level using PICO-60 detector data. We have included in our analysis leading experiments in the search for DM with Xenon targets such as XENON-1T and PANDAX-4T.

### Non-relativistic effective field theory

In the subsection 3.1.1, the effective Lagrangian (3.1) was introduced to describe the scattering of the DM with nucleons in the NREFT approach. This treatment results in quantum mechanical operators depending on relative velocity, exchanged momentum, and nucleon and DM spins. In this study we will address the operators  $\mathcal{O}_1 = 1_\chi 1_N$  (with  $1_\chi$  and  $1_N$  as identity operators) and  $\mathcal{O}_4 = \vec{S}_\chi \cdot \vec{S}_N$ , where  $\vec{S}_\chi$  and  $\vec{S}_N$  are the DM and the spin of the nucleus, respectively. These two operators are the classical SI and SD interactions that are considered in direct dark matter detection experiments. It is important to note that the  $\mathcal{O}_4$  operator is particularly significant for inelastic dark matter experiments sensitive to electronic recoils, since for odd mass isotopes low transitions between ground and excited states with different spins can take place [29]. The generalization to "inelastic dark matter" would imply allowing  $\chi_1 \mathcal{O}_\chi \chi_2$ , with  $\chi_1$  and  $\chi_2$  having different masses.

### Kinematics of inelastic dark matter scattering

In models of inelastic DM, the dark sector comprises two states  $\chi_1$  and  $\chi_2$  with a mass splitting  $\delta = M_{\chi_2} - M_{\chi_1}$ . At tree level,  $\chi_2$  couples to  $\chi_1$  via scalar or a gauge boson field, but the self-coupling  $\bar{\chi}_1\chi_1$  or  $\bar{\chi}_2\chi_2$  is loop-suppressed. In the simplest case, we consider the Lagrangian  $\mathcal{L} \supset g\phi\bar{\chi}_2\chi_1 + h.c.$ . Since  $\chi_2$  is heavier than  $\chi_1$ , after freeze-out we expect  $\chi_2$  to be depleted either through decay or through the inter-conversion process  $\chi_2\chi_2 \rightarrow \chi_1\chi_1$  when the temperature of the universe falls below the mass splitting,  $T < \delta$ . As a consequence, the dark matter today is dominated by  $\chi_1$ .

We consider two types of dark matter interactions in the detector. The first is nuclear recoil (NR), where the target nucleus shifts and  $\chi_1$  becomes  $\chi_2$ . In addition,  $\chi_1$  may also interact with the valence nucleons and instigate nuclear excitation (NE) into an unstable state  $N^*$ . As long as the mediator mass  $M_\phi$  is much larger than the momentum transfer  $q$ , the interaction can be described by the effective Lagrangian

$$\mathcal{L} \sim \frac{1}{\Lambda^2} \bar{\chi}_2 \chi_1 \bar{N}^* N, \quad (3.21)$$

where the UV scale  $\Lambda$  is set by the mediator mass and the coupling between the dark sector and the SM. We define the quantity  $\delta$ , which represents the sum of the DM mass splitting  $\delta$  and the excitation energy  $\Delta E \equiv E_{N^*} - E_N$ :

$$\Delta \equiv \delta + \Delta E. \quad (3.22)$$

$\Delta E$  vanishes in NR-only scattering. The kinematics of both interactions follows

$$\frac{\vec{q}_i^2}{2M_{\chi_1}} = \frac{\vec{q}_f^2}{2M_{\chi_2}} + \frac{\vec{q}^2}{2M_N} + \Delta \quad (3.23)$$

where the momentum transfer  $\vec{q} = \vec{q}_f - \vec{q}_i$ . Equation 3.23 can be written as:

$$\frac{q^2}{2\mu_{\chi N}} - qv\cos\theta + \Delta = 0, \quad (3.24)$$

where  $\mu_{\chi N} \equiv M_\chi M_N / (M_\chi + M_N)$  is the reduced mass of the DM-nucleus system, and  $\theta$  is the laboratory frame scattering angle. We also define  $M_\chi \equiv M_{\chi_1} \simeq M_{\chi_2}$  which is valid so long as  $M_\chi \gg \delta$ . We will assume the dark matter velocity  $v$  follows a Maxwellian distribution with  $v_0 = 220$  km/s truncated at the escape velocity  $v_{esc} = 600$  km/s in the Earth's frame, assuming the Earth's velocity is  $v_e = 240$  km/s [54]. The minimum/maximum momentum transfer is obtained at  $|\cos\theta| = 1$  which gives

$$q_{min}/q_{max} = \mu_{\chi N} v \left[ 1 \mp \sqrt{1 - 2\frac{\Delta}{\mu_{\chi N} v^2}} \right], \quad (3.25)$$

and the minimum/maximum recoil energy is simply obtained via the relationship  $E_R = q^2 / (2M_N)$ . The minimum dark matter velocity required to scatter off a nucleus with *any* recoil energy is thus

$$v_{min} = \sqrt{2\frac{\Delta}{\mu_{\chi N}}}. \quad (3.26)$$

Therefore, higher dark matter kinetic energy is required for inelastic scattering as  $\Delta$  increases. Therefore, the maximum mass split that can be probed in an experiment

is

$$\delta_{max} = \frac{1}{2}\mu_{\chi N}(v_e + v_{esc})^2 - \Delta E, \quad (3.27)$$

which grows for larger reduced masses  $\mu_{\chi N}$  and, therefore, heavier target nuclei. For a specific nuclear recoil energy, the minimum dark matter velocity for an interaction to occur can also be obtained from Eq. 3.24:

$$v_{min}(E_R) = \frac{1}{\sqrt{2M_N E_R}} \left( \frac{M_N}{\mu_{\chi N}} E_R + \Delta \right). \quad (3.28)$$

In addition to NR interactions in traditional direct detection experiments, we are also interested in deexcitation gamma quanta in NE scattering:  $\chi_1 + N \rightarrow \chi_2 + N^* \rightarrow \chi_2 + N + \gamma$ . Depending on the IDM model,  $\chi_2$  may also decay to SM or invisible particles. If  $\chi_2$  decays to photon(s) rapidly within the detector, the decay photon could be resolved as an inelastic scattering signature; otherwise,  $\chi_2$  could leave the detector. For both NR and NE, the dispersion rate is given by:

$$R = \sum_i N_{T_i} \frac{\rho_\chi}{M_\chi} \int_{v_{min}}^{v_{max}} dv v f(v) \int_{E_{R,min}}^{E_{R,max}} \frac{d\sigma_{\chi N}}{dE_R} dE_R, \quad (3.29)$$

where  $N_{T_i}$  is the number of the target nuclei of a given isotope in the detector,  $\rho_\chi = 0.3 \text{ GeV cm}^{-3}$  is the local dark matter density, and  $f(v)$  is the one-dimensional Maxwellian velocity distribution. The minimum and maximum recoil energies can be found from Eq. 3.25. The differential cross section is

$$\frac{d\sigma_{\chi N}}{dE_R} = \frac{\sigma_n M_N}{2v^2 \mu_{\chi n}^2} S(E_R), \quad (3.30)$$

where  $\sigma_n$  is the per-nucleon scattering cross section and the nuclear response is encapsulated in  $S(E_R)$ . For NR, this is just the Helm form factor. In the NE case, dark matter only interacts with the few valence nucleons in the surface layer of the nucleus, where the nuclear response depends on momentum transfer without the enhancement factor  $A^2$  in  $S(E_R)$ . As first derived in [28], the nuclear response function is written as

$$S(\vec{q}) = \sum_L |\langle J_f || j_L(qr) Y_{LM}(\hat{r}) || J_i \rangle|^2, \quad (3.31)$$

where the sum runs over all allowed even angular momentum states within the range  $|J_i - J_f| \leq L \leq |J_i + J_f|$ . Here,  $J_i$  and  $J_f$  are respectively the initial and final angular momenta,  $j_L$  are spherical Bessel functions and  $Y_{LM}$  are spherical harmonics. The calculation of the response function is usually quite complicated in the case of heavy nuclei due to the complexity of the valence structure and the deformation of the nucleus. Fortunately, we can use the reduced transition probability at the nuclear transition  $E2$  to approximately eliminate the element of the angular matrix, which is defined as

$$B(E2) = \frac{1}{2J_i + 1} |\langle J_f || er^2 Y_2 || J_i \rangle|^2, \quad (3.32)$$

with  $Y_2$  the spherical tensor operator. Assuming that the nuclear transition probability density has a peak near the surface of the nucleus, we find [30]

$$S(\vec{q}) = \frac{A^2}{Z^2} (2J_i + 1) j_2(qR)^2 \frac{B(E2)}{e^2 R^4}, \quad (3.33)$$



with the nucleus radius  $R \simeq 1.2 \times A^{1/3}$  fm.

In this analysis we have classified the operators into two groups, the spin-independent and the spin-dependent, as we can see in Table 3.3. Our objective is to obtain the behavior of the exclusion limits using the PICO-60 data at a 90% confidence level as a function of the  $\delta$  (mass splitting) parameter for all the operators. As a point of comparison we have calculated the same limits for the leading detectors XENON-1T [15] and PANDAX-4T [52] using the exposure and background values reported by these experiments in their latest results for SI coupling.

TABLE 3.3: NREFT operators, with  $\vec{v}^\perp$  the component of the velocity perpendicular to the momentum transfer,  $i\frac{\vec{q}}{m_N}$  the momentum transfer,  $\vec{S}_\chi$ -DM spin and  $\vec{S}_N$ -nucleon spin.

SD Operators	SI Operators
$\mathcal{O}_3 = i\vec{S}_N \cdot \left( \frac{\vec{q}}{m_N} \times \vec{v}^\perp \right)$	$\mathcal{O}_1 = 1_\chi 1_N$
$\mathcal{O}_4 = \vec{S}_\chi \cdot \vec{S}_N$	$\mathcal{O}_5 = i\vec{S}_\chi \cdot \left( \frac{\vec{q}}{m_N} \times \vec{v}^\perp \right)$
$\mathcal{O}_6 = \left( \vec{S}_\chi \cdot \frac{\vec{q}}{m_N} \right) \left( \vec{S}_N \cdot \frac{\vec{q}}{m_N} \right)$	$\mathcal{O}_8 = \vec{S}_\chi \cdot \vec{v}^\perp$
$\mathcal{O}_7 = \vec{S}_N \cdot \vec{v}^\perp$	$\mathcal{O}_{11} = i\vec{S}_\chi \cdot \frac{\vec{q}}{m_N}$
$\mathcal{O}_9 = i\vec{S}_\chi \cdot \left( \vec{S}_N \cdot \frac{\vec{q}}{m_N} \right)$	
$\mathcal{O}_{10} = i\vec{S}_N \cdot \frac{\vec{q}}{m_N}$	

### Detector efficiencies

One of the most important factors in determining WIMP efficiencies for a given type of coupling in direct search is the detector efficiency curves. These curves are obtained by fitting all the calibration data for each chemical element present in the detector target material. The shape of these curves and the range of energies in which they are defined completely determine the behavior of the exclusion limits. In the case of direct search detectors that use time projection cameras (TPC) as a detection technique (XENON-1T and PANDAX-4T), electronic backtracking plays an important role. In this type of chamber, scintillation light is used as the main signal to discriminate between nuclear or electronic recoils. Therefore, since the efficiency is determined from the scintillation light measured in the PMTs, it is very difficult to have high efficiency values, since depending on where the interaction event occurs, a part of the emitted light can always be lost. On the other hand, detectors such as PICO-60, which are bubble chambers with superheated liquids, have the important advantage of recording events (bubbles) above a certain threshold energy value with nearly 100% efficiency. Figure 3.12 shows the efficiency curves used in our analysis for the XENON-1T, PANDAX-4T and PICO-60 detectors. These efficiency curves were taken from the latest results reported for the XENON-1T [15] and PANDAX-4T [52] detectors for SI coupling.

### 3.2.2 Results for SI and SD couplings

In this subsection we will see the limits for the IDM in the classical SI( $\mathcal{O}_1$ ) and SD( $\mathcal{O}_4$ ) couplings. We will consider for the delta parameter a range between 0 and 600 keV, which is interpreted as a variable  $v_{min}$  in the integration for a fixed WIMP mass. To

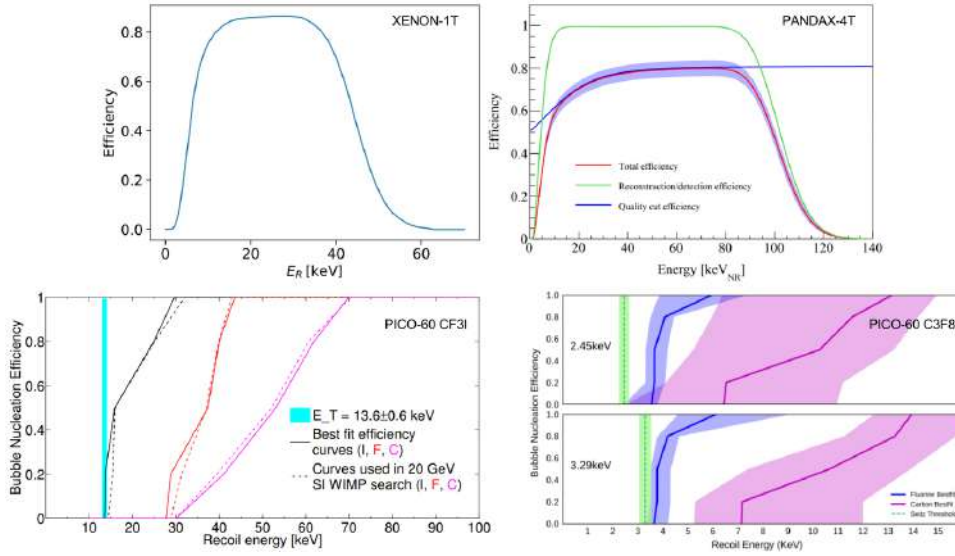


FIGURE 3.12: Nucleation efficiency curves for the detectors considered in this work. Efficiency curves for detectors with Xenon targets XENON-1T (upper left) [15] and PANDAX-4T (upper right) [52]. On the bottom we have the efficiency curves for the PICO-60 detector with  $\text{CF}_3\text{I}$  (left) and  $\text{C}_3\text{F}_8$  (right) targets.

calculate the differential event rate within an NREFT for each operator we will use the python package `WIMpy_NREFT` [46]. The standard halo parametrization is used, with the following parameters: local dark matter density  $\rho_D = 0.3 \text{ GeV}c^{-2}\text{cm}^{-3}$ , galactic escape velocity  $v_{esc} = 544 \text{ km/s}$ , velocity of the earth with respect to the halo  $v_{Earth} = 232 \text{ km/s}$ , and characteristic WIMP velocity with respect the halo  $v_0 = 220 \text{ km/s}$ .

In the case of PICO-60 we used the results of the runs with  $\text{C}_3\text{F}_8$  and  $\text{CF}_3\text{I}$  targets, where it was taken into account that for high DM masses only the data from the  $\text{CF}_3\text{I}$  bubble chamber are significant. The thermodynamic threshold for the  $\text{CF}_3\text{I}$  chamber was 13.6 keV and for the  $\text{C}_3\text{F}_8$  chamber we had two thresholds 2.45 and 3.29 keV, and we used the background levels values reported for these thresholds of 1, 3 and 0 events per year respectively. With these reported background values we calculated the Poisson upper limit for each threshold.

In the case of the Xenon target detectors considered, such as XENON-1T and PANDAX-4T, we took into account that observed events are reported in addition to the background itself due to the electronic recoils. To calculate the upper Poisson limit in this case we use the following expression:

```

Nsig_upper = float(optimize.root(lambda mu: poisson.cdf(Nobs, mu) - 0.1
                                , 5).x) - NBG

```

where “optimize.root” is a function of the python scipy library that is used to find a root of a vector function, “poisson.cdf” is the cumulative distributed function, the value of 0.1 refers to a 90% confidence level, and Nobs and NBG refer to the number of observed and background events respectively. In the case of PANDAX-4T we consider an exposure of 0.63 tonne-year. For XENON-1T an exposure of  $0.475 \times 0.9$  tonnes-year is used, this factor of 0.475 reported by XENON-1T is needed for

searches in the reference region (i.e. where 47.5% of NR events are expected). Table 3.4 shows the values used for the number of events observed and the background level in both experiments.

TABLE 3.4: Number of observed events and background level reported by both experiments in the results for SI coupling [15, 52].

Experiment	Nobs	NBG
XENON-1T	2	1.32
PANDAX-4T	1058	1.1

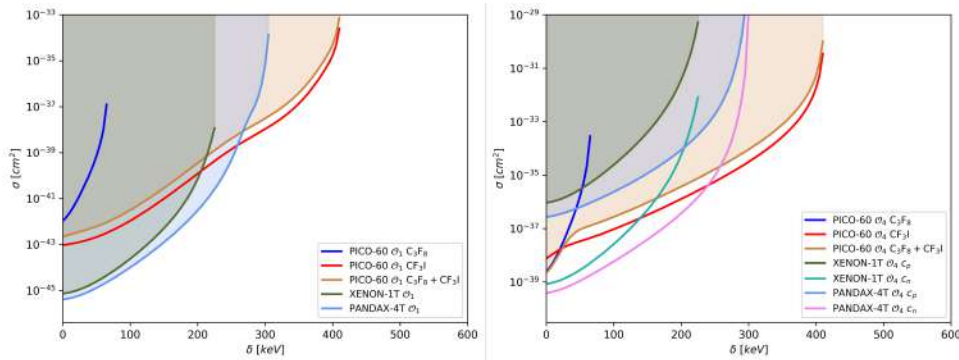


FIGURE 3.13: Exclusion limits as a function of the delta parameter for a WIMP mass of 1TeV on the PICO-60 bubble chamber and the XENON-1T and PANDAX-4T TPCs. Left: 90% limits for SI coupling ( $\mathcal{O}_1$ ), in the case of PICO-60 we show the results for both targets ( $C_3F_8$  and  $CF_3I$ ) separately and combined. Right: Limits at 90% confidence level for SD interaction ( $\mathcal{O}_4$ ), in the case of PICO-60 we only consider coupling with protons and for the Xenon detectors we explore both possibilities.

Figure 3.13 shows the results for WIMP-nucleon SI(left) and SD(right) couplings as a function of the delta parameter for a mass of 1 TeV. In the case of the PICO-60 detector we have considered only WIMP couplings with protons for SD case. For the XENON-1T and PANDAX-4T experiments we have considered both possibilities, couplings with protons or with neutrons, as can be seen in the legend. As we can see considering couplings with protons, PICO-60 sets better limits. In the case of neutron coupling in the experiments using Xenon as target, we have indicated the delta value from which PICO-60 explores a better parameter region. It is important to note that in the case of PICO-60 we show the limits for the  $C_3F_8$  and  $CF_3I$  targets individually as well as the combination of both results. The purpose of this comparison is to elucidate the advantages of using one or another target for future PICO detectors. For SI coupling, which has a direct dependence on the number of target nucleons, we can see that XENON-1T and PANDAX-4T offer better limits. We can also see that thanks to the characteristics of the efficiency curves, the PICO-60 detector explores better the region of high delta parameter, being able to find a value above which it offers better limits than those of detectors using a time projection camera.

As part of our analysis we have decided to analyze the behavior of the sensitivity limits as a function of mass division for masses of 10  $GeV/c^2$ , 100  $GeV/c^2$ , 1  $TeV/c^2$  and 10  $TeV/c^2$  using data from the PICO-60 bubble chambers  $CF_3I$  and  $C_3F_8$ . Figure 3.14 shows the upper limits at 90% C.L. on inelastic DM-nucleon scattering

cross section as a function of the mass splitting  $\delta$  for the  $\mathcal{O}_1$  operator. This cross section is defined at zero transferred momentum, in the elastic ( $\delta = 0$ ) limit. The reported results are compared with important experiments such as XENON-1T [15], PANDAX-4T [53], and CRESST-II [47].

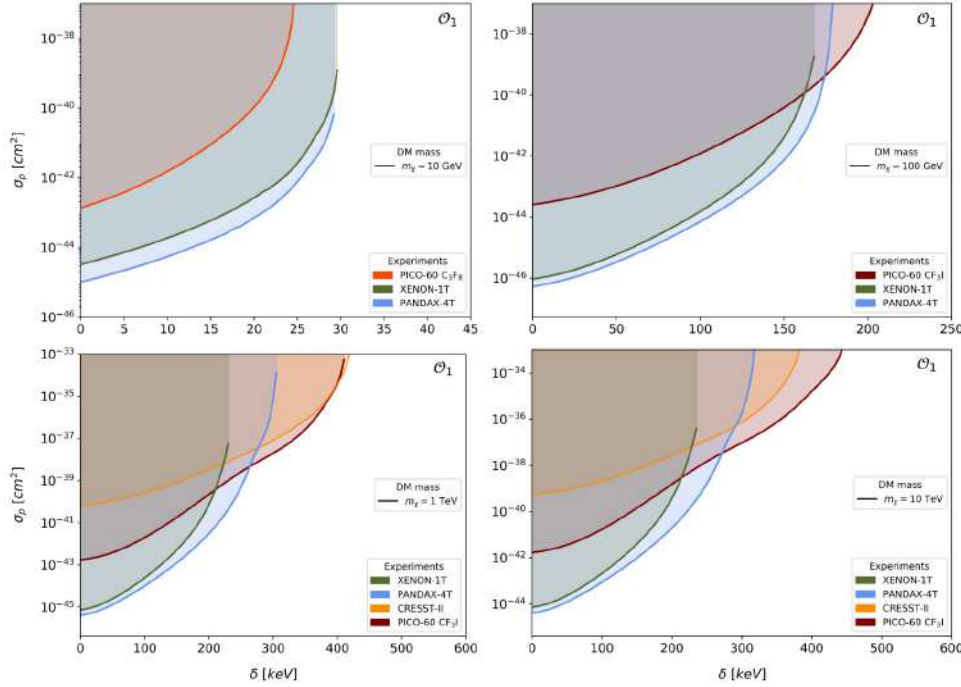


FIGURE 3.14: Upper limits (90% C. L.) on inelastic DM-nucleon scattering cross sections assuming isospin conservation as a function of the mass splitting for the effective operator  $\mathcal{O}_1$  and DM masses of  $10 \text{ GeV}/c^2$ ,  $100 \text{ GeV}/c^2$ ,  $1 \text{ TeV}/c^2$ , and  $10 \text{ TeV}/c^2$ , from the analysis of the PICO-60  $\text{CF}_3\text{I}$  and  $\text{C}_3\text{F}_8$  experiments. Limits from XENON-1T [15], PANDAX-4T [53], and CRESST II [47] are also shown. The limits from XENON-1T and PANDAX-4T were derived using the same methodology, utilizing the available information and data published by the respective collaborations.

We also took the task of comparing our results with the signal reported by DAMA in Figure 3.15. The results of our study using PICO-60 data exclude the possibility that the signal reported by DAMA is due to a dark matter interaction via inelastic scattering for mass splits below 20 keV and above 35 keV [57, 61]. For this comparison with DAMA results we have used data collected in 2001 and 2009, prior to the exclusion of DAMA by XENON-100. However, despite the existence of more recent data, PICO is a suitable experiment to test these results since it uses the same heavy element (iodine) as DAMA. For high mass values of the DM ( $\sim 50 \text{ GeV}/c^2$  and higher), the PICO-60  $\text{CF}_3\text{I}$  data specifically exclude the interpretation of the DAMA signal produced by inelastic scattering in iodine. For mass splittings between 20 and 35 keV, PICO-60 excludes all mass ranges considered, except masses close to  $11 \text{ GeV}/c^2$ , where only small mass splits below 20 keV are excluded. In this case and in general, what happens is that for light masses of the DM (a few  $\text{GeV}/c^2$  up to  $\sim 10 \text{ GeV}/c^2$ ), the contribution of iodine is negligible. due to the little momentum transferred in the interaction. For light DM masses of a few  $\text{GeV}/c^2$ , only lower mass splitting values,  $O(10 \text{ keV})$ , and light nuclei such as carbon and fluorine (PICO)

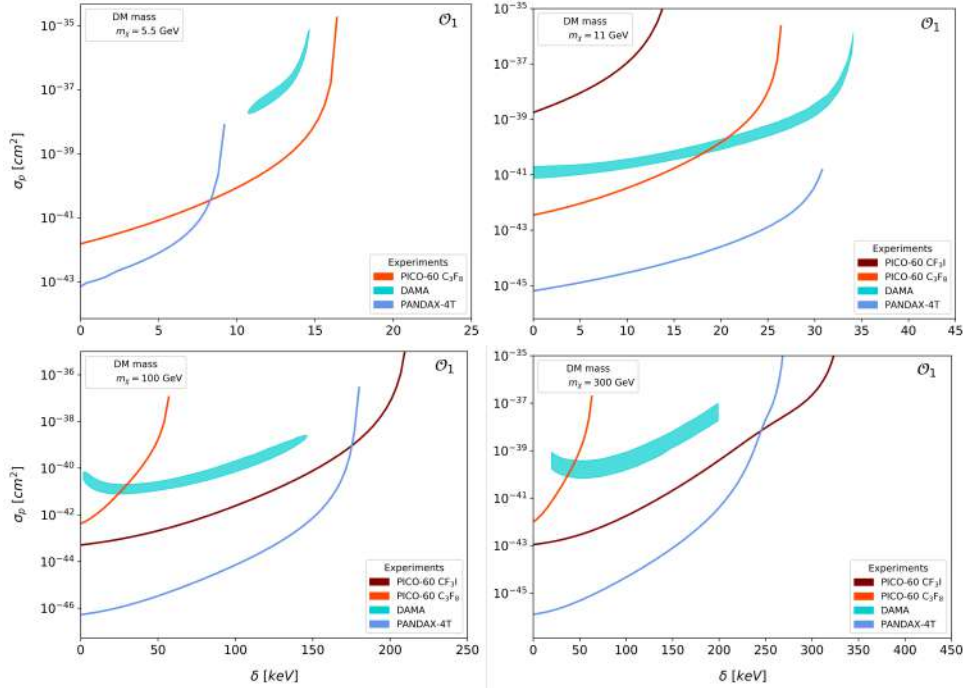


FIGURE 3.15: DAMA allowed regions obtained from [57, 61] and upper bounds of PICO-60 CF<sub>3</sub>I and C<sub>3</sub>F<sub>8</sub> in DM-nucleon scattering cross sections as a function of mass splitting for the effective operator  $\mathcal{O}_1$  and DM masses of 5.5 GeV/c<sup>2</sup>, 11 GeV/c<sup>2</sup>, 100 GeV/c<sup>2</sup> and 300 GeV/c<sup>2</sup> at 99% C. L.

and sodium (DAMA) are possible experimentally, play a decisive role in sensitivity. Although other experiments have excluded these DM mass ranges and mass splittings, PICO is the only experiment that uses iodine. Because PICO and DAMA use a heavy target such as iodine, it is possible to achieve high mass splittings. Bubble chambers, compared to other detection techniques such as scintillation, phonon and ionization detectors (such as DAMA) have a higher sensitivity to inelastic dark matter scattering since they can measure nuclear recoils above the energy threshold and they have the potential to extend to the MeV scale, unlike the limited recoil energy window of other technologies. From these results we can conclude that although inelastic dark matter continues to stimulate significant theoretical development [22, 58, 35, 44], the results obtained from PICO provide evidence that the tension that exists between DAMA and other experiments in the inelastic dark matter model cannot be attributed to the properties of iodine.

We have already seen that the strengths of the PICO-60 bubble chambers lie in the SD couplings, due to the physical properties of the targets used. For this reason, in this study of the inelastic sector, we set ourselves the task of determining the cross section of this dispersion for the operator  $\mathcal{O}_4$ . Figure 3.16 shows the upper limits at 90% C.L. in the inelastic cross section for DM-proton scattering as a function of the mass splitting  $\delta$  for the  $\mathcal{O}_4$  operator. We compare our results with limits derived from results published by XENON-1T [15] and PANDAX-4T [53]. As we can see, the PICO-60 bubble chambers set major limits for all possible values of mass splitting, with a sensitivity of up to 449 keV. For mass splittings below 30 keV PICO-60 C<sub>3</sub>F<sub>8</sub> dominates, however, for higher values PICO-60 CF<sub>3</sub>I prevails.

In Figure 3.17 we have recast the PICO-60 exclusion limits calculated for the  $\mathcal{O}_1$

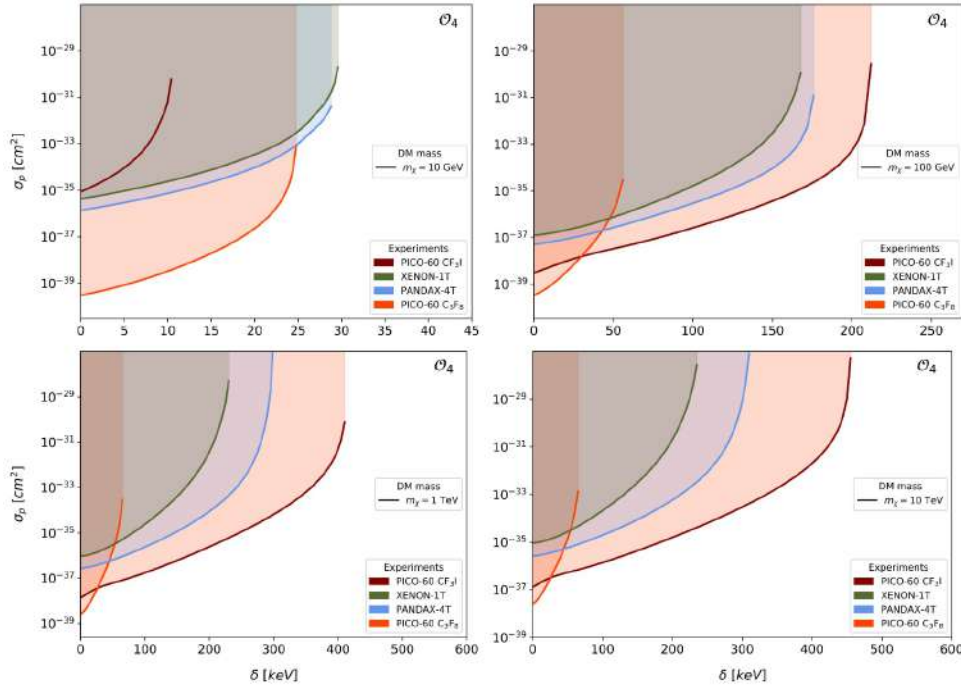


FIGURE 3.16: Upper limits (90% C. L.) on inelastic DM-nucleon scattering cross sections assuming isospin conservation as a function of the mass splitting for the effective operator  $\mathcal{O}_4$  and DM masses of  $10 \text{ GeV}/c^2$ ,  $100 \text{ GeV}/c^2$ ,  $1 \text{ TeV}/c^2$  and  $10 \text{ TeV}/c^2$ , from the analysis of the PICO-60  $\text{CF}_3\text{I}$  and  $\text{C}_3\text{F}_8$  experiments. Limits from XENON-1T and PANDAX-4T are also shown. The limits from XENON-1T and PANDAX-4T were derived using the same methodology, utilizing the available information and data published by the respective collaborations.

and  $\mathcal{O}_4$  operators for the entire range of WIMP masses interesting for direct search experiments as a function of mass splitting. From this graph we can make a better analysis of the behavior of these limits, as well as the importance of the targets used. The unique sensitivity of PICO-60  $\text{CF}_3\text{I}$  to high mass splittings is due to a combination of the heavy nucleus used (iodine) and the ability of this experiment to measure nuclear recoil at all energies above a certain threshold, unlike of experiments that employ noble crystals and semiconductor detectors and therefore have a restricted energy window to measure nuclear recoils. The results indicate a leading sensitivity for classical  $\mathcal{O}_4$  spin-dependent coupling for dark matter masses from a few  $\text{GeV}/c^2$  to a few  $\text{TeV}/c^2$ . These results are of great relevance since this inelastic dispersion is useful to distinguish between spin-dependent or spin-independent interactions [27]. Leading limits for the operator  $\mathcal{O}_1$  are also achieved for mass divisions between 264 keV and 398 keV (DM mass of  $1 \text{ TeV}/c^2$ ), as well as from 272 keV to 445 keV (DM mass of  $10 \text{ TeV}/c^2$ ). These results presented for inelastic dark matter are already published in the journal Physical Review D [1].

### 3.2.3 Excitation limits on large target mass

Now we will see the other possible result of the inelastic WIMP-nucleus interaction, where the heavy nucleus is excited at certain specific values of mass splitting. It is important to note that this effect is only appreciable for heavy elements and that it

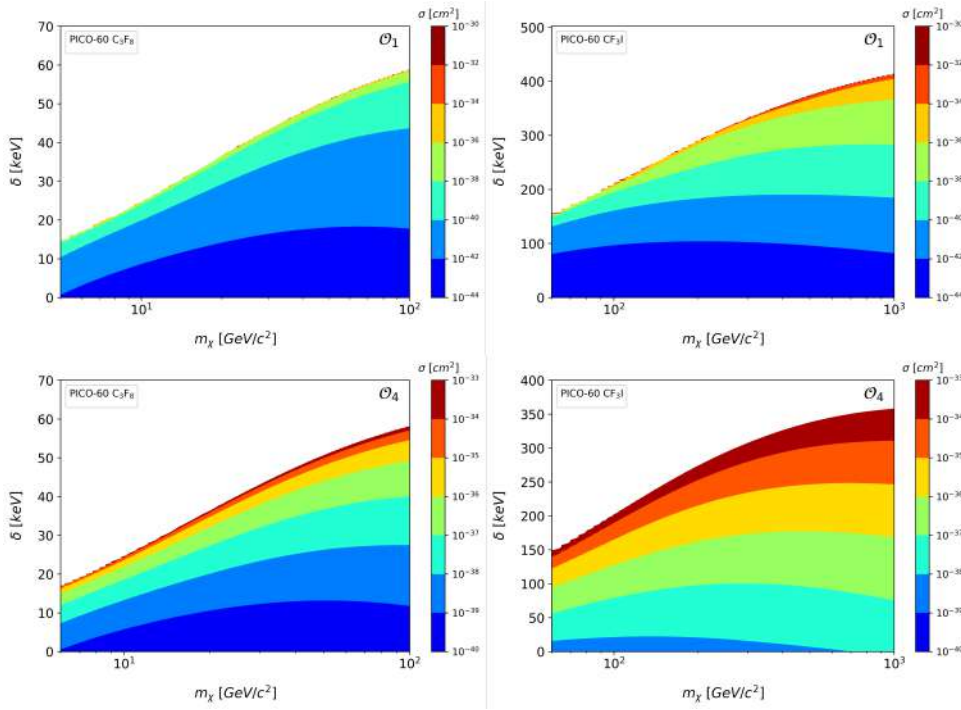


FIGURE 3.17: Upper limits at 90% C.L. obtained from the PICO-60 C3F8 and CF3I experiments on inelastic scattering cross sections of DM-protons and DM-nucleons assuming isospin conservation. The limits are presented as a color scale for the effective operators  $O_1$  (top) and  $O_4$  (bottom) as a function of mass division and mass DM.

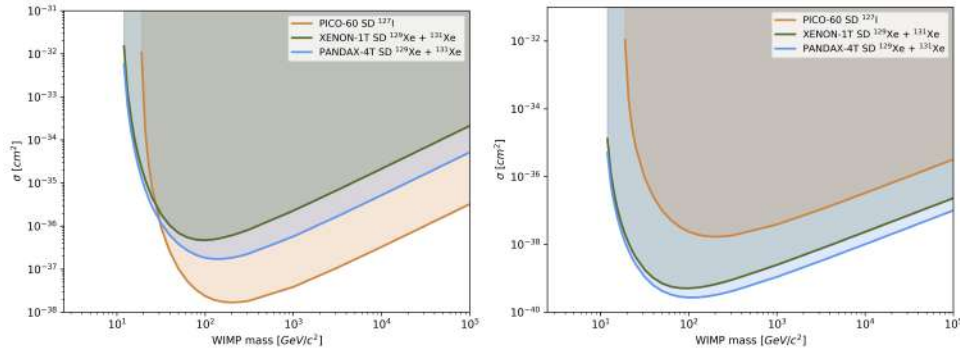


FIGURE 3.18: Exclusion limits with a 90% confidence level considering excitations in the isotopes of  $^{127}\text{I}$ ,  $^{129}\text{Xe}$  and  $^{131}\text{Xe}$  present in the PICO-60, XENON-1T and PANDAX-4T detectors for specific mass splittings of 57.6, 39.6 and 80.2 keV. On the left side we consider couplings with protons and on the right side with neutrons.

only occurs for certain specific values of the delta parameter equal to the excitation energy of each isotope. In our study case only the isotopes of  $^{127}\text{I}$ ,  $^{129}\text{Xe}$  and  $^{131}\text{Xe}$  are relevant, for which the excitation energies are 57.6, 39.6 and 80.2 keV respectively. In Figure 3.18 (left), we have considered couplings with protons, where it can be seen that the PICO-60 detector gives better results for masses higher than 20 GeV.

### 3.2.4 Results for NREFT operators

In this subsection we show the results of our study for the inelastic interaction for all the NREFT operators. In this analysis we have differentiated between spin independent ( $\mathcal{O}_3, \mathcal{O}_5, \mathcal{O}_8, \mathcal{O}_{11}$ ) and spin dependent ( $\mathcal{O}_6, \mathcal{O}_7, \mathcal{O}_9, \mathcal{O}_{10}$ ) operators.

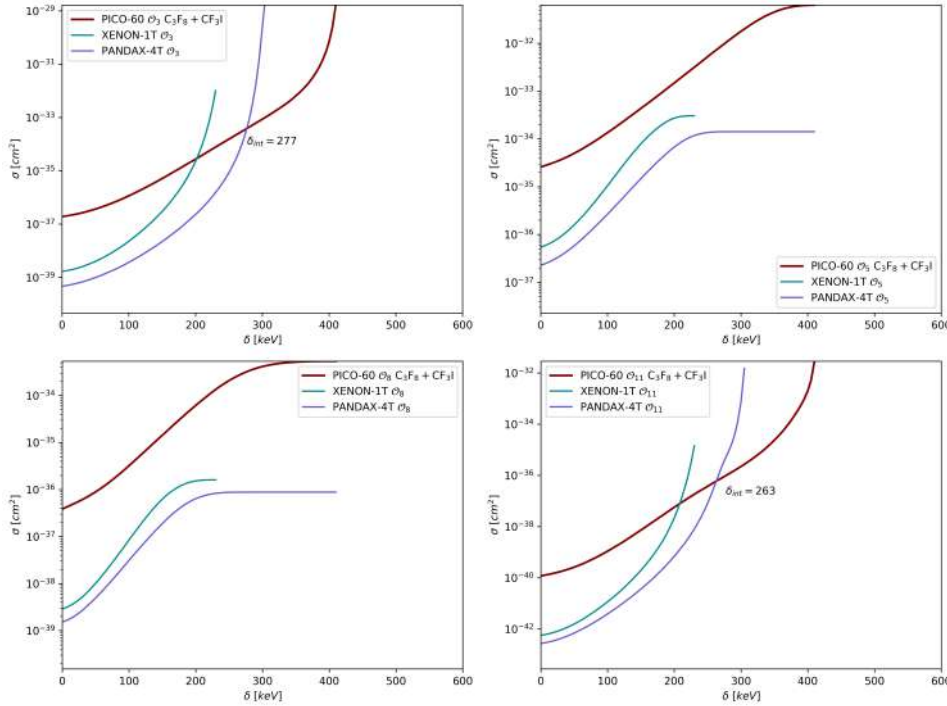


FIGURE 3.19: Exclusion curves behavior at 90% confidence level as a function of the delta parameter for SI operators.

In Figure 3.19 we show the results for the group of operators that behave as spin-independent. In the case of operators  $\mathcal{O}_3$  and  $\mathcal{O}_{11}$  we can see the value of the delta parameter for which PICO-60 gives better results than PANDAX-4T. For operators with SD behavior we show the results in Figure 3.20. In this case we have considered both proton and neutron couplings in the case of the XENON-1T and PANDAX-4T detectors. Once again we see how the PICO-60 detector, using targets with number of unpaired protons in their last shell such as Iodine and Fluorine, can also reach leading limits in this type of inelastic WIMP-nucleon interactions. Overall we have obtained excellent results for all SD operators involved.



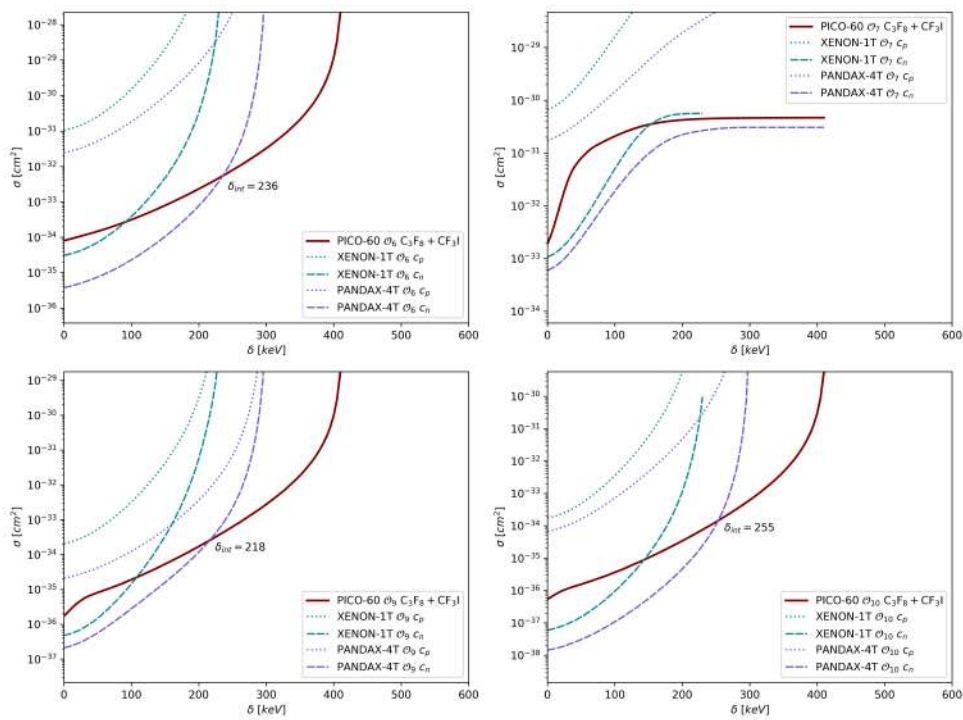


FIGURE 3.20: Exclusion curves at 90% confidence level as a function of the delta parameter for the group of operators behaving as spin-dependent.

## Chapter 4

# Conclusion

In conclusion, in this thesis we have presented the results achieved in the modeling and data analysis using data from the PICO detectors. We have done a complete characterization of the background noise of the PICO500 detector taking into account the main components with respect to its size, composition material and proximity to the target material. To this end we had to model the entire geometry of the detector and its mounting location in SNOLAB using the GEANT4 software. Furthermore, using the latest data collected by the PICO-60 CF3I and PICO-60 C3F8 bubble chambers we have developed an analysis within the framework of a non-relativistic effective theory considering specific photon-mediated couplings between dark matter and nucleons, and also inelastic DM-nucleus interactions. In the case of coupling for photon-mediated DM interactions, leading limits are reported in our work for masses from  $2.7 \text{ GeV}/c^2$  to  $24 \text{ GeV}/c^2$ . The coupling strength of the effective contact interaction operators was performed using a non-relativistic effective field theory. In the low-mass WIMP range ( $2.7\text{-}24 \text{ GeV}/c^2$ ) the reported results are the strongest limits established for photon-mediated DM interactions. For inelastic DM interactions, we have obtained results that establish leading limits on the scattering cross sections between dark matter and nucleons over a wide range of mass divisions and DM masses. These results present the most sensitive search for inelastic dark matter using fluorine and iodine targets. Assuming that the signal reported by DAMA is due to inelastic dark matter interactions, we can exclude several theoretical scenarios with an experiment that, like DAMA, uses iodine. With our results we can conclude that the theoretical scenarios that have been proposed are only allowed in a small DM mass window around  $10 \text{ GeV}/c^2$  and for small mass divisions ( $\sim 10 \text{ keV}$ ). Among some of these scenarios, we have magnetic inelastic dark matter, inelastic scattering that is predominantly coupled to the spin of protons, and proton-philic spin-dependent inelastic dark matter. Our results reaffirm the excellent physical reach of bubble chamber technology using fluorine-iodine objectives.

## Appendix A

# Codes used in the thesis

### A.1 Rate calculators

CODE LISTING A.1: Code for calculating the differential rate for anapole Dark Matter.

```
def dRdE_anapole(E, m_x, c_A, target, vlag=232.0, sigmav=156.0, vesc
=544.0):
    """Return recoil rate for anapole Dark Matter.
    Parameters
    -----
    * 'E' [array]: Recoil energies.
    * 'm_x' [float]: Dark Matter mass in GeV.
    * 'c_A' [float]: Dark Matter anapole moment (in GeV-2).
    * 'target' [string]: Recoil target.
    * 'vlag' [float] (optional): Average lag speed of the lab in km/s.
    Default is 232.
    * 'sigmav' [float] (optional): Velocity dispersion of the DM halo
    in km/s. Default is 156.
    * 'vesc' [float] (optional): Escape speed in the Galactic frame in
    km/s. Default is 544.
    Returns
    -----
    * 'rate' [array like]: Recoil rate in units of events/keV/kg/day.
    """

    #See https://arxiv.org/pdf/1401.4508.pdf

    alpha = 0.007297
    e = np.sqrt(4*np.pi*alpha)
    gp = 5.59
    gn = -3.83

    cn = np.zeros(11)
    cp = np.zeros(11)

    #Operator 8
    cp[7] = -2.0*e*c_A

    #Operator 9
    cp[8] = -gp*c_A
    cn[8] = -gn*c_A

    return dRdE_NREFT(E, m_x, cp, cn, target, vlag, sigmav, vesc)
```

CODE LISTING A.2: Code for calculating the differential rate for millicharged Dark Matter.

```
def dRdE_millicharge(E, m_x, epsilon, target, vlag=232.0, sigmav=156.0,
vesc=544.0):
```

```

"""Return recoil rate for millicharged Dark Matter.
Parameters
-----
* 'E' [array]: Recoil energies.
* 'm_x' [float]: Dark Matter mass in GeV.
* 'epsilon' [float]: Dark Matter charge (in units of the electron
charge).
* 'target' [string]: Recoil target.
* 'vlag' [float] (optional): Average lag speed of the lab in km/s.
Default is 232.
* 'sigmav' [float] (optional): Velocity dispersion of the DM halo
in km/s. Default is 156.
* 'vesc' [float] (optional): Escape speed in the Galactic frame in
km/s. Default is 544.
Returns
-----
* 'rate' [array like]: Recoil rate in units of events/keV/kg/day.
"""
A = Avals[target]

eta = calcEta(vmin(E, A, m_x), vlag=vlag, sigmav=sigmav, vesc=vesc)
amu = 931.5e3 # keV
q1 = np.sqrt(2*A*amu*E)

#Recoil momentum over nucleon mass
qr = q1/amu

# Required for form factors
q2 = q1*(1e-12/1.97e-7)
b = np.sqrt(41.467/(45*A**(-1.0/3.0) - 25*A**(-2.0/3.0)))
y = (q2*b/2)**2

rate = E*0.0

#Calculate the coupling to protons
alpha = 0.007297
e = np.sqrt(4*np.pi*alpha)
m_p = 0.9315

cn = 0
cp = epsilon*e**2

c = [cp + cn, cp - cn]

for tau1 in [0,1]:
    for tau2 in [0,1]:
        c1 = c[tau1]
        c2 = c[tau2]

        R_M = c1*c2*eta/(q1*1e-6)**4
        rate += R_M*np.vectorize(WM.calcwm)(tau1, tau2, y, target)

conv = (rho0/2./np.pi/m_x)*1.69612985e14 #1 GeV^-4*cm^-3*km^-1*s*c
^6*hbar^2 to keV^-1kg^-1day^-1

rate = np.clip(rate, 0, 1e30)
return (4*np.pi/(2*Jvals[target]+1))*rate*conv

```

CODE LISTING A.3: Code for calculating the differential rate for the electric dipole moment.

```

def dRdE_electric(E, m_x, dchi, target, vlag=232.0, sigmav=156.0, vesc
=544.0):

```

```

#Return recoil rate for DM with electric dipole moment.
#dchi: electric dipole moment (in units of e*cm).
A = DMU.Avals[target]

#double eta = calcEta(vmin(E, A, m_x),vlag=vlag, sigmav=sigmav,
vesc=vesc);
#double eta = calcEta_num(vmin(E, A, m_x), vlag, vesc);
eta = DMU.calcEta(DMU.vmin(E, A, m_x),vlag=vlag, sigmav=sigmav,
vesc=vesc)

amu = 931.5e3 # keV
q1 = np.sqrt(2*A*amu*E)

#Recoil momentum over nucleon mass
qr = q1/amu

# Required for form factors
q2 = q1*(1e-12/1.97e-7)
b = np.sqrt(41.467/(45*A**(-1.0/3.0) - 25*A**(-2.0/3.0)))
y = (q2*b/2)**2

rate = E*0.0
rho0 = 0.3 #GeV/cm^3
R_M = 0.0

#Calculate the coupling to protons
alpha = 0.007297
e = np.sqrt(4*np.pi*alpha)
m_p = 0.9315

cn = np.zeros(11)
cp = np.zeros(11)

#cp[10] = 2.0*dchi
cp[10] = 2.0*e*dchi # [GeV^-1]

c_sum = [cp[i] + cn[i] for i in range(11)]
c_diff = [cp[i] - cn[i] for i in range(11)]
c = [c_sum, c_diff]

for tau1 in [0,1]:
    for tau2 in [0,1]:

        c1 = c[tau1]
        c2 = c[tau2]

        R_M = qr**2*eta*c1[10]*c2[10]/(q1*1e-6)**4
        rate += R_M*np.vectorize(WM.calcwm)(tau1, tau2, y, target)

conv = (rho0/2./np.pi/m_x)*1.69612985e14 #1GeV^-4*cm^-3*km^-1*s*
c^6*hbar^2 to keV^-1kg^-1day^-1
rate = np.clip(rate, 0, 1e30)
return (4*np.pi/(2*DMU.Jvals[target]+1))*rate*conv

```

CODE LISTING A.4: Code for calculating the differential rate for the magnetic dipole moment.

```

def dRdE_magnetic(E, m_x, mu_x, target, vlag=232.0, sigmav=156.0, vesc
=544.0):
    """Return recoil rate for magnetic dipole Dark Matter.
    Parameters
    -----

```

```

* 'E' [array]: Recoil energies.
* 'm_x' [float]: Dark Matter mass in GeV.
* 'mu_x' [float]: Dark Matter magnetic dipole (in units of the Bohr
  Magnetron).
* 'target' [string]: Recoil target.
* 'vlag' [float] (optional): Average lag speed of the lab in km/s.
  Default is 232.
* 'sigmav' [float] (optional): Velocity dispersion of the DM halo
  in km/s. Default is 156.
* 'vesc' [float] (optional): Escape speed in the Galactic frame in
  km/s. Default is 544.
Returns
-----
* 'rate' [array like]: Recoil rate in units of events/keV/kg/day.
  """
A = Avals[target]

#See Eq. 62 of https://arxiv.org/pdf/1307.5955.pdf, but note
#that we're using some different normalisations for the operators
#so there are some extra factors of m_x and m_p lurking around...

amu = 931.5e3 # keV
q1 = np.sqrt(2*A*amu*E) #Recoil momentum in keV

alpha = 0.007297
e = np.sqrt(4*np.pi*alpha)
m_p = 0.9315

#Proton and neutron g-factors
gp = 5.59
gn = -3.83

#Bohr Magnetron
#Tesla = 194.6*eV**2 # Tesla in natural units (with e =
  sqrt(4 pi alpha))
#muB = 5.7883818e-5*eV/Tesla # Bohr magneton
mu_B = 297.45 #GeV^-1 (in natural units (with e = sqrt(4 pi alpha))
)

cp = [E*0.0 for i in range(11)]
cn = [E*0.0 for i in range(11)]

#Operator 1
cp[0] = e*(mu_x*mu_B)/(2.0*m_x)

#Operator 5
cp[4] = 2*e*(mu_x*mu_B)*m_p/(q1*1e-6)**2

#Operator 4
cp[3] = gp*e*(mu_x*mu_B)/m_p
cn[3] = gn*e*(mu_x*mu_B)/m_p

#Operator 6
cp[5] = -gp*e*(mu_x*mu_B)*m_p/(q1*1e-6)**2
cn[5] = -gn*e*(mu_x*mu_B)*m_p/(q1*1e-6)**2

return dRdE_NREFT(E, m_x, cp, cn, target, vlag, sigmav, vesc)

```

## A.2 Other relevant codes

CODE LISTING A.5: Code for drawing exclusion limits in Python language.

```

threshold1 = 3.29
threshold2 = 2.45

Er = np.arange(0.1,130.2,0.1) # array of recoil energies
    (0.01,500.01,0.01)
#####LF Tensors#####
LF=np.ones((42,40,40,2,3))

if int_type == 'SI':
    LFSI = np.load('LF_NewSI.npy')
    LF[:, :, :, 0, 0] = LFSI[:, :, :, 0, 0]
    LF[:, :, :, 0, 1] = LFSI[:, :, :, 0, 1]
    LF[:, :, :, 0, 2] = LFSI[:, :, :, 0, 2]
    index_coupling = 0
if int_type == 'Millicharge':
    LFMillicharge = np.load('LF_NewMillicharge.npy')
    LF[:, :, :, 0, 0] = LFMillicharge[:, :, :, 0, 0]
    LF[:, :, :, 0, 1] = LFMillicharge[:, :, :, 0, 1]
    LF[:, :, :, 0, 2] = LFMillicharge[:, :, :, 0, 2]
    index_coupling = 0
if int_type == 'Magnetic':
    LFMagnetic = np.load('LF_NewMagnetic.npy')
    LF[:, :, :, 0, 0] = LFMagnetic[:, :, :, 0, 0]
    LF[:, :, :, 0, 1] = LFMagnetic[:, :, :, 0, 1]
    LF[:, :, :, 0, 2] = LFMagnetic[:, :, :, 0, 2]
    index_coupling = 0
if int_type == 'Electric':
    LFElectric = np.load('LF_NewElectric.npy')
    LF[:, :, :, 0, 0] = LFElectric[:, :, :, 0, 0]
    LF[:, :, :, 0, 1] = LFElectric[:, :, :, 0, 1]
    LF[:, :, :, 0, 2] = LFElectric[:, :, :, 0, 2]
    index_coupling = 0
if int_type == 'Anapole':
    LFAnapole = np.load('LF_NewAnapole.npy')
    LF[:, :, :, 1, 0] = LFAnapole[:, :, :, 0, 0]*0.81
    LF[:, :, :, 1, 1] = LFAnapole[:, :, :, 0, 1]*0.81
    LF[:, :, :, 1, 2] = LFAnapole[:, :, :, 0, 2]
    index_coupling = 1
if int_type == 'SD':
    LFSD = np.load('LF_NewSD.npy')
    LF[:, :, :, 1, 0] = LFSD[:, :, :, 0, 0]*0.81
    LF[:, :, :, 1, 1] = LFSD[:, :, :, 0, 1]*0.81
    LF[:, :, :, 1, 2] = LFSD[:, :, :, 0, 2]
    index_coupling = 1

fig, (ax) = plt.subplots(1, 1, figsize=(8,6))
ax.loglog(masaPICOAna, crossPICOAna, linewidth=3, label="[$GeV^{-2}$]:
    anapole moment")
ax.loglog(masaPICOmagnetic, crossPICOmagnetic, linewidth=3, label="[$\
    \mu_{B}$]: magnetic dipole moment")
ax.loglog(masaPICOelectric, crossPICOelectric, linewidth=3, label="[$e\
    \cdot cm$]: electric dipole moment")
ax.loglog(masaPICOmilli, crossPICOmilli, linewidth=3, label="[$e$]:
    fractional electric charge")
ax.set_xlabel('$m_{\chi}$ [GeV/c^2]', size=10, labelpad=10)
ax.set_ylabel('Coupling strength', size=10, labelpad=10)
plt.show()

```

CODE LISTING A.6: Part of the code used to calculate the differential rates for each specific coupling studied for each mass value considered.

```

from WIMpy import DMUtils as DMU
#####couplings#####
def coupling_ana(sigma,m_x):
    return np.sqrt(np.array(sigma)*np.pi)/(1.97e-14*DMU.reduced_m(1.0, np
    .array(m_x)))

def coupling_mag(sigma,m_x):
    return np.sqrt(np.array(sigma)*np.pi)/(1.97e-14)

def coupling_elec(sigma,m_x):
    return np.sqrt(np.array(sigma)*np.pi)/(1.97e-14)

def coupling_milli(sigma,m_x):
    return np.sqrt(np.array(sigma)*np.pi)*DMU.reduced_m(1.0, np.array(m_x
    ))/(1.97e-14)
#####
for l in range(len(mass_array)):
    mass_index = l
    mass = mass_array[mass_index]

    c_A = coupling_ana(1e-43, mass)          #seeds for anapole
coupling
    eps = coupling_milli(1e-43, mass)        #seeds for
millicharge coupling
    mu_x = coupling_mag(1e-43, mass)         #seeds for magnetic
coupling
    d_x = coupling_elec(1e-43, mass)        #seeds for electric
coupling

    anapole_difftrate_f[l,:] = dRdE_electric(Er, mass, c_A, "
Fluorine")
    anapole_difftrate_c[l,:] = dRdE_electric(Er, mass, c_A, "C12")
    millicharge_difftrate_f[l,:] = dRdE_electric(Er, mass, eps, "
Fluorine")
    millichargee_difftrate_c[l,:] = dRdE_electric(Er, mass, eps, "
C12")
    magnetic_difftrate_f[l,:] = dRdE_electric(Er, mass, mu_x, "
Fluorine")
    magnetic_difftrate_c[l,:] = dRdE_electric(Er, mass, mu_x, "C12")
    electric_difftrate_f[l,:] = dRdE_electric(Er, mass, d_x, "
Fluorine")
    electric_difftrate_c[l,:] = dRdE_electric(Er, mass, d_x, "C12")

```

CODE LISTING A.7: Part of the code where the likelihood surfaces stored in the LF tensor are fitted by convolution with two-dimensional Gaussians that take into account the uncertainties in the thermodynamic thresholds.

```

if int_type == 'SI' or int_type == 'Millicharge' or int_type == '
Magnetic' or int_type == 'Electric':
    SI_rateF_2_4keV_bf = 0.1*np.dot(bf_eff24f,SI_difftrate_f_dmdd)
    SI_rateF_2_4keV_pes = 0.1*np.dot(pes_eff24f,SI_difftrate_f_dmdd)
    SI_rateC_2_4keV_bf = 0.1*np.dot(bf_eff24c,SI_difftrate_c)
    SI_rateC_2_4keV_pes = 0.1*np.dot(pes_eff24c,SI_difftrate_c)
    SI_rate_2_4keV_pes = SI_rateF_2_4keV_pes*152/188+
SI_rateC_2_4keV_pes*36/188
    SI_rate_2_4keV_bf = SI_rateF_2_4keV_bf*152/188+SI_rateC_2_4keV_bf
*36/188
    ratio_p2bf_24 = SI_rate_2_4keV_pes/SI_rate_2_4keV_bf

```



```

diff_p2bf_24 = -math.log(ratio_p2bf_24)

SI_rateF_3_3keV_bf = 0.1*np.dot(bf_eff33f,SI_difftrate_f_dmdd)
SI_rateF_3_3keV_pes = 0.1*np.dot(pes_eff33f,SI_difftrate_f_dmdd)
SI_rateC_3_3keV_bf = 0.1*np.dot(bf_eff33c,SI_difftrate_c)
SI_rateC_3_3keV_pes = 0.1*np.dot(pes_eff33c,SI_difftrate_c)
SI_rate_3_3keV_pes = SI_rateF_3_3keV_pes*152/188+
SI_rateC_3_3keV_pes*36/188
SI_rate_3_3keV_bf = SI_rateF_3_3keV_bf*152/188+SI_rateC_3_3keV_bf
*36/188
ratio_p2bf_33 = SI_rate_3_3keV_pes/SI_rate_3_3keV_bf
diff_p2bf_33 = -math.log(ratio_p2bf_33)
#create 2D gaussian
logbin_sizex_si = abs(np.min(np.diff(map(math.log,LF[mass_index
, :,0,0,0]))))
logbin_sizey_si = abs(np.min(np.diff(map(math.log,LF[mass_index
,0, :,0,1]))))
sigx_si=diff_p2bf_24/logbin_sizex_si
sigy_si=diff_p2bf_33/logbin_sizey_si
g2d_si=np.zeros((int(math.ceil(3*sigx_si))*2+1,int(math.ceil(3*
sigy_si))*2+1))
meanx_si=(g2d_si.shape[0]+1)/2
meany_si=(g2d_si.shape[1]+1)/2
for i in range(1,g2d_si.shape[0]+1):
    for j in range(1,g2d_si.shape[1]+1):
        exponent = ((i-meanx_si)**2)/(2*sigx_si**2) + ((j-
meany_si)**2)/(2*sigy_si**2)
        amplitude = 1/(sigx_si*sigy_si*2*np.pi)
        g2d_si[i-1,j-1] = amplitude*math.exp(-exponent)

g2d_si=g2d_si/g2d_si.T.ravel().sum() #renormalization necessary
because of discrete sampling.

tempLF = np.squeeze(LF[mass_index, :, :,0,2]) + np.min(LF[mass_index
, :, :,0,2])*(-1)
convLFsi = convolve2d(tempLF,g2d_si, mode='same')
(SI_max1l,SI_maxindex) = np.amax(convLFsi),np.argmax(convLFsi.
flatten('F'))
(SI_maxindex_24,SI_maxindex_32) = np.unravel_index(SI_maxindex,[
numsen1,numsen2], 'F')
SI_maxindex_24_v[1]=SI_maxindex_24
SI_maxindex_32_v[1]=SI_maxindex_32
SI_rate_C3F8_2_4keV_dmdd_best=LF[mass_index,SI_maxindex_24,
SI_maxindex_32,0,0]
SI_rate_C3F8_3_29keV_dmdd_best=LF[mass_index,SI_maxindex_24,
SI_maxindex_32,0,1]

```

CODE LISTING A.8: Part of the code where the exclusion limits are calculated at 90% confidence for both thresholds and each mass value from the values stored in the LF tensor. It is important to note that these are the expressions for the Anapolar case. Relevant expressions are used for the other couplings.

```

for aa in range(numsen1):
    for bb in range(numsen2):
        Anapole_rate_C3F8_2_4keV_ = LF[mass_index,aa,bb,1,0]
        Anapole_rate_C3F8_3_29keV_ = LF[mass_index,aa,bb,1,1]

        #limits for 0 events
        pico60_limit_2_4keV_Anapole[1,aa,bb] = coupling_ana(ProbTable
[0]*2.3/
                                (Anapole_rate_C3F8_2_4keV_*exposure2)*1e
-43, mass)

```

---

```
        pico60_limit_3_29keV_Anapole[l,aa,bb] = coupling_ana(  
ProbTable[0]*2.3/  
        (Anapole_rate_C3F8_3_29keV_*exposure1)*1  
e-43, mass)
```

# Bibliography

- [1] E. Adams, B. Ali, I. J. Arnquist, D. Baxter, E. Behnke, M. Bressler, B. Broerman, C. J. Chen, K. Clark, J. I. Collar, P. S. Cooper, C. Cripe, M. Crisler, C. E. Dahl, M. Das, S. Fallows, J. Farine, R. Filgas, A. García-Viltres, G. Giroux, O. Harris, T. Hillier, E. W. Hoppe, C. M. Jackson, M. Jin, C. B. Krauss, V. Kumar, M. Laurin, I. Lawson, A. Leblanc, H. Leng, I. Levine, C. Licciardi, W. H. Lippincott, P. Mitra, V. Monette, C. Moore, R. Neilson, A. J. Noble, H. Nozard, S. Pal, M.-C. Piro, A. Plante, S. Priya, C. Rethmeier, A. E. Robinson, J. Savoie, A. Sonnenschein, N. Starinskitekl, familyi=v., given=I., giveni=I., „ D. Tiwari, E. Vázquez-Jáuregui, U. Wichoski, V. Zacek, and J. Zhang. “Search for inelastic dark matter-nucleus scattering with the PICO-60 CF<sub>3</sub>I and C<sub>3</sub>F<sub>8</sub> bubble chambers”. In: *Phys. Rev. D* 108 (6 2023), p. 062003. DOI: [10.1103/PhysRevD.108.062003](https://doi.org/10.1103/PhysRevD.108.062003). URL: <https://link.aps.org/doi/10.1103/PhysRevD.108.062003>.
- [2] P. Adhikari et al. “Constraints on dark matter-nucleon effective couplings in the presence of kinematically distinct halo substructures using the DEAP-3600 detector”. In: *Phys. Rev. D* 102 (8 2020), p. 082001. DOI: [10.1103/PhysRevD.102.082001](https://doi.org/10.1103/PhysRevD.102.082001). URL: <https://link.aps.org/doi/10.1103/PhysRevD.102.082001>.
- [3] S. Agostinelli et al. “GEANT4—a simulation toolkit”. In: *Nucl. Instrum. Meth. A* 506 (2003), pp. 250–303. DOI: [10.1016/S0168-9002\(03\)01368-8](https://doi.org/10.1016/S0168-9002(03)01368-8).
- [4] B. Aharmim et al. “Measurement of the Cosmic Ray and Neutrino-Induced Muon Flux at the Sudbury Neutrino Observatory”. In: *Phys. Rev. D* 80 (2009), p. 012001. DOI: [10.1103/PhysRevD.80.012001](https://doi.org/10.1103/PhysRevD.80.012001). arXiv: 0902.2776 [hep-ex].
- [5] D. S. Akerib et al. “Results from a Search for Dark Matter in the Complete LUX Exposure”. In: *Physical Review Letters* 118.2 (2017). DOI: [10.1103/physrevlett.118.021303](https://doi.org/10.1103/physrevlett.118.021303). URL: <https://doi.org/10.1103/physrevlett.118.021303>.
- [6] B. Ali, I. J. Arnquist, D. Baxter, E. Behnke, M. Bressler, B. Broerman, C. J. Chen, K. Clark, J. I. Collar, P. S. Cooper, C. Cripe, M. Crisler, C. E. Dahl, M. Das, D. Durnford, S. Fallows, J. Farine, R. Filgas, A. García-Viltres, G. Giroux, O. Harris, T. Hillier, E. W. Hoppe, C. M. Jackson, M. Jin, C. B. Krauss, V. Kumar, M. Laurin, I. Lawson, A. Leblanc, H. Leng, I. Levine, C. Licciardi, S. Linden, P. Mitra, V. Monette, C. Moore, R. Neilson, A. J. Noble, H. Nozard, S. Pal, M.-C. Piro, A. Plante, S. Priya, C. Rethmeier, A. E. Robinson, J. Savoie, A. Sonnenschein, N. Starinskitekl, familyi=v., given=I., giveni=I., „ D. Tiwari, E. Vázquez-Jáuregui, U. Wichoski, V. Zacek, and J. Zhang. “Results on photon-mediated dark-matter–nucleus interactions from the PICO-60 C<sub>3</sub>F<sub>8</sub> bubble chamber”. In: *Phys. Rev. D* 106 (4 2022), p. 042004. DOI: [10.1103/PhysRevD.106.042004](https://doi.org/10.1103/PhysRevD.106.042004). URL: <https://link.aps.org/doi/10.1103/PhysRevD.106.042004>.
- [7] B. Ali et al. “Determining the bubble nucleation efficiency of low-energy nuclear recoils in superheated C<sub>3</sub>F<sub>8</sub> dark matter detectors”. In: *Phys. Rev. D* 106 (12 2022), p. 122003. DOI: [10.1103/PhysRevD.106.122003](https://doi.org/10.1103/PhysRevD.106.122003). URL: <https://link.aps.org/doi/10.1103/PhysRevD.106.122003>.

- [8] C. Amole et al. “Dark matter search results from the complete exposure of the PICO-60 C<sub>3</sub>F<sub>8</sub> bubble chamber”. In: *Phys. Rev. D* 100 (2 2019), p. 022001. DOI: [10.1103/PhysRevD.100.022001](https://doi.org/10.1103/PhysRevD.100.022001). URL: <https://link.aps.org/doi/10.1103/PhysRevD.100.022001>.
- [9] C. Amole et al. “Dark Matter Search Results from the Complete Exposure of the PICO-60 C<sub>3</sub>F<sub>8</sub> Bubble Chamber”. In: *Phys. Rev. D* 100.2 (2019), p. 022001. DOI: [10.1103/PhysRevD.100.022001](https://doi.org/10.1103/PhysRevD.100.022001). arXiv: [1902.04031](https://arxiv.org/abs/1902.04031) [astro-ph.CO].
- [10] C. Amole et al. “Dark Matter Search Results from the PICO–60 C<sub>3</sub>F<sub>8</sub> Bubble Chamber”. In: *Phys. Rev. Lett.* 118 (25 2017), p. 251301. DOI: [10.1103/PhysRevLett.118.251301](https://doi.org/10.1103/PhysRevLett.118.251301). URL: <https://link.aps.org/doi/10.1103/PhysRevLett.118.251301>.
- [11] C. Amole et al. “Dark matter search results from the PICO-60 CF<sub>3</sub>I bubble chamber”. In: *Phys. Rev. D* 93 (5 2016), p. 052014. DOI: [10.1103/PhysRevD.93.052014](https://doi.org/10.1103/PhysRevD.93.052014). URL: <https://link.aps.org/doi/10.1103/PhysRevD.93.052014>.
- [12] C. Amole et al. “Data-driven modeling of electron recoil nucleation in PICO C<sub>3</sub>F<sub>8</sub> bubble chambers”. In: *Phys. Rev. D* 100 (8 2019), p. 082006. DOI: [10.1103/PhysRevD.100.082006](https://doi.org/10.1103/PhysRevD.100.082006). URL: <https://link.aps.org/doi/10.1103/PhysRevD.100.082006>.
- [13] Haipeng An, P. S. Bhupal Dev, Yi Cai, and R. N. Mohapatra. “Sneutrino Dark Matter in Gauged Inverse Seesaw Models for Neutrinos”. In: *Phys. Rev. Lett.* 108 (2012), p. 081806. DOI: [10.1103/PhysRevLett.108.081806](https://doi.org/10.1103/PhysRevLett.108.081806). arXiv: [1110.1366](https://arxiv.org/abs/1110.1366) [hep-ph].
- [14] Nikhil Anand, A. Liam Fitzpatrick, and W. C. Haxton. “Weakly interacting massive particle-nucleus elastic scattering response”. In: *Phys. Rev. C* 89.6 (2014), p. 065501. DOI: [10.1103/PhysRevC.89.065501](https://doi.org/10.1103/PhysRevC.89.065501). arXiv: [1308.6288](https://arxiv.org/abs/1308.6288) [hep-ph].
- [15] E. Aprile et al. “Dark Matter Search Results from a One Ton-Year Exposure of XENON1T”. In: *Phys. Rev. Lett.* 121.11 (2018), p. 111302. DOI: [10.1103/PhysRevLett.121.111302](https://doi.org/10.1103/PhysRevLett.121.111302). arXiv: [1805.12562](https://arxiv.org/abs/1805.12562) [astro-ph.CO].
- [16] Chiara Arina and Nicolao Fornengo. “Sneutrino cold dark matter, a new analysis: Relic abundance and detection rates”. In: *JHEP* 11 (2007), p. 029. DOI: [10.1088/1126-6708/2007/11/029](https://doi.org/10.1088/1126-6708/2007/11/029). arXiv: [0709.4477](https://arxiv.org/abs/0709.4477) [hep-ph].
- [17] G. Barello, Spencer Chang, and Christopher A. Newby. “A Model Independent Approach to Inelastic Dark Matter Scattering”. In: *Phys. Rev. D* 90.9 (2014), p. 094027. DOI: [10.1103/PhysRevD.90.094027](https://doi.org/10.1103/PhysRevD.90.094027). arXiv: [1409.0536](https://arxiv.org/abs/1409.0536) [hep-ph].
- [18] E. Behnke et al. “Direct measurement of the bubble-nucleation energy threshold in a CF<sub>3</sub>I bubble chamber”. In: *Phys. Rev. D* 88 (2 2013), p. 021101. DOI: [10.1103/PhysRevD.88.021101](https://doi.org/10.1103/PhysRevD.88.021101). URL: <https://link.aps.org/doi/10.1103/PhysRevD.88.021101>.
- [19] Kimberly Boddy and Vera Gluscevic. “First Cosmological Constraint on the Effective Theory of Dark Matter-Proton Interactions”. In: *Physical Review D* 98 (Jan. 2018). DOI: [10.1103/PhysRevD.98.083510](https://doi.org/10.1103/PhysRevD.98.083510).
- [20] Jatan Buch, JiJi Fan, and John Shing Chau Leung. “Implications of the Gaia Sausage for Dark Matter Nuclear Interactions”. In: *Phys. Rev. D* 101.6 (2020), p. 063026. DOI: [10.1103/PhysRevD.101.063026](https://doi.org/10.1103/PhysRevD.101.063026). arXiv: [1910.06356](https://arxiv.org/abs/1910.06356) [hep-ph].

- [21] Jatan Buch, JiJi Fan, and John Shing Chau Leung. "Implications of the Gaia sausage for dark matter nuclear interactions". In: *Phys. Rev. D* 101 (6 2020), p. 063026. DOI: [10.1103/PhysRevD.101.063026](https://doi.org/10.1103/PhysRevD.101.063026). URL: <https://link.aps.org/doi/10.1103/PhysRevD.101.063026>.
- [22] Spencer Chang, Graham D. Kribs, David Tucker-Smith, and Neal Weiner. "Inelastic dark matter in light of DAMA/LIBRA". In: *Phys. Rev. D* 79 (4 2009), p. 043513. DOI: [10.1103/PhysRevD.79.043513](https://doi.org/10.1103/PhysRevD.79.043513). URL: <https://link.aps.org/doi/10.1103/PhysRevD.79.043513>.
- [23] James M. Cline, Zuowei Liu, and Wei Xue. "Millicharged Atomic Dark Matter". In: *Phys. Rev. D* 85 (2012), p. 101302. DOI: [10.1103/PhysRevD.85.101302](https://doi.org/10.1103/PhysRevD.85.101302). arXiv: [1201.4858](https://arxiv.org/abs/1201.4858) [hep-ph].
- [24] Xiangyi Cui et al. "Dark Matter Results from 54-Ton-Day Exposure of PandaX-II Experiment". In: *Physical Review Letters* 119.18 (2017). DOI: [10.1103/physrevlett.119.181302](https://doi.org/10.1103/physrevlett.119.181302). URL: <https://doi.org/10.1103/physrevlett.119.181302>.
- [25] F. Duncan. *User's handbook*. Report. SNOLAB, 2008.
- [26] D. Durnford and M.-C. Piro. "Nucleation efficiency of nuclear recoils in bubble chambers". In: *Journal of Instrumentation* 17.01 (2022), p. C01030. DOI: [10.1088/1748-0221/17/01/c01030](https://doi.org/10.1088/1748-0221/17/01/c01030). URL: <https://doi.org/10.1088/1748-0221/17/01/c01030>.
- [27] John Ellis, R.A. Flores, and J.D. Lewin. "Rates for inelastic nuclear excitation by dark matter particles". In: *Physics Letters B* 212.3 (1988), pp. 375–380. ISSN: 0370-2693. DOI: [https://doi.org/10.1016/0370-2693\(88\)91332-9](https://doi.org/10.1016/0370-2693(88)91332-9). URL: <https://www.sciencedirect.com/science/article/pii/0370269388913329>.
- [28] J. Engel, S. Pittel, and P. Vogel. "NUCLEAR PHYSICS OF DARK MATTER DETECTION". In: *International Journal of Modern Physics E* 01.01 (1992), pp. 1–37. DOI: [10.1142/S0218301392000023](https://doi.org/10.1142/S0218301392000023). eprint: <https://doi.org/10.1142/S0218301392000023>. URL: <https://doi.org/10.1142/S0218301392000023>.
- [29] J. Engel and P. Vogel. "Neutralino inelastic scattering with subsequent detection of nuclear  $\gamma$  rays". In: *Phys. Rev. D* 61 (6 2000), p. 063503. DOI: [10.1103/PhysRevD.61.063503](https://doi.org/10.1103/PhysRevD.61.063503). URL: <https://link.aps.org/doi/10.1103/PhysRevD.61.063503>.
- [30] J. Engel and P. Vogel. "Neutralino inelastic scattering with subsequent detection of nuclear gamma-rays". In: *Phys. Rev. D* 61 (2000), p. 063503. DOI: [10.1103/PhysRevD.61.063503](https://doi.org/10.1103/PhysRevD.61.063503). arXiv: [hep-ph/9910409](https://arxiv.org/abs/hep-ph/9910409).
- [31] J. Engel and P. Vogel. "Neutralino inelastic scattering with subsequent detection of nuclearmml:math xmlns:mml="http://www.w3.org/1998/Math/MathML" display="inline"mml:mi/mml:mi/mml:mathrays". In: *Physical Review D* 61.6 (2000). DOI: [10.1103/PhysRevD.61.063503](https://doi.org/10.1103/PhysRevD.61.063503). URL: <https://doi.org/10.1103/PhysRevD.61.063503>.
- [32] "Exposures to  $^{222}\text{Rn}$  and its progeny derived from implanted  $^{210}\text{Po}$  activity". In: *Radiation Measurements* 41.1 (2006), pp. 101–107. ISSN: 1350-4487. DOI: <https://doi.org/10.1016/j.radmeas.2005.03.004>.
- [33] SNOLAB Gamma Assay Facility. "<http://www.snolab.ca/users/services/gamma-assay/index.html>". In: ().
- [34] JiJi Fan, Matthew Reece, and Lian-Tao Wang. "Non-relativistic effective theory of dark matter direct detection". In: *J. Cosmol. Astropart. Phys.* 11 (2010), p. 042. DOI: [10.1088/1475-7516/2010/11/042](https://doi.org/10.1088/1475-7516/2010/11/042). arXiv: [1008.1591](https://arxiv.org/abs/1008.1591) [hep-ph].

- [35] Douglas P. Finkbeiner, Tongyan Lin, and Neal Weiner. “Inelastic dark matter and DAMA/LIBRA: An experimentum crucis”. In: *Phys. Rev. D* 80 (11 2009), p. 115008. DOI: [10.1103/PhysRevD.80.115008](https://doi.org/10.1103/PhysRevD.80.115008). URL: <https://link.aps.org/doi/10.1103/PhysRevD.80.115008>.
- [36] A. Liam Fitzpatrick, Wick Haxton, Emanuel Katz, Nicholas Lubbers, and Yiming Xu. “The Effective Field Theory of Dark Matter Direct Detection”. In: *JCAP* 02 (2013), p. 004. DOI: [10.1088/1475-7516/2013/02/004](https://doi.org/10.1088/1475-7516/2013/02/004). arXiv: [1203.3542](https://arxiv.org/abs/1203.3542) [hep-ph].
- [37] Daniel Foreman-Mackey, David W. Hogg, Dustin Lang, and Jonathan Goodman. “emcee: The MCMC Hammer”. In: *Publications of the Astronomical Society of the Pacific* 125.925 (2013), pp. 306–312. DOI: [10.1086/670067](https://doi.org/10.1086/670067). URL: <https://doi.org/10.1086/670067>.
- [38] Drew Anthony Fustin. “First Dark Matter Limits from the COUPP 4 kg Bubble Chamber at a Deep Underground Site”. PhD thesis. Chicago U., 2012.
- [39] Vera Gluscevic and Samuel D. McDermott. “dmdd: Dark Matter Direct Detection”. In: *Astrophysics Source Code Library* (June 2015), ascl:1506.002. URL: <https://ui.adsabs.harvard.edu/abs/2015ascl.soft06002G>.
- [40] Mark W. Goodman and Edward Witten. “Detectability of Certain Dark Matter Candidates”. In: *Phys. Rev. D* 31 (1985). Ed. by M. A. Srednicki, p. 3059. DOI: [10.1103/PhysRevD.31.3059](https://doi.org/10.1103/PhysRevD.31.3059).
- [41] Lawrence J. Hall, Takeo Moroi, and Hitoshi Murayama. “Sneutrino cold dark matter with lepton number violation”. In: *Phys. Lett. B* 424 (1998), pp. 305–312. DOI: [10.1016/S0370-2693\(98\)00196-8](https://doi.org/10.1016/S0370-2693(98)00196-8). arXiv: [hep-ph/9712515](https://arxiv.org/abs/hep-ph/9712515).
- [42] Chiu Man Ho and Robert J. Scherrer. “Anapole Dark Matter”. In: *Phys. Lett. B* 722 (2013), pp. 341–346. DOI: [10.1016/j.physletb.2013.04.039](https://doi.org/10.1016/j.physletb.2013.04.039). arXiv: [1211.0503](https://arxiv.org/abs/1211.0503) [hep-ph].
- [43] Miaotianzi Jin. “Measurements and Analysis of the Sensitivity of Superheated C3F8 Bubble Chambers to Interactions from WIMP Dark Matter”. PhD thesis. Northwestern University, 2019.
- [44] Sunghyun Kang, S. Scopel, Gaurav Tomar, and Jong-Hyun Yoon. “Protonphilic spin-dependent inelastic dark matter as a viable explanation of DAMA/LIBRA-phase2”. In: *Phys. Rev. D* 99 (2 2019), p. 023017. DOI: [10.1103/PhysRevD.99.023017](https://doi.org/10.1103/PhysRevD.99.023017). URL: <https://link.aps.org/doi/10.1103/PhysRevD.99.023017>.
- [45] Bradley Kavanagh. “New directional signatures from the non-relativistic effective field theory of dark matter”. In: *Physical Review D* 92 (May 2015). DOI: [10.1103/PhysRevD.92.023513](https://doi.org/10.1103/PhysRevD.92.023513).
- [46] Bradley J. Kavanagh and Thomas D. P. Edwards. WIMpy\_NREFT v1.1 [Computer Software], doi:10.5281/zenodo.1230503. Available at [https://github.com/bradkav/WIMpy\\_NREFT](https://github.com/bradkav/WIMpy_NREFT). 2018.
- [47] H. Kluck et al. “Latest results of CRESST-III’s search for sub-GeV/csup2/sup dark matter”. In: *Journal of Physics: Conference Series* 1468.1 (2020), p. 012038. DOI: [10.1088/1742-6596/1468/1/012038](https://doi.org/10.1088/1742-6596/1468/1/012038). URL: <https://doi.org/10.1088/1742-6596/1468/1/012038>.
- [48] Chris Kouvaris. “Composite Millicharged Dark Matter”. In: *Phys. Rev. D* 88.1 (2013), p. 015001. DOI: [10.1103/PhysRevD.88.015001](https://doi.org/10.1103/PhysRevD.88.015001). arXiv: [1304.7476](https://arxiv.org/abs/1304.7476) [hep-ph].

- [49] J.D. Lewin and P.F. Smith. "Review of mathematics, numerical factors, and corrections for dark matter experiments based on elastic nuclear recoil". In: *Astroparticle Physics* 6.1 (1996), pp. 87–112. ISSN: 0927-6505. DOI: [https://doi.org/10.1016/S0927-6505\(96\)00047-3](https://doi.org/10.1016/S0927-6505(96)00047-3). URL: <https://www.sciencedirect.com/science/article/pii/S0927650596000473>.
- [50] "Measurement of radon diffusion and solubility constants in membranes". In: *Nuclear Instruments and Methods in Physics Research Section B: Beam Interactions with Materials and Atoms* 61.1 (1991), pp. 8–11. ISSN: 0168-583X. DOI: [https://doi.org/10.1016/0168-583X\(91\)95553-P](https://doi.org/10.1016/0168-583X(91)95553-P).
- [51] Dongming Mei and A. Hime. "Muon-induced background study for underground laboratories". In: *Phys. Rev. D* 73 (2006), p. 053004. DOI: [10.1103/PhysRevD.73.053004](https://doi.org/10.1103/PhysRevD.73.053004). arXiv: [astro-ph/0512125](https://arxiv.org/abs/astro-ph/0512125).
- [52] Yue Meng et al. "Dark Matter Search Results from the PandaX-4T Commissioning Run". In: *Phys. Rev. Lett.* 127.26 (2021), p. 261802. DOI: [10.1103/PhysRevLett.127.261802](https://doi.org/10.1103/PhysRevLett.127.261802). arXiv: [2107.13438](https://arxiv.org/abs/2107.13438) [hep-ex].
- [53] Yue Meng et al. "Dark Matter Search Results from the PandaX-4T Commissioning Run". In: *Phys. Rev. Lett.* 127 (26 2021), p. 261802. DOI: [10.1103/PhysRevLett.127.261802](https://doi.org/10.1103/PhysRevLett.127.261802). URL: <https://link.aps.org/doi/10.1103/PhysRevLett.127.261802>.
- [54] G. Monari, B. Famaey, I. Carrillo, T. Piffl, M. Steinmetz, R. F. G. Wyse, F. Anders, C. Chiappini, and K. Janßen. "The escape speed curve of the Galaxy obtained from iGaia/i DR2 implies a heavy Milky Way". In: *Astronomy & Astrophysics* 616 (2018), p. L9. DOI: [10.1051/0004-6361/201833748](https://doi.org/10.1051/0004-6361/201833748). URL: <https://doi.org/10.1051/0004-6361/201833748>.
- [55] Torsten Åkesson et al. "Light Dark Matter eXperiment (LDMX)". In: (Aug. 2018). arXiv: [1808.05219](https://arxiv.org/abs/1808.05219) [hep-ex].
- [56] Alan Edward Robinson. "Dark Matter Limits From a 2L C3F8 Filled Bubble Chamber". In: (2015). DOI: [10.2172/1248221](https://doi.org/10.2172/1248221).
- [57] Kai Schmidt-Hoberg and Martin Wolfgang Winkler. "Improved constraints on inelastic dark matter". In: *Journal of Cosmology and Astroparticle Physics* 2009.09 (2009), pp. 010–010. DOI: [10.1088/1475-7516/2009/09/010](https://doi.org/10.1088/1475-7516/2009/09/010). URL: <https://doi.org/10.1088/1475-7516/2009/09/010>.
- [58] Kai Schmidt-Hoberg and Martin Wolfgang Winkler. "Improved constraints on inelastic dark matter". In: *Journal of Cosmology and Astroparticle Physics* 2009.09 (2009), p. 010. DOI: [10.1088/1475-7516/2009/09/010](https://doi.org/10.1088/1475-7516/2009/09/010). URL: <https://dx.doi.org/10.1088/1475-7516/2009/09/010>.
- [59] Frederick Seitz. "On the Theory of the Bubble Chamber". In: *Physics of Fluids* 1.1 (Jan. 1958), pp. 2–13. DOI: [10.1063/1.1724333](https://doi.org/10.1063/1.1724333).
- [60] Kris Sigurdson, Michael Doran, Andriy Kurylov, Robert R. Caldwell, and Marc Kamionkowski. "Dark-matter electric and magnetic dipole moments". In: *Phys. Rev. D* 70 (2004). [Erratum: *Phys.Rev.D* 73, 089903 (2006)], p. 083501. DOI: [10.1103/PhysRevD.70.083501](https://doi.org/10.1103/PhysRevD.70.083501). arXiv: [astro-ph/0406355](https://arxiv.org/abs/astro-ph/0406355).
- [61] David Smith and Neal Weiner. "Inelastic dark matter". In: *Phys. Rev. D* 64 (4 2001), p. 043502. DOI: [10.1103/PhysRevD.64.043502](https://doi.org/10.1103/PhysRevD.64.043502). URL: <https://link.aps.org/doi/10.1103/PhysRevD.64.043502>.
- [62] N. J. T. Smith. "The SNOLAB deep underground facility". In: *Eur. Phys. J. Plus* 127 (2012), p. 108. DOI: [10.1140/epjp/i2012-12108-9](https://doi.org/10.1140/epjp/i2012-12108-9).

- [63] W B Wilson, R T Perry, E F Shores, W S Charlton, Theodore A Parish, G P Estes, T H Brown, Edward D. Arthur, Michael Bozoian, T R England, D G Madland, and J E Stewart. "SOURCES 4C : a code for calculating ([alpha],n), spontaneous fission, and delayed neutron sources and spectra." In: *Applied Radiation and Isotopes* 41.41092883 (Jan. 2002).